



---

Università degli Studi Roma Tre  
Dipartimento di Matematica e Fisica "*E. Amaldi*"

**DARK MATTER DIRECT DETECTION WITH THE  
DARKSIDE PROJECT  
RED: AN EXPERIMENT TO PROBE THE RECOIL  
DIRECTIONALITY IN LIQUID ARGON**

**Simone Sanfilippo**  
Ph.D. Degree in Physics  
XXXII Cycle

Ph.D. Program Coordinator: Prof. G. Degrassi

Supervisors: Prof. S. M. Mari  
Dott. L. Pandola

*Alla mia famiglia.  
A Laura.*

*“But light is no real property of mass. The existence of numberless visible stars can prove nothing against the evidence of numberless invisible ones.”*

*Friederich Bessel*

*“If this would be confirmed, we would get the surprising result that dark matter is present in much greater amount than luminous matter.”*

*Fritz Zwicky*

# Contents

<b>Introduction</b>	<b>1</b>
<b>1 The Dark Matter</b>	<b>4</b>
1.1 Evidences of Dark Matter . . . . .	4
1.1.1 Rotation curves of galaxies . . . . .	5
1.1.2 Galaxy clusters and gravitational lensing . . . . .	6
1.1.3 The Cosmic Microwave Background anisotropies . . . . .	8
1.2 Dark Matter Candidates . . . . .	8
1.2.1 Neutrinos . . . . .	11
1.2.2 Axions . . . . .	11
1.2.3 Baryonic Dark Matter . . . . .	12
1.2.4 WIMPs . . . . .	13
1.3 WIMPs detection . . . . .	15
1.3.1 Differential rate and cross section . . . . .	17
1.3.2 Direct detection techniques . . . . .	18
1.3.3 State of the Art of the direct detection experiments . . . . .	19
<b>2 The DarkSide program</b>	<b>22</b>
2.1 Liquid Argon properties . . . . .	23
2.2 DarkSide-50 . . . . .	24
2.2.1 DarkSide-50 recent results . . . . .	28
2.3 The future of DarkSide . . . . .	29
<b>3 The Recoil Directionality (ReD) Experiment</b>	<b>33</b>
3.1 Recoil Directionality: the motivation . . . . .	33
3.2 A hint to the directionality: the SCENE Experiment . . . . .	38
3.3 The ReD Experiment . . . . .	41
3.3.1 ReD: neutrons production and geometry . . . . .	42
3.3.2 ReD: inside the scattering chamber . . . . .	45
3.3.3 ReD: TPC and cryogenics . . . . .	47
3.3.4 The ReD optical readout . . . . .	51

---

3.3.5	ReD: the neutrons spectrometer . . . . .	54
3.3.6	Data Acquisition and software . . . . .	56
3.4	Monte Carlo expectations . . . . .	58
<b>4</b>	<b>Characterization and Optimization of the TPC</b>	<b>63</b>
4.1	Single Electron Response of SiPM . . . . .	65
4.2	S1 studies and quenching factor . . . . .	72
4.2.1	S1 Light Yield determination . . . . .	75
4.2.2	Pulse shape discrimination . . . . .	80
4.2.3	S1 quenching . . . . .	82
4.3	S2 and charge yield determination . . . . .	85
4.3.1	Electrons drift time and lifetime . . . . .	85
4.3.2	The S1-S2 anti-correlation . . . . .	89
4.3.3	S2 echoes: a tool to estimate $g_2$ . . . . .	94
<b>5</b>	<b>Liquid Scintillator Characterization</b>	<b>99</b>
5.1	Organic liquid scintillators . . . . .	99
5.1.1	Pulse Shape Discrimination . . . . .	100
5.2	Experimental setup . . . . .	102
5.2.1	Theoretical spectrum and expected rates . . . . .	105
5.3	Experimental results . . . . .	107
5.3.1	Energy calibrations . . . . .	107
5.3.2	Time-of-flight analysis and time shift correction . . . . .	110
5.3.3	Neutron efficiency . . . . .	115
<b>6</b>	<b>ReD at Laboratori Nazionali del Sud</b>	<b>118</b>
6.1	Testing the neutron beam . . . . .	120
6.1.1	Experimental setup . . . . .	120
6.1.2	Preliminary results . . . . .	122
	<b>Conclusions</b>	<b>131</b>
	<b>A Matched filter to the Single Electron Response</b>	<b>134</b>
	<b>B Quenching factor in liquid scintillators</b>	<b>139</b>
	<b>C Pulse shape discrimination analysis in liquid scintillators</b>	<b>143</b>
	<b>D Neutron detectors efficiencies</b>	<b>148</b>
	<b>References</b>	<b>150</b>

# List of Figures

1.1	Rotation curve of galaxy NGC 3198 . . . . .	5
1.2	Galaxy cluster Abell 2218 . . . . .	6
1.3	Bullet Cluster . . . . .	7
1.4	Cosmic Microwave Background . . . . .	9
1.5	CMB angular power spectrum . . . . .	10
1.6	WIMPs number density . . . . .	15
1.7	Dark Matter detection methods . . . . .	16
1.8	Current upper limits on spin-independent WIMP-nucleus cross section . . . . .	21
2.1	Pulse Shape Discrimination in liquid argon . . . . .	25
2.2	Conceptual design of the DarkSide-50 experiment . . . . .	26
2.3	The DarkSide-50 LAr TPC . . . . .	27
2.4	The DarkSide-50 $f_{90}$ vs S1 . . . . .	29
2.5	The DarkSide-50 recent results . . . . .	30
2.6	The DarkSide-50 recent low mass WIMP results . . . . .	30
2.7	The DarkSide-20k conceptual design . . . . .	32
2.8	The DarkSide-20k projection curve . . . . .	32
3.1	Differential WIMP-nucleus recoil rate plotted on a Mollweide plot . . . . .	35
3.2	The variation of the total velocity $\mathbf{V}$ during a sidereal day in a frame at rest with Earth . . . . .	36
3.3	Horizontal and vertical daily variation of the events rate for a 100 tonnes detector located at LNGS . . . . .	37
3.4	The SCENE apparatus scheme . . . . .	39
3.5	Scintillation and ionization yields from the SCENE experiment . . . . .	40
3.6	Drawing of the ReD geometrical scheme . . . . .	42
3.7	Kinematical loci of the $p(^7\text{Li}, ^7\text{Be})n$ two body reaction at 28 MeV $^7\text{Li}$ beam energy . . . . .	43

3.8	Angular correlation of neutrons and ${}^7\text{Be}$ from the $p({}^7\text{Li},{}^7\text{Be})n$ two body reaction at 28 MeV ${}^7\text{Li}$ beam energy . . . . .	44
3.9	Inside the scattering chamber of ReD . . . . .	46
3.10	Scatter plot of the $\Delta E$ -E matrix . . . . .	47
3.11	The ReD Liquid Argon Time Projection Chamber . . . . .	48
3.12	Picture of the diving-bell of the ReD TPC . . . . .	49
3.13	Drawing of the ReD cryogenic system . . . . .	50
3.14	Schematic representation of noise generation in SiPM . . . . .	52
3.15	Pictures of one of the SiPM tiles used in ReD and its FEB . . . . .	53
3.16	Photo of the neutron spectrometer used in ReD . . . . .	55
3.17	Photo DAQ system used in Catania. . . . .	57
3.18	Raw waveforms of ReD during normal data taking . . . . .	58
3.19	Rendering of the Geant4-based custom made application for ReD simulation . . . . .	59
3.20	Simulated spectrum of the energy deposition in liquid argon . . . . .	60
3.21	Simulated spectrum of the argon recoil angle . . . . .	61
4.1	Photo of the ${}^{83}\text{Rb}$ trap of the recirculation loop of ReD . . . . .	65
4.2	Measured charge spectrum from a bottom tile channel . . . . .	66
4.3	Measured charge spectrum from a top tile channel . . . . .	66
4.4	SER calibration function from a bottom tile channel . . . . .	67
4.5	SER calibration function from a top tile channel . . . . .	68
4.6	Amplitude of the SER spectrum from a bottom tile channel . . . . .	68
4.7	Amplitude of the SER spectrum from a top tile channel . . . . .	69
4.8	S1 light yield calibration spectrum with ${}^{241}\text{Am}$ source at null fields . . . . .	72
4.9	S1 pulse integral distributions versus TBA before and after the applied corrections . . . . .	74
4.10	Comparison between ${}^{241}\text{Am}$ calibration peaks taken at 200 V/cm drift field, before and after the application of TBA corrections . . . . .	75
4.11	S1 light yield calibration spectrum with ${}^{241}\text{Am}$ source at 200 V/cm drift field . . . . .	76
4.12	Comparison between ${}^{241}\text{Am}$ peaks taken at 0 V/cm and at 200 V/cm electric drift field values . . . . .	77
4.13	S1 light yield calibration spectrum with ${}^{83m}\text{Kr}$ source at 200 V/cm drift field . . . . .	78
4.14	S1 light yield calibration spectrum with ${}^{133}\text{Ba}$ source at 200 V/cm drift field . . . . .	79
4.15	$f_{prompt}$ distribution versus S1 from AmBe neutron source . . . . .	81
4.16	$f_{prompt}$ distribution versus S1 from $d(d,n){}^3\text{He}$ reaction . . . . .	82

4.17	Electric field quenching of the S1 prompt signal . . . . .	83
4.18	Electron drift time distribution from an $^{241}\text{Am}$ run with nominal fields configuration . . . . .	87
4.19	Electron drift time distribution from a $^{83m}\text{Kr}$ run at nominal fields configuration . . . . .	87
4.20	Electron drift lifetime distribution from an $^{241}\text{Am}$ run at nominal fields configuration . . . . .	88
4.21	Electron drift lifetime for comparison . . . . .	89
4.22	S1 yield versus S2 yield from $^{241}\text{Am}$ runs . . . . .	90
4.23	Charge yield ( $Q_y$ ) versus drift field for $^{241}\text{Am}$ runs . . . . .	93
4.24	Recombination probability versus drift field from $^{241}\text{Am}$ double phase data . . . . .	94
4.25	Raw waveform of a typical S2 echo signal . . . . .	95
4.26	Drift time distribution of echo events . . . . .	96
4.27	Charge distribution of S3 events . . . . .	97
5.1	SCIONIX liquid scintillator neutron detectors . . . . .	100
5.2	Technical design of the ReD liquid scintillator neutron detector	103
5.3	Experimental setup used to calibrate the ReD neutron spectrometer . . . . .	104
5.4	Drawing of the setup used for the calibration measurements	104
5.5	Calculated spectrum of $^{252}\text{Cf}$ . . . . .	105
5.6	$^{137}\text{Cs}$ calibration energy spectrum . . . . .	108
5.7	$^{241}\text{Am}$ calibration energy spectrum . . . . .	108
5.8	$^{22}\text{Na}$ calibration energy spectrum . . . . .	109
5.9	Linearity response of one liquid scintillator detector . . . . .	109
5.10	Time-of-flight spectrum with and without PSD rejection . . . . .	110
5.11	Measured spectrum of $^{252}\text{Cf}$ in the near detector . . . . .	111
5.12	Background gamma spectrum . . . . .	112
5.13	Gamma spectrum from $^{252}\text{Cf}$ in the near detector . . . . .	112
5.14	Drawings of a typical gamma interaction from background and $^{252}\text{Cf}$ source in the LScis . . . . .	113
5.15	Time-of-flight spectrum versus PSD. . . . .	114
5.16	Incoming neutron energy in one far detector . . . . .	115
5.17	Measured absolute efficiency profile from the ReD neutron spectrometer . . . . .	116
5.18	Comparison between two measured absolute efficiency profiles from the same liquid scintillator detector . . . . .	117
6.1	Photo of the ReD experiment assembled at the Catania beam line . . . . .	119

6.2	Photo of the experimental apparatus used for the neutron beam test in Catania . . . . .	121
6.3	Reference frames used for the calibration of the movement system . . . . .	122
6.4	Fraction of events in the LScis from the commissioning of the precision movement system . . . . .	123
6.5	Events selection in the silicon detector from the commissioning of the precision movement system . . . . .	124
6.6	Angular correlation between $\theta_n$ and $\theta_{7\text{Be}}$ from the $p(^7\text{Li}, ^7\text{Be})n$ two body reaction at 28 MeV $^7\text{Li}$ beam energy . . . . .	125
6.7	Checking the fraction of events in the LScis in case of $\theta_{7\text{Be}} = 4.6^\circ$ , $\phi_{7\text{Be}} = 48.44^\circ$ . . . . .	126
6.8	Checking the fraction of events in the LScis in case of $\theta_{7\text{Be}} = 5.45^\circ$ , $\phi_{7\text{Be}} = 47.93^\circ$ . . . . .	127
6.9	Triple coincidence events from the July 2019 test beam . . .	128
6.10	Scatter plot used for the triple-coincidence events selection from the July 2019 test beam . . . . .	129
6.11	Simulated S2/S1 ratio versus S1 signal for directional effect prediction . . . . .	132
A.1	Raw waveform from a single channel . . . . .	135
A.2	Single photoelectron average waveform used as kernel in the matched filter . . . . .	135
A.3	Filtered waveform . . . . .	136
A.4	Amplitude spectrum for bottom channel #0 filtered signal .	136
A.5	Amplitude spectrum for top channel #9 filtered signal . . .	137
B.1	Linear fit to the LSci calibration curve with a fixed parameter	141
C.1	Scatter plot of PSD versus energy for the near detector . . .	144
C.2	Scatter plots of PSD versus energy for the far detectors . . .	144
C.3	Figures of Merit (FoMs) in energy slices . . . . .	145
C.4	Distribution of Figure of Merit (FoM) versus energy . . . . .	145
C.5	PSD parameter distribution per slice of 50 keV <sub>ee</sub> energy each	146
C.6	PSD parameter distribution per slice of 25 keV <sub>ee</sub> energy each	147
D.1	Efficiency profiles from single neutron detectors . . . . .	149

# List of Tables

1.1	Current dark matter experiments . . . . .	20
3.1	Positioning angles of the ReD neutron detectors . . . . .	56
4.1	Sources used to calibrate the energy response of the TPC . . . . .	63
4.2	Light Yields from single phase runs calculation . . . . .	80
4.3	Scintillation quenching versus electric field . . . . .	84
4.4	Fit parameters to the Doke-Birks recombination model . . . . .	85
4.5	Dataset used to calibrate the S2 response of the TPC . . . . .	86
4.6	S1 and S2 yields used for the $g_1$ and $g_2$ calculation . . . . .	91
4.7	Charge yield values from double phase ReD data . . . . .	92
5.1	Properties of the Eljen Technology EJ-309 scintillator used in ReD . . . . .	101
5.2	Measured and expected absolute efficiencies at 2.4 MeV and 7 MeV neutron energies of the neutron liquid scintillator cells . . . . .	106
5.3	Calibration sources used to calibrate the neutron spectrometer of ReD . . . . .	107
A.1	Comparison between SNRs and resolutions for filtered and non filtered SER signals . . . . .	138
B.1	Fitting parameters from linear fit constraining to 0 the intercept . . . . .	140
B.2	Fitting parameters from linear fit with free parameters . . . . .	140
B.3	Fitting parameters from Birks saturation law linear fit constraining to 0 the intercept . . . . .	142
D.1	Comparison between measured efficiencies for single neutron detector at 2.5 MeV and 7 MeV . . . . .	148

# Introduction

The existence of dark matter in the Universe is nowadays commonly accepted as the explanation of many astrophysical and cosmological phenomena, ranging from internal motions of galaxies to the large scale inhomogeneities in the cosmic microwave background radiation and the dynamics of colliding galaxy clusters. Cosmological and astronomical observations, supported by the recent results from the Planck satellite indicate that dark matter, which forms the observed large-scale structures and galaxies, accounts for 27%, dark energy, responsible of the observed accelerated expansion of Universe, accounts for 68% while the remaining 5% is composed by ordinary baryonic matter.

Elementary particle physics offers an attractive solution to explain non-baryonic dark matter in the form of relic *Weakly Interacting Massive Particles* (WIMPs), formed in the early Universe and gravitationally clustered together with the standard baryonic matter. In our galaxy, dark matter might constitute a halo, extending far beyond the visible disk, whose properties are inferred from the rotational kinematics of the visible matter. WIMPs could then be directly detected, as the Earth passes through such a halo, by looking at the nuclear recoils produced by WIMP interactions with ordinary matter. Up to now none of the running, neither the already concluded, experiments were able to detect dark matter as a particle.

In this scenario, dual-phase noble liquid Time Projection Chambers (TPC), detecting both ionization and scintillation lights produced by recoiling nuclei, offer the most promising experimental technique to reach the sensitivity required for the possible detection of a weak signal coming from the interaction of dark matter with the ordinary one. Liquid Argon (LAr), in particular, offers an extraordinary and unique add-on key feature: an excellent discrimination power, to disentangle signal from the dominant electron-like background based on the scintillation pulse.

The work presented here is performed in the framework of the DarkSide long term program, which aims at the WIMPs detection down to the neutrino-nucleus limit. DarkSide is a direct search dark matter program, born in 2010

with a small prototype detector used to develop the dark matter revelation technology by means of a Liquid Argon-based Time Projection Chamber (LAr TPC). Since then the detector was upgraded with the current version, DarkSide-50 (DS-50), currently running at INFN - Laboratori Nazionali del Gran Sasso (LNGS), Italy, that uses a dual phase LAr-TPC filled with about 50 kg of liquid argon coming from underground sources. This is necessary because atmospheric argon contains a significant activity from the long-lived cosmogenic  $^{39}\text{Ar}$ .  $^{39}\text{Ar}$  is a beta-emitter which could contribute a significant amount of background and masks a possible dark matter signal in the detector.

The DarkSide Collaboration has demonstrated the powerful discrimination power against background of the LAr technology, even if, because of the limited mass of the active target, DarkSide-50 did not reveal any WIMP signal. The next step will be DarkSide-20k (DS-20k), with a fiducial mass of 30 t of liquid argon, made by very radio-pure materials in order to minimize the internal background, and equipped with new optical readout based on Silicon PhotoMultipliers (SiPMs) instead of the PMTs used by DarkSide-50. Another important feature of DS-20k will be the usage of the so-called depleted liquid argon (underground liquid argon chemically distilled in order to further decrease the internal  $\beta$  contaminants) instead of the one used so far in DS-50.

In the framework of DarkSide program, the R&D project ReD (*Recoil Directionality*) aims to investigate the realization of a liquid argon TPC to directly detect directionality signature, in the energy range of the expected WIMP-nucleus scattering recoils (up to 100 keV), by exploiting the recombination effect. Columnar recombination models suggest, in fact, that the magnitude of such a recombination effect should vary with the angle between the electric field applied to the detector and the track direction. A difference in the electron-ion recombination effect is expected when the ionizing track is either parallel or perpendicular to the electric field. Recombination effect was explored by the SCENE experiment, where a monoenergetic neutron beam was used to irradiate a small dual-phase LAr TPC with and without the application of an electric field. The collaboration achieved, for the first time, the comparison of the light and charge yield of recoils parallel and perpendicular with respect to the electric field (directional sensitivity), in case of a S1 signal due to scintillation. On the contrary, the same was not found for ionization signals. The ReD experiment was proposed with the aim to improve the SCENE measurements as part of the DarkSide program, so it may provide a fully scalable technology to bring the future dark matter experiments based on LAr to the multi-ton scale.

The goal of the project is to irradiate a small LAr TPC with a neutron beam

of known energy and direction by using the 15MV Tandem accelerator of the INFN - Laboratori Nazionali del Sud (LNS) in Catania, Italy. Neutrons are produced by means of the  $p(^7\text{Li}, ^7\text{Be})n$  two-body reaction in inverse kinematics, and then, thanks to the closed kinematics of the reaction, directed towards the TPC. Furthermore, most of the technological solutions adopted in ReD will be part of the future DarkSide-20k detector such as the cryogenic SiPMs that are, for the first time, tested in LAr with the ReD apparatus.

After an introduction on the general aspects of dark matter and its possible particles candidates (**chapter one**), a deeper look on the LAr TPC adopted in the DarkSide program will be presented in **chapter two**, together with the latest recent results from DarkSide-50. The chapter will ends with a look on the future plans of the collaboration.

**Chapter three** will be mostly devoted to the description of the ReD R&D project, starting from the scientific motivations that brought to its proposal and development, up to its construction with a detailed look on its hardware components.

**Chapter four**, in particular, will be focused on the latest recent results on the characterization and the optimization of the ReD LAr TPC, while in **chapter five** the commissioning and calibration of an important piece of the ReD setup, the neutrons spectrometer, will be presented.

This work will ends, finally, with a brief overview, on **chapter six**, of the recent test beam performed in July 2019 at INFN - Laboratori Nazionali del Sud in Catania for the fine tuning and the optimization of the neutrons beam parameters. After a period of tests beams with the full ReD system during the 2018, a new physics run is scheduled early 2020.

# Chapter 1

## The Dark Matter

The existence of dark matter (DM) in the Universe, proposed by Jan Oort [1] and Fritz Zwicky [2, 3] in the 1930s, is today commonly accepted as the explanation of many astrophysical and cosmological phenomena, ranging from internal motions of galaxies [4] to the large scale inhomogeneities in the cosmic microwave background radiation [5] and the dynamics of colliding galaxy clusters [6]. Cosmological and astronomical observations, supported by the recent results from the Planck satellite [7] indicate that, dark matter, which forms the observed large-scale structures and galaxies, accounts for 27%, dark energy, responsible of the observed accelerated expansion of Universe, accounts for 68% while the remaining 5% is composed by ordinary baryonic matter. Despite all of cosmological evidences listed so far, we don't know anything about the real nature of DM even if it is common belief that the dark matter is a kind of matter that is not described by the Standard Model (SM) of particle physics. For this reason, detecting and measuring the properties of DM would represent a big step forward in our knowledge of the Universe.

In this chapter a brief review of some cosmological evidences of the existence of dark matter is presented and some candidates of the dark matter as a particle are described.

### 1.1 Evidences of Dark Matter

Strong evidences of the presence of DM in the Universe are supported by a large number of observations, from the galactic to the cosmological scales. In the following, some of them will be described in detail.

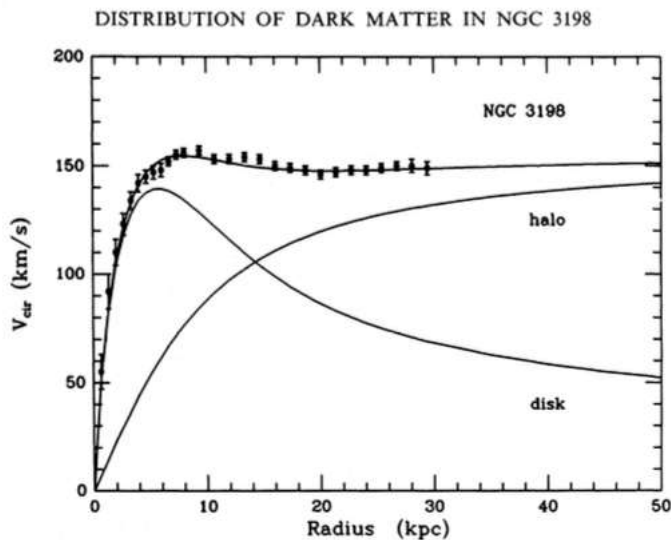


Figure 1.1: Fit to the observed rotation curve of galaxy NGC 3198 (black points with error bars). The other two lines represent the behavior of the halo and the optical disk of galaxy, respectively. The flatness of the velocity beyond the optical disk ( $r \sim 3$  kpc) is clearly visible [8].

### 1.1.1 Rotation curves of galaxies

Observations made in galaxies and galaxy clusters showed that the rotation curves of the galaxies, or the distribution of the circular velocities of stars and gas in a galaxy as a function of their distance from the galactic center, imply that there is not enough visible mass gravitationally bounded with those large systems.

According to the Newton's dynamics, in fact, the radial velocity of a galaxy is given by:

$$v(r) = \sqrt{\frac{GM(r)}{r}} \quad (1.1)$$

where  $M(r) = 4\pi \int \rho(r)r^2 dr$ , and  $\rho(r)$  is the mass density profile of the galaxy. The radial velocity is, so, expected to increase from the center to the edge of the structure, decreasing as  $1/\sqrt{r}$  beyond the optical disk. Unfortunately, the measured rotation curves do not exhibit this described behavior. From the observations what it is got is reported in figure 1.1: far beyond the optical disk the rotation velocity remains constant. These phenomena can be explained if one gets into account the presence of a non-visible halo in the form of DM with  $M(r) \propto r$  and  $\rho(r) \propto 1/r^2$  for distances greater than the visible optical disk. Observational evidences of the presence

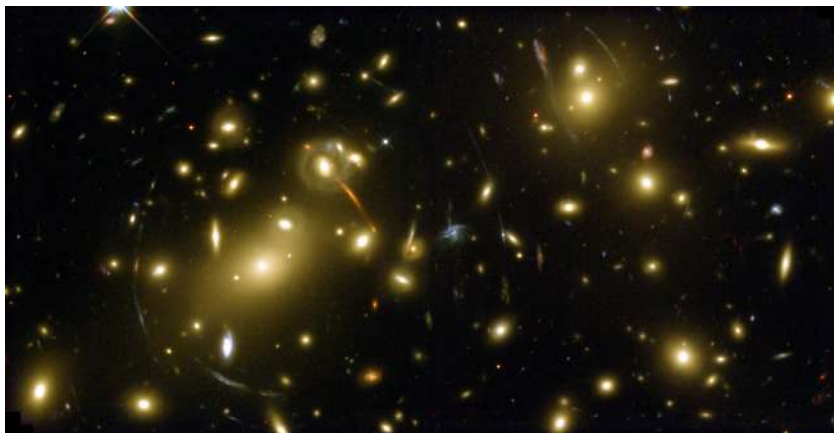


Figure 1.2: Image of the galaxy cluster Abell 2218. Image credits: NASA, Andrew Fruchter and the ERO Team (Sylvia Baggett (STScI), Richard Hook (ST-ECF), Zoltan Levay (STScI)).

of DM in the Universe comes also from the study of galaxy clusters and from galaxies rotating in clusters of galaxies.

### 1.1.2 Galaxy clusters and gravitational lensing

Galaxy clusters are the largest known gravitationally bound objects in the Universe. They consist of hundreds of thousands of galaxies bound together by gravity. As Fritz Zwicky [2, 3] pointed out in the 1930s, the velocity distributions of the galaxies inside a cluster is greater than expected if one gets in to account the content of visible matter of the cluster only. This represents the strongest evidence of the presence of a DM buldge in such an object that attracts the single galaxies and that is the responsible for their higher motion velocity. From the virial theorem in fact, if one considers a system of  $N$  bodies in gravitational equilibrium, starting from the velocity dispersion of the cluster it is possible to derive that the mass  $M$  of the cluster is  $M > M_{vis}$ , with  $M_{vis}$  the mass content of the visible matter. On top of this, clusters offer another important piece of evidence for the existence of DM: the gravitational lensing effect. As predicted by the Einstein's theory of general relativity, massive objects curve the spacetime around them, so the path of light can be significantly deflected in strong gravitational fields. The light emitted by objects behind the cluster can be, then, deflected producing small shape distortions (fig. 1.2), or in some cases, multiple images of the same object. The mass of the galaxy cluster can be then inferred by measuring the deflection angle of the light path. Suppose to

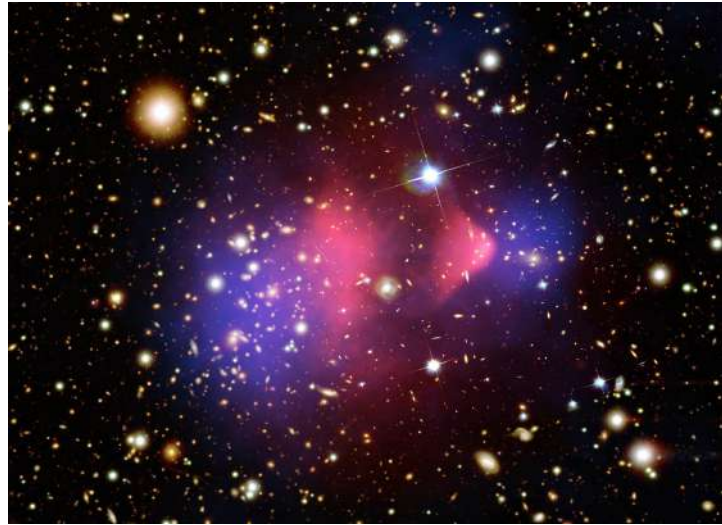


Figure 1.3: Optical image of the Bullet Cluster.

Image credits: <https://arstechnica.com/science/2017/09/science-in-progress-did-the-bullet-cluster-withstand-scrutiny>.

have a cluster of total mass  $M$  and impact parameter  $d$ , the deflection angle is given by:

$$\alpha \approx \left( \frac{GM}{dc^2} \right)^{1/2}. \quad (1.2)$$

The observed lensing effect results much stronger than what expected by assuming only the contribute of stars and gas in the cluster. For galaxy clusters with masses range from  $10^{14}$  to  $10^{15}$  solar masses, stars and gasses make up about 10% of the total, that means that such structures are dominated by some kind of non-baryonic matter which would account for the rest 90% of the total budget of their mass content.

### **Bullet cluster: a peculiar case**

Another evidence of this theory is provided by the observation of gravitational lensing phenomena in the galaxy cluster 1E0657-56, the so-called *Bullet Cluster* (fig. 1.3). This particular system is composed by two smaller clusters that collided in the past. As it is well evident from the picture, during the collision, the stars passed through the collision site without any substantial modification, while the ionized gas clouds interacted electromagnetically, slowing down and assuming the typical shape of a shockwave in the intergalactic medium. So, measurements of the gravitational lensing effect can give an indication of the center of mass of the cluster that one

can suppose can coincide with the gas clouds. Moreover, since the mass of the cluster is dominated by the gas and the stars, X-ray measurements can provide an independent estimation of the baryonic mass distribution of the two sub-clusters. Surprisingly, the measurements above described differ drastically, implying that the center of mass for the clusters is coincident with the galaxies distribution. This represents a clear evidence of the presence of a non-baryonic, weakly interacting form of matter that represents the dominant mass component for galaxies and galaxies clusters.

### 1.1.3 The Cosmic Microwave Background anisotropies

The Cosmic Microwave Background (CMB), predicted in the 1948 by Ralph Alpher and Robert Herman [9] and measured for the first time by Arno Penzias and Robert Wilson from the Bell Laboratories in the 1965 [10], represents the thermal radiation leftover from the decoupling of matter and radiation during the recombination era following the Big Bang. Today it is well known that CMB is isotropic at the level of  $10^{-5}$ , following the spectrum of a black body with temperature  $\sim 2.7$  K. The temperature map of the CMB, as determined by the Planck mission (fig. 1.4), is very uniform and presents small spatial anisotropies. The analysis of this kind of anisotropies can give the chance to perform several tests in both cosmology and particle physics. In particular an analysis of the CMB power spectrum (fig. 1.5), using the so-called Lambda Cold Dark Matter ( $\Lambda$ CDM) model, allows to extract very precisely the content of the Universe in terms of baryons, dark matter and dark energy (4.9%, 26.6% and 68.5%, respectively [7]).

## 1.2 Dark Matter Candidates

Over the time since its formulation, the dark matter problem attracts an increasing number of particle physicists eventually interested in cosmology. By the late 1980s, the hypothesis that the missing baryon problem in the Universe consists of one or more yet-unknown particle species had become as the leading paradigm of dark matter. So, referring to the astrophysical evidences of the presence of DM in the Universe, particle-astrophysicists listed down a series of properties that particles must have in order to be considered as a good DM candidate. They have to be **dark** (small cross sections with baryons, no electromagnetic interaction), **stable** over the cosmological time-scale (half-life comparable with the age of the large scale structures of the Universe), in **thermal equilibrium** with photons and baryons and with no **color charge**. In addition to these, based only on theoretical “prejudice”,

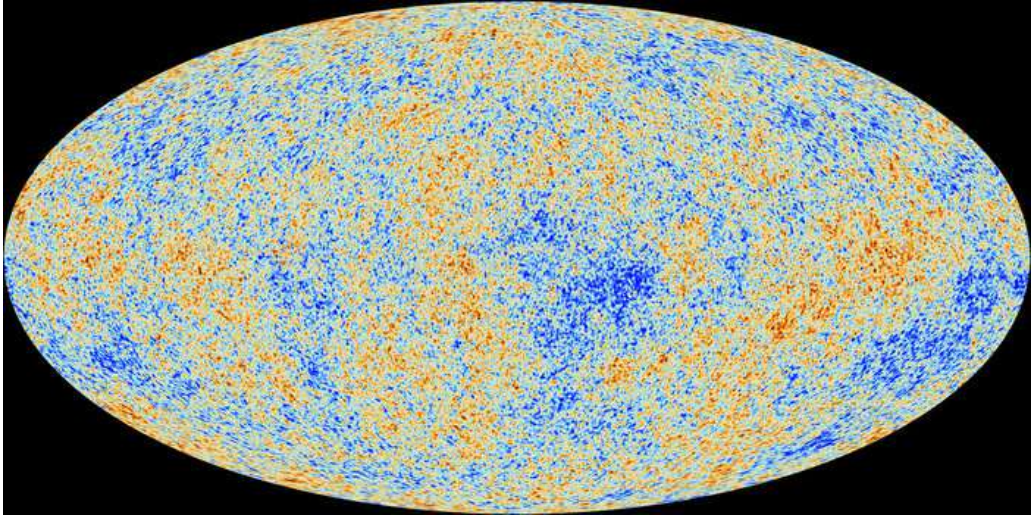


Figure 1.4: The anisotropies of the Cosmic Microwave Background (CMB) as observed by Planck satellite [7]. The CMB is a snapshot of the oldest light in our Universe, imprinted on the sky when the Universe was just 380 000 years old. It shows tiny temperature fluctuations that correspond to regions of slightly different densities, representing the seeds of all future structure: the stars and galaxies of today. Image credits: <https://www.esa.int>

they should also be **theoretically appealing**, means that its existence has to be advocated independently from other theories. Moreover, from a pure astrophysical point of view, dark matter has to be **cold**, in the sense that it has to be non relativistic at the time of decoupling from the radiation and with a small dispersion velocity at the present epoch (on the contrary, relativistic particles at the epoch of decoupling are considered as **hot** particles). Unfortunately, the Standard Model of particles does not provide any suitable candidate that satisfies any or part of this requirements. This could mean that DM should not made of particles at all, as suggested by several theories on the modification of the general relativity [11], or that it is composed of a new form of yet undiscovered particles.

Many theories have been proposed during the last decades to provide a dark matter candidate as a particle, but for the purposes of this thesis, only a sample of this so-called *zoo* will be discussed: neutrinos, axions, baryonic dark matter and WIMPs.

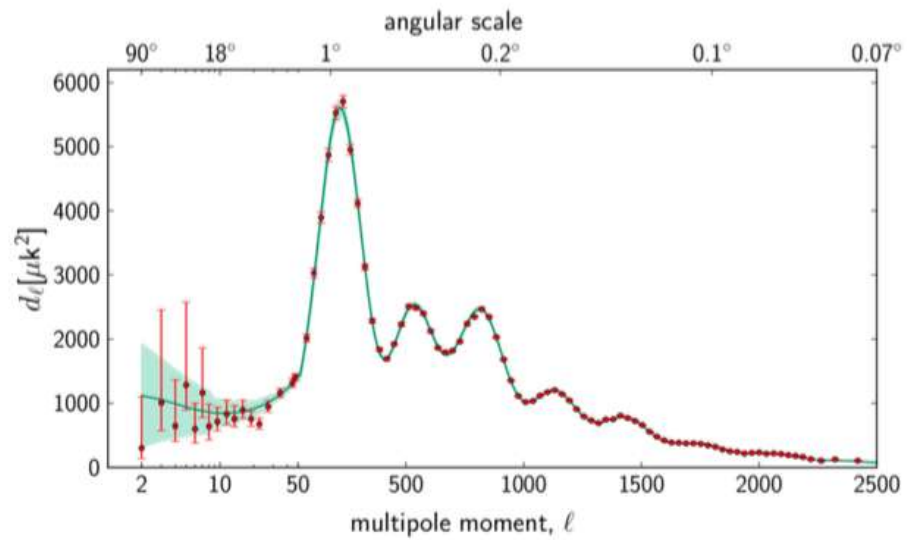


Figure 1.5: The angular power spectrum of the Cosmic Microwave Background as calculated by the Planck Collaboration: red points are the data, while the green line is a best-fit with the  $\Lambda$ CDM model. In order to calculate the baryon density, the ratio between the first and the second peak is needed, while the total number density is due to the ratio among the second and the third ones [7].

### 1.2.1 Neutrinos

In the framework of the Standard Model, neutrinos are the only particles that are stable, electrically neutral and not strongly interacting and so they were considered for a long time the perfect dark matter candidates. In the middle of 80's, in particular, with the development of numerical simulations, neutrinos would expect to have an important role in cosmology, and pushed the astrophysicist to consider the possibility that dark matter halos surrounding galaxies and galaxies clusters may not be made up of astrophysical objects (like for example faint stars (more on par. 1.2.3)), but instead of a gas of non-baryonic particles.

The total relic neutrinos density is however predicted to be

$$\Omega_\nu = \sum_{i=1}^3 \frac{m_i}{93 \text{ eV}} \quad (1.3)$$

where  $m_i$  is the mass of the neutrino species  $i$ . Again, from the analysis of the CMB, the Planck collaboration found [12] that  $\sum m_\nu < 0.23 \text{ eV}$ . This implies an upper limit on the total neutrinos relic density of  $\Omega_\nu h^2 \leq 0.002$ , which means that neutrinos are not abundant enough to be considered as dark matter candidates. Moreover, SM neutrinos, being very light thermal relics, are predicted to be relativistic particles during the early stage of Universe formation, and thus would represent an example of hot dark matter [13, 14]. Simulations have shown that hot dark matter particles would tend to collapse before the formation of galaxies and galaxies clusters, since its relativistic nature would not allow the accumulation of matter. Moreover, from these it emerges that cold and hot dark matter particles lead to very different patterns of large scale structures in the Universe.

Although neutrinos were not good candidates of dark matter particles, this does not preclude the possibility for other neutrino-like particles might be. Sterile neutrinos, for example, have been proposed as DM candidates. These particles are similar to SM neutrinos, but without electroweak interactions [15] and with a small degree of mixing with standard ones. Furthermore, such particles would have never been in thermal equilibrium in the early Universe, but would have been produced through the neutrinos mixing mechanism. Finally, depending on their mass, these would constitute either a hot or a cold candidate for dark matter particles ( $m_{\nu_s} \sim \text{keV}$ ).

### 1.2.2 Axions

Quantum Chromodynamics (QCD) is a successful theory that describes strong interactions between quarks and gluons. QCD, however, suffers from

one issue known as the *strong-CP problem*. Briefly, the QCD Lagrangian contains a term closely related to the phase of the QCD vacuum. If it was of the order of unity, this should introduce a charge-parity (CP) violating effect, causing the electric dipole moment of neutron to be much more larger than what experimentally measured ( $\sim 10^{-10}$ ) [16]. This has been interpreted by many as the indication of some new physics comes into the theory to explain this small value. The solution of this problem, comes first by R. Peccei and H. Quinn [17] in the 1977, by introducing the spontaneous breaking of a new chiral symmetry  $U(1)$ . In the same year, Wilczek [18] and Weinberg [19] independently proposed that such a symmetry broken might be due to the presence of a Nambu-Goldstone boson, called an axion.

Axions with masses in the range of  $m_a \sim 10^{-6} - 10^{-4}$  eV, being stable over cosmological time-scales, if sufficiently plentiful, might constitute a dark matter halo surrounding galaxies and galaxies clusters, have become one of the most popular and well studied dark matter particles candidates.

### 1.2.3 Baryonic Dark Matter

One of the first hypothesis on the missing baryon problem in the Universe was that this missing mass in galaxies and galaxies clusters might make up of faint material. To many astronomers and astrophysicists, in fact, the most obvious solution to the DM problem was thought to a class of compact objects much less luminous, but quite similar, to the normal stars and that could constitute the dark galaxies halos. Possible candidates for this class of objects were found in planets, brown, red and white dwarfs, neutron stars and primordial black holes, simply the compact objects known as Massive Astrophysical Compact Halo Objects (MACHOs).

Nowadays there is a large consensus that MACHOs do not constitute the large fraction of missing matter in the Universe. However several experiments looked for them in the past by using essentially two lines of investigation: gravitational micro-lensing survey <sup>1</sup> and the determination of missing matter based on the measurement of primordial light elements abundances and from CMB.

Finally, constraints on the cosmological baryonic density becomes very important in the last decades. Of primary importance were the first high precision measurements of the primordial deuterium abundance that were used to determined the baryonic abundance with a 10% precision  $\Omega_b h^2 =$

---

<sup>1</sup>In the framework of the Einstein's general relativity, a massive body could deflect the light from a distant source, in such a way to reproduce multiple images of the source or even a ring, called Einstein's ring [20]. This technique could also be used to search for compact objects in the halos of galaxies like the Milky Way or of the local group.

$0.020 \pm 0.002$  (95% CL) [21] leaving no room for baryonic MACHOs. Today this number was improved by studying the angular power spectrum of CMB (see par. 1.1.3) firstly thanks to the observations made by the WMAP satellite, and then by the Planck Collaboration that fixed the most recent value to  $\Omega_b h^2 = 0.02225 \pm 0.00016$  [7]. When this is compared with the total mass density inferred with this and other experiments, became clear that less than 5% of the matter in the Universe is in the form of baryonic particles.

### Primordial Black Holes

Primordial black holes as dark matter candidates were discussed for the first time by Carr and Hawking in the 1974 [22]. According to the authors this kind of objects exhibits a mass that is of the same order of that contained within the event horizon at the time of their formation ( $M_{horizon} \sim 10^{15} \text{ kg} \times (10^7 \text{ GeV/T})^2$ ), allowing for a very large masses range (from  $10^{14} \text{ kg}$  to  $10^{23} \text{ kg}$ ) for dark matter in the form of primordial black holes. Unfortunately, their number in the Universe is too poor to account for the observed amount of dark matter. Recent detection of gravitational waves originating from merging black holes has however renewed interest of astrophysicists on this objects [23].

### 1.2.4 WIMPs

The term WIMP, Weakly Interacting Massive Particle, was coined in the 1984 by Gary Steigman and Michael Turner to include all dark matter particles candidates. Nowadays the definition of this term has evolved to denote only those particles that interact through the weak force. In particular, with the term WIMP, it is usually denoted a particle that:

- interacts with baryonic matter only at the weak scale;
- is massive, with a mass usually in the range GeV - TeV and non relativistic at the time of decoupling;
- is stable over the time scale comparable with the age of the Universe;
- has a relic density of the same order of the density of dark matter (about  $0.3 \text{ GeV}/c^2 \text{ cm}^3$ ).

The last point is known as the so-called *WIMP miracle*.

Before the recombination epoch, in fact, WIMPs were produced and annihilated by the reaction:

$$\chi + \bar{\chi} \rightarrow l^+ + l^- \quad (1.4)$$

where  $\chi$  is the common symbol to denote the most general WIMP particle, while  $l$  stands for *lepton*. The main argument here is that in the early stage of the Universe,  $\chi$  and  $\bar{\chi}$  were in thermal equilibrium until the annihilation rate become smaller than the expansion rate of the Universe. This is the so-called *freeze-out* epoch, i.e. the production and the annihilation of WIMPs stopped, so their number in a co-moving volume remained constant giving the relic density that nowadays is observed. Assuming  $\sigma_A$  as the annihilation cross section,  $\nu$  the WIMPs relative velocity and  $n_{eq}$  the number density at the equilibrium, the time evolution of the WIMPs number due to the expansion of the Universe is:

$$\frac{dn}{dt} = -3Hn - \langle \sigma_A \nu \rangle (n^2 - n_{eq}^2) \quad (1.5)$$

where  $H$  is the Hubble constant (to take into account the expansion of the Universe), while the term  $\langle \sigma_A \nu \rangle$  represents the total annihilation cross section thermally averaged. Combining the above equation with the law of entropy conservation, and using the relation between the Hubble constant and the energy density  $\rho$ , the Friedman equation  $H^2 = \frac{8\pi}{3M_P^2}\rho$ , one gets:

$$\frac{dY}{dx} = \left( \frac{45}{\pi M_P^2} \right)^{-\frac{1}{2}} g_*^{\frac{1}{2}} m_\chi \langle \sigma_A \nu \rangle (Y^2 - Y_{eq}^2) \quad (1.6)$$

where  $Y = n/s$  with  $s$  the entropy density,  $x = m_\chi/T$  with  $T$  the photon temperature and  $g_*^{1/2}$  depends on the degrees of freedom. The previous can be numerically solved with the boundary condition  $Y = Y_{eq}$  at  $x \simeq 1$  in order to obtain the WIMPs abundance at the present time. Finally the WIMPs relic density is the computed as:

$$\Omega_\chi h^2 = \frac{\rho_\chi^0 h^2}{\rho_c^0} = \frac{m_\chi^0 s_0 Y_0 h^2}{\rho_c^0} = 2.755 \times 10^8 \frac{Y_0 m_\chi}{GeV} \quad (1.7)$$

where  $\rho_\chi^0$  and  $s_0$  are critical density at the present epoch and the entropy density, respectively [24]. In fig. 1.6 the evolution of  $Y$  as given by the eq. 1.6 is shown. From this it can be notice that the smaller annihilation cross sections, the greater relic densities. So, another way to derive the present WIMPs relic density is the following:

$$\Omega_\chi h^2 \approx \frac{3 \times 10^{-27} cm^3 s^{-1}}{\langle \sigma_A \nu \rangle}. \quad (1.8)$$

Surprisingly (here is the “miracle”), the value calculated with a cross section of the order of that of the weak scale is of the the same order of magnitude of the measured one [24].

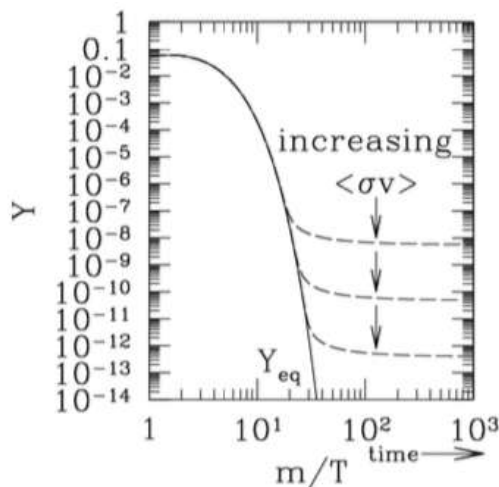


Figure 1.6: WIMPs number density as a function of temperature during the epoch of decoupling. The solid line refers to the  $Y_{eq}$  evolution, while the dashed lines define possible relic density solutions at the *freeze-out* epoch (see the text for the details) [24].

### 1.3 WIMPs detection

It is clear from the above discussion that the existence of dark matter is inferred from its gravitational effects on astrophysical and cosmological objects. So, as particle physicists became interested in the problem of the missing matter in the Universe, some of them began to be interested on how individual particles of dark matter might be detected.

Generally speaking, dark matter particles can be detected by three complementary methods. Referring to the fig. 1.7, those methods are categorized as direct, indirect and at colliders searches. Starting from the last one, the aim of the DM search at colliders, such the *Large Hadron Collider* (LHC) at CERN, is to produce dark matter particles in collisions of SM particles at very high energies. Any dark matter particle produced in such a way would not be detected, so what researchers do in this kind of experiments is to look for a missing energy and momentum in the output channels of the collisions.

*Indirect methods* look for annihilations processes through WIMPs. These would produce SM particles such as neutrinos, gammas, positrons and antiprotons, so an excess of these particles in the cosmic rays flux could be related to the presence of dark matter.

Finally, the *direct detection method*: as it is showed in the fig. 1.7, in this kind of searches it is expected that a dark matter particle, after the inter-

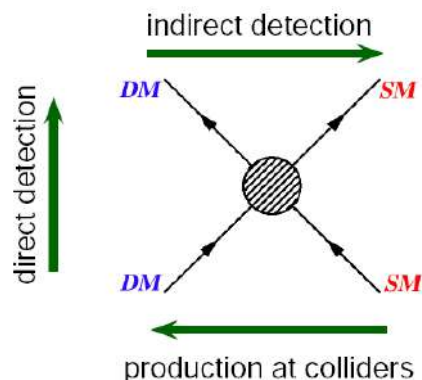


Figure 1.7: Schematic representation of the three possible dark matter interaction ways with the ordinary matter: from left to right, two DM particles can annihilate producing SM particles (indirect detection), from right to left, collisions of two SM particles can produce DM (search at colliders) while, from bottom to top, the case of DM and SM particles elastic scattering it is known as direct search of dark matter. Image credits: <https://www.mpi-hd.mpg.de>.

action with a SM nucleus, will leave some recoil energy in the detector that can be measured. Referring to the *Standard Halo Model* (SHM)<sup>2</sup>, if the dark halo of the Milky Way is composed of dark matter, the expected flux of WIMPs on Earth is

$$\phi_\chi \propto 10^5 \left( \frac{100 \text{ GeV}}{m_\chi} \right) \text{ cm}^{-2} \text{ s}^{-1}. \quad (1.9)$$

Since the expected flux is quite large, it can happen that a small number of WIMPs scatter off a nucleus of baryonic matter of which detectors are made of. Measuring this kind of nuclear recoil is the aim of any direct search dark matter experiment.

In the following, for the aim of this thesis, only this last technique will be considered. The theoretical calculations of the expected event rate will be presented together with a brief description of the detection techniques involved.

<sup>2</sup>The Standard Halo Model (SHM) is a simple model in which the galaxy's dark halo is considered a non-rotating isothermal sphere.

### 1.3.1 Differential rate and cross section

The differential event rate is given by the following

$$\frac{dR}{dE_R} = \frac{\rho_0}{m_N m_\chi} \int_{v_{min}}^{v_{esc}} v f(\mathbf{v}, t) \frac{d\sigma}{dE_R} d^3v \quad (1.10)$$

where:

- $\rho_0$  is the local DM density;
- $m_N$  is the mass of the target nucleus;
- $m_\chi$  is the mass of WIMPs;
- $\frac{d\sigma}{dE_R}$  is the differential cross section for the WIMP-nucleus elastic scattering process;
- $v$  is the WIMPs velocity;
- $f(\mathbf{v}, t)$  is the velocity distribution of WIMPs in the laboratory frame;
- $v_{min}$  is the minimum WIMPs velocity requested to have a recoil energy<sup>3</sup>  $E_R$ , while
- $v_{esc}$  is the WIMP escape velocity from galaxy<sup>4</sup>.

Note that, while  $\rho_0$ ,  $v_{esc}$  and  $f(\mathbf{v}, t)$  come from astrophysical constraints, the other quantities in the eq. 1.10 pertain to particle physics. This is the main reason why the three detection methods listed above are *complementary*.

Integrating the above equation it is possible to calculate the total event rate per kilogram per day over all the possible recoil energies of the elastic WIMP-nucleus process

$$R = \int_{E_{th}}^{\infty} \frac{dR}{dE_R} dE_R \quad (1.11)$$

with  $E_{th}$  the energy threshold of the detector.

The WIMP-nucleus differential cross section in the so-called *spin-independent* formulation can be expressed as:

$$\frac{d\sigma}{dE_R} = \frac{2m_N}{\pi v^2} [Z f_p + (A - Z) f_n]^2 F^2(q) \quad (1.12)$$

<sup>3</sup>This can be expressed as  $v_{min} = \sqrt{m_N E_R / 2\mu^2}$ .

<sup>4</sup>In the case of the Milky Way, the maximum speed that a WIMP gravitationally bound with the galaxy can have, is about 544 km/s [25].

with  $Z$  and  $A$  atomic number and atomic mass of the target nucleus respectively,  $f_p$  and  $f_n$  the effective spin-independent coupling factors of the WIMPs with protons ( $f_p$ ) and neutrons ( $f_n$ ), and  $F^2(q)$  the nuclear form factor of the target. In general the two coupling factors are unitary, so the differential cross section is proportional to  $A^2$ , so the strength of the interaction increases with the atomic mass of the target nuclei.

Considering all the informations from the previous description, one can finally write down the differential rate as:

$$\frac{dR}{dE_R} \propto A^2 F^2(q) e^{-E_R/E_0} \quad (1.13)$$

where  $E_0 = 2\mu^2 v_0^2 / m_N$ , while  $v_0 = 220$  km/s is the average speed of WIMPs in the Earth frame [25]. It is also important to note that the above rate decreases exponentially with the recoil energy  $E_R$  and this is important when considering the threshold energy of a detector.

### 1.3.2 Direct detection techniques

Since the expected event rate for typical dark matter particle is very low (for a WIMP of  $m_\chi = 100$  GeV/ $c^2$  and a WIMP-nucleus scattering cross section of about  $10^{-45}$  cm<sup>2</sup>, the event rate is of the order of  $10^{-5}$  counts/day kg), in order to detect WIMPs, direct dark matter search experiments have to reach a very large exposure mass and a very low background content. Moreover, since the recoil energy expected for the WIMP-nucleus process is of the order of 100 keV, the detectors have to be capable to distinguish between a possible dark matter signal from a background (both radiogenic and cosmogenic) one. From such signals is then possible not only to prove the dark matter signature but also measuring its mass and interaction cross section. So, a low threshold detector is needed to reach this goal. For all of these reasons, the major direct detection experiments are built deep underground with a very careful choice of very radiopure materials, and using passive shields or active vetoes against background events.

Usually, the direct detection experiments are based on three principles: **scintillation detection**, **ionization detection** and **heat detection**. Many experiments, are, however, based on the combination of two of these.

The *scintillation detection* is mainly based on the scintillation mechanism, i.e. a particle interacting with a scintillator material induces photon emissions due to the de-excitation of the excited atoms or molecules. This de-excitation results in a scintillation light that can be detected by means of different kind of photosensors, like for example *photomultipliers tubes* (PMTs)

or, more recently, *silicon photomultipliers* (SiPMs) depending on the hardware setup. The main characteristic of this kind of detection is that the scintillator material has to be transparent to its own light. Typical scintillator used for direct dark matter detection experiments are crystals (the mainly used are NaI(Tl) or CsI) or liquid noble gases scintillators like argon or xenon.

Furthermore, when a particle interacts inside a detector produces free electrons or electron-hole pairs that can be collected and revealed by applying an electric field to the detector to avoid recombination effects. This is the case of the *ionization detection* technique. A particularly used kind of detectors working with this technique are *time projection chambers* (TPCs) filled with liquid noble gasses, in which free electrons are drifted towards an *ad-hoc* gas region where they discharge and so producing emission of light. Finally, the *heat detection* technique is used mainly in cryogenic bolometers which, cooled down to temperatures of the order of mK, have the capability to detect very small variations of their temperature. This results in the production of phonons which can be detected in order to obtain informations about the interaction point inside the detector.

### 1.3.3 State of the Art of the direct detection experiments

Many particle physics theories beyond the Standard Model, provide natural candidates for WIMPs, but there is a huge range in the possible WIMPs masses (from 1 GeV, up to 10 TeV) and interaction cross sections with normal matter ( $10^{-40} \div 10^{-50} \text{ cm}^2$ ). The full exploration of this range requires several hundreds tonnes-year exposures and the capability to detect nuclear recoil energies in the 1-100 keV range. The motivation for direct WIMPs searches remains extremely strong, especially for high masses ( $\geq 200 \text{ GeV}$ ), not yet explored by the LHC, and the region of low-cross section corresponding to Higgs-mediated scattering [26].

During the last decades several technologies have been developed for the direct detection of dark matter. In table 1.1 are summarized the still ongoing, and future approved, ones. These experiments all share the common goal of achieving the low detection threshold energy required to observe the collisions of WIMPs with target nuclei and the low background, to identify these extremely rare events.

Among all dark matter detectors to date, the XENON Collaboration has obtained the most sensitive limit on spin-independent interactions of WIMPs with nuclei, using a xenon target to place a limit on the WIMP-nucleon

Experiment	Target	$\sigma$ @ 100GeV/c <sup>2</sup> (cm <sup>2</sup> )	$\sigma$ @ 1TeV/c <sup>2</sup> (cm <sup>2</sup> )	Reference
DarkSide-50	UAr	$1.1 \times 10^{-44}$	$3.8 \times 10^{-44}$	[27]
LUX	Xe	$2 \times 10^{-45}$	$2 \times 10^{-44}$	[28]
ArDM	Ar	$8 \times 10^{-45}$	$7 \times 10^{-44}$	[29, 30, 31]
DEAP-3600	AAr	$3.9 \times 10^{-45}$	$1.5 \times 10^{-44}$	[32]
XENON1T	Xe	$1 \times 10^{-47}$	$1 \times 10^{-46}$	[33]
DarkSide-20k	UAr	$7.4 \times 10^{-48}$	$6.9 \times 10^{-47}$	[34]
Argo	UAr	$2.7 \times 10^{-48}$	$2.5 \times 10^{-47}$	[34]

Table 1.1: Comparison of sensitivity for current dark matter experiments leading the search for high mass WIMPs and of future approved and proposed experiments.

interaction cross section of  $4.1 \times 10^{-47}$  cm<sup>2</sup> for a WIMP mass of 30 GeV/c<sup>2</sup> [33]. Evidence for a low-mass dark matter signal has been claimed, in the recent past, by the DAMA/LIBRA [35] and CoGeNT [36] collaborations, and may be consistent with observations of the CDMS collaboration using Si detectors [37]. However, these claims are in tension with a number of other strong results, including those by XENON1T [33]. The positive claims are also in strong contradiction with the results from LUX [28], which directly rule out the interpretation of CoGeNT and CDMS/Si results in terms of low-mass WIMPs. The region of cross section around  $10^{-39}$  cm<sup>2</sup> expected for Z-mediated scattering [26] seems to be fully explored now and excluded. In this scenario, noble liquid time projection chambers, detecting both ionization and scintillation produced by recoiling nuclei, offer the most promising experimental technique to reach the necessary sensitivity. The long-term goal is to reach the sensitivity level set by the so-called *neutrino floor*, the dark matter sensitivity level where coherent nuclear scattering by atmospheric neutrinos provides one count of background.

In order to reach the sensitivity needed at the level of the neutrino floor, collaborations are developing several R&Ds projects. One of them, in particular, is exploring the possibility to have a directional sensitivity detector. In the following, the *Recoil Directionality Experiment* (ReD), within the framework of the DarkSide Collaboration, will be presented as the main topic of this dissertation.

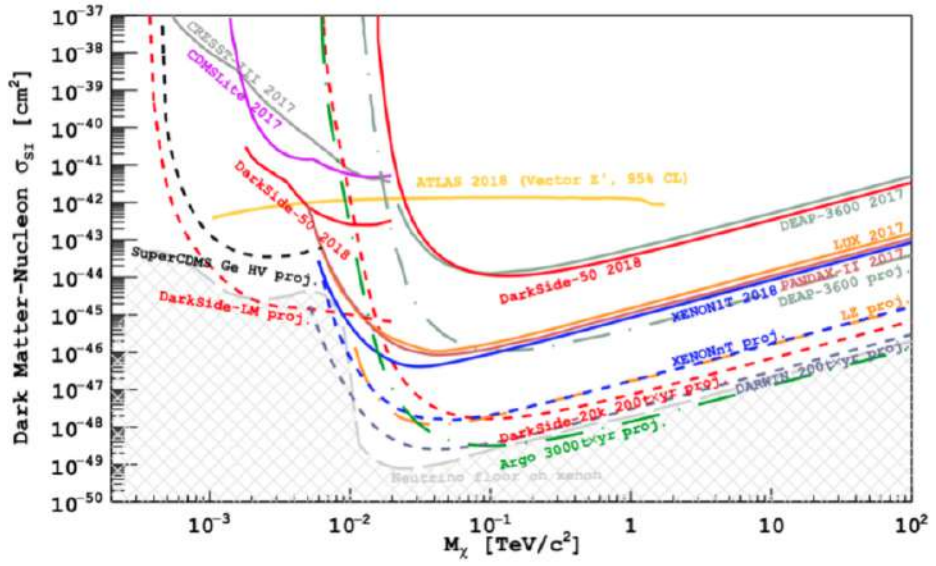


Figure 1.8: Current upper limits on spin-independent WIMP-nucleon cross section for different experiments (see text for details). Projection for future experiments are also shown together with a recent measurement from the ATLAS Collaboration that puts a new constrain on the dark matter searches at colliders [38]. The shadowed grey region represents the so-called *neutrino floor*, the region of the space parameters in which the contribution of the coherent scattering neutrino-nucleus to a possible dark matter signal became irreducible. Image credits: <https://cerncourier.com/defeating-the-background-in-the-search-for-dark-matter/>.

## Chapter 2

# The DarkSide program

DarkSide is a direct search dark matter program, born in 2010 with a small prototype detector called DarkSide-10 used to develop the dark matter revelation technology by means of a Liquid Argon-based Time Projection Chamber (LAr TPC) [39]. Since 2012, the detector was upgraded with the current version, DarkSide-50 (DS-50), actually running at INFN - Laboratori Nazionali del Gran Sasso (LNGS), at a depth of 3800 m.w.e., that uses a dual phase LAr TPC filled with about 50 kg of liquid argon coming from underground sources (Underground Argon (UAr))<sup>1</sup>. In the past, the DarkSide Collaboration has demonstrated the powerful discrimination power against background of the LAr technology, even if, because of the limited mass of the active target, DarkSide did not reveal any WIMP signal. This is the main reason why the collaboration is working on a bigger version of its detector, DarkSide-20k (DS-20k), with a fiducial mass of 30 t of liquid argon, made by very radiopure materials in order to minimize the internal background noise, and equipped with several new optical readout based on Silicon PhotoMultipliers (SiPMs) instead of the PMTs used by DarkSide-50. Another important feature of DS-20k will be the usage of the so-called depleted liquid argon instead of the UAr used so far in DS-50. This, in fact, after the extraction in Colorado, will be shipped to a former coal mine in Sardinia (Italy), where a chemical distillation column will deplete <sup>40</sup>Ar from its radioactive isotope <sup>39</sup>Ar. As its predecessors, even DarkSide-20k will be housed at LNGS and will become operative starting from 2021 (see par. 2.3).

After a brief introduction on liquid argon properties and the main results obtained by the DarkSide-50 experiment, the future plans of the DarkSide program will be explained.

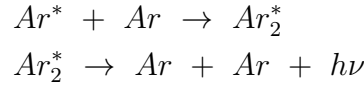
---

<sup>1</sup>The argon is chemically extracted from a CO<sub>2</sub> deposit in a former coal mine in Colorado, USA.

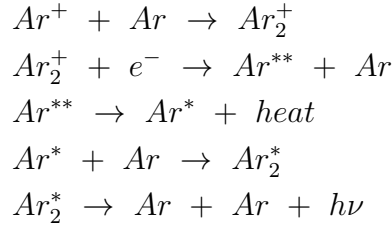
## 2.1 Liquid Argon properties

Liquified noble gases have been largely used in the direct search dark matter experiment in the last decades, mainly because of their excellent scintillation and ionization properties, and because they are available in large quantities such to build very large detectors.

A typical interaction inside such a scintillator material produces excited atoms, and a short track of ionization. Following ionization, electron-ions pairs are produced together with excited diatomic molecules that, after their decay, emit scintillation photons. The scintillation light in argon is the result of two distinct processes, the *excitation luminescence* due to the decay to the ground level of argon excited dimers, and the *recombination luminescence* produced after the recombination of an electron-ion pair. In both cases a vacuum ultra violet (VUV) photon with  $\lambda = 128$  nm is emitted, but the difference between the two contributions comes from the different excimer formation process. In the excitation luminescence process, excited atoms ( $Ar^*$ ), produced by the scattering of a particle, for example an electron, with an argon atom, emit scintillation light through the following reactions chain:



where  $Ar$  stands for argon atom, while  $Ar_2^*$  is the excited argon dimer. On the other hand, recombination luminescence is a more complex process, in which, after the binding between an argon ion ( $Ar^+$ ) and a neutral argon atom in the ground state ( $Ar$ ), an argon molecular ion ( $Ar_2^+$ ) is produced. In this case the process will follow the chain:



where  $Ar^{**}$  is a highly excited argon atom. As it is possible to note from the previous, both the described processes produce as final state the same emission of a 128 nm VUV photon ( $E \sim 9.7$  eV). The atomic de-excitation of an argon molecule is, however, strongly suppressed. In average, in fact,  $Ar^*$  forms excimers before the atomic de-excitation occurs.

The two excimers produced in the above processes are spectroscopically

indistinguishable but have different decay times. They can form, in fact, either a triplet state with a lifetime  $\tau_t \sim 1.5 \mu\text{s}$ , and a single state which has a lifetime  $\tau_s \sim 6 \text{ ns}$  [40]. This time constants do not vary depending on the particles that generates the interaction, but the ratio of the two states (singlet to triplet) depends on the ionization density and it is about 0.3 for electrons, 1.3 for  $\alpha$  particles and 3 for fission fragments, so depending on the species of the ionizing particles [41]. This represents an important feature because allows to distinguish, by a time and a shape analysis of the signals, between particles that induced electron or nuclear recoils via the so-called Pulse Shape Discrimination method (PSD). Electron recoils (ERs), in particular, are  $\beta/\gamma$  events in which the incident particle interacts with the electrons clouds of argon atoms. Those atoms, after the interaction, lose their energy ionizing and exciting the neighboring ones. Nuclear recoils (NRs), on the other hand, are elastic scattering WIMP-nucleus-like events inside the active region of the detector. In this case the de-excitation process of the nucleus ionizes and excites the neighboring argon atoms.

PSD is particularly efficient in liquid argon because singlet and triplet lifetime, as seen before, differ by three order of magnitudes. Furthermore, in double phase detectors like the DarkSide TPCs, for example, a recoil event is detected by measuring both the scintillation and the ionization photons, the last ones by using a drifting electric field in order to minimize the recombination process. As shown in fig. 2.1, in the case of electron recoils (red curve), for example, because of the low density of the electron-ion pairs, there are less recombinations and so less scintillation and more free electrons than the case of a nuclear recoil event. Nuclear recoils, in fact, result in a higher density of electron-ion pairs and this corresponds to a higher scintillation photons (blue curve). Finally, the ratio between ionization to scintillation signals allows to distinguish background events, such as  $\beta$  or  $\gamma$  particles, from a nuclear recoil one. This represents one of the main reasons why the DarkSide collaboration chooses liquid argon instead of other liquified noble liquids.

## 2.2 DarkSide-50

The DarkSide-50 (DS50) experiment is located deep underground inside the hall C of the INFN - Laboratori Nazionali del Gran Sasso (LNGS), under 3800 m.w.e. of rocks. This is an essential feature for the detection of the tiny signal that are expected to come from WIMPs.

DarkSide-50 is essentially composed by three detectors: a dual-phase Liquid Argon Time Projection Chamber (LAr TPC), a Liquid Scintillator Veto

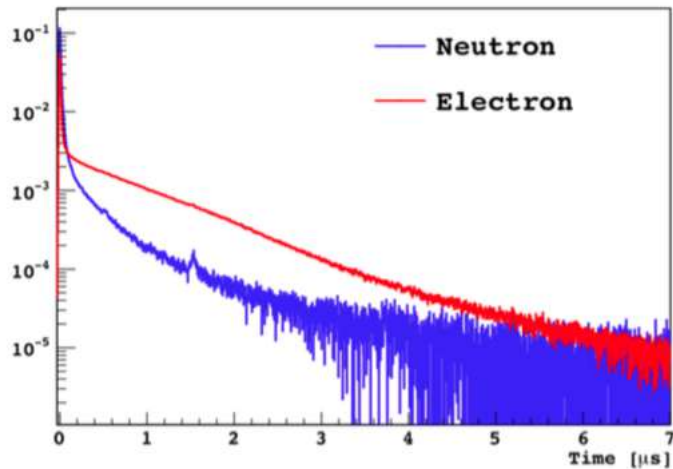


Figure 2.1: Electron (red) and nuclear (blue) recoil events in liquid argon as function of time in  $\mu\text{s}$ . The different shapes and time decays of the two averaged waveforms are the bases for the Pulse Shape Discrimination (PSD) method (see text for more details) [42].

(LSV) and an outer Water Cherenkov Veto (WCV). The DarkSide-50 TPC contains about 50 kg of UAr as active dark matter target, and represents, of course, the core of the experiment. This detector is then immersed in about 30 t of borated liquid scintillator, aimed to veto the TPC from cosmogenic and radiogenic neutrons. Finally, the TPC + LSV system is then deployed inside the WCV, a sphere of 11 m diameter that, with its 1000 t of purified water, is used as a passive shield against cosmic muons. For the sake of completeness, it has to be known that the two veto systems work in the so-called anti-coincidence mode, i.e. events that leave a coincidence signal in both the detectors are rejected. A sketch of the complete DarkSide-50 setup is shown in fig. 2.2.

The DarkSide-50 TPC is shown in the fig. 2.3. It has a cylindrical shape of 35.6 cm diameter and 35.6 cm height, made by a 2.54 cm thick teflon material (PTFE). Its volume contains about 50 kg of UAr and it is closed both on top and on bottom by means of two fused silica windows. The optical readout sensors consisting in two arrays of 19 3-inch Hamamatsu R11065 PMTs, placed on the top and on the bottom of the detector, allowing the detection of events in the active region. All the inner surfaces, as well as the two optical windows, are coated with a wavelength shifter, the *Tetraphenylbutadiene* (TPB), that absorbs the 128 nm VUV photon emitted during the scintillation and ionization processes and re-emits them in the visible range at 420 nm. Both the two silica windows are also coated with a 15 mm thick

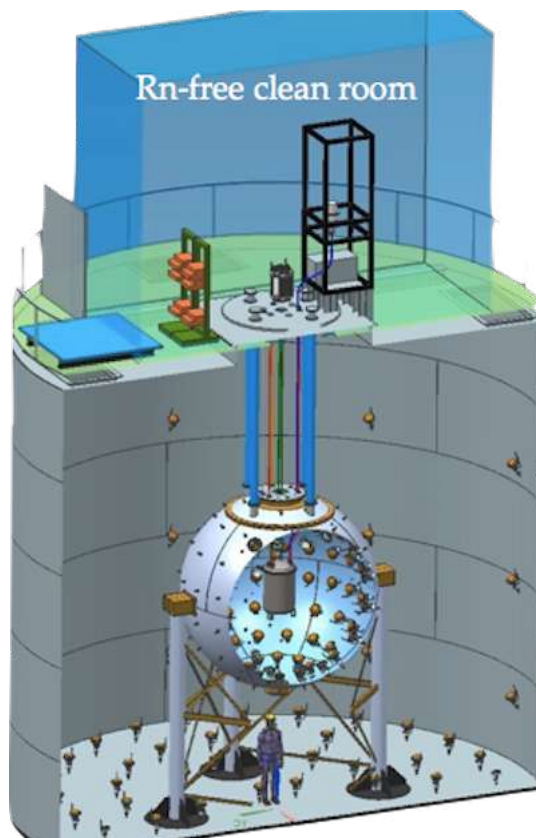


Figure 2.2: Conceptual design of the DarkSide-50 experiment. Are visible the WCV and the LSV surrounding the TPC closed inside a cryostat to maintain the argon in the liquid phase ( $\sim 87$  K).



Figure 2.3: A picture of the DarkSide-50 LAr TPC from the bottom point of view. The array of 19 3-inch bottom PMTs is also visible.

transparent conductive layer of *Indium-Tin-Oxyde* (ITO) that allows the inner surface of the top window to serve as the anode (grounded), while the bottom of the TPC as the High Voltage (HV) cathode.

Furthermore, the top window has a cylindrical ring extending downward the detector to form the so-called *diving bell* with the aim of containing the thick gas layer ( $\sim 2$  cm) necessary to allow for the ionization and electroluminescence signals in the gas phase. The TPC is also surrounded by a copper field cage that allows for the uniformity of the electric field applied to the detector to drift upward the ionization electrons. The two ITO windows, together with the cathode and the anode plane, the field cage and a grid that separates drift and extraction regions, are the so-called *electron-drift system*. Finally, the extraction and electroluminescence fields are independently adjusted by the setting of a potential between the grid and the anode. In standard conditions a drift field of  $200$  V/cm is applied, while extraction and electroluminescence fields are  $2.4$  kV/cm and  $\sim 4.2$  kV/cm, respectively. In a dual phase TPC, i.e. a detector that contains argon in both phases, liquid and gas, in thermal equilibrium like the one of DS50, it is possible to measure both the scintillation light and the ionization signal of the extracted electrons in the gas phase. Briefly, the scintillation signal produced in liquid (S1) frees a certain amount of electrons that, escaping the recombination with the other argon atoms, are drifted toward the upper part of the detec-

tor by means of the applied drift electric field. Once the drifted electrons reach the grid, they are extracted into the gas phase, where, by means of the presence of the electroluminescence field, are accelerated one more time, producing secondary scintillation light (S2). The extraction process depends on the strength of the electric field and, in general, for fields of the order of 2.5 - 3 kV/cm the extraction efficiency reaches its maximum, so in average the whole amount of electrons are completely extracted [43, 44].

The process of secondary scintillation in gas allows a strong multiplication because high amounts of photons are generated per single extracted electron. This mechanism generates the already cited (see par. 2.1) 128 nm VUV photons.

In DarkSide-50, and in general in all the detectors using the same technology, both scintillation and ionization signals are detected at the same time using the equipped photosensors. In DS50, in particular, with the bottom ones, informations about the energy of the prompt scintillation signal are extracted, while the horizontal position in the (x,y) plane can be reconstructed from the S2 distribution across the photosensors of the top array. Finally, it is also possible to reconstruct the interaction vertex associating the z-position of one event with the time delay between the S1 and S2 signals. This time interval can be also used to calculate the electrons drift time in liquid and to infer informations about their drift velocity.

### 2.2.1 DarkSide-50 recent results

Detailed descriptions of the DarkSide detector performances and Monte-Carlo simulations can be found in [45, 46, 47], while fig. 2.4 shows the distribution of scintillation events (S1) versus the PSD parameter<sup>2</sup> after a 532.4 live-days exposure of low-radioactivity underground argon. This was obtained using the so-called *blind analysis* technique, in which the analysis is performed looking at only a quite large sample of events, progressively enlarged once events surviving a series of analysis and quality cuts, allowing to perform a set of criteria to reduce background contaminations and so testing predictions. During this analysis in particular, a set point of 0.1 events of background was considered [27]. Finally, an upper limit on the spin-independent DM-nucleon cross section was set in the framework of the standard isothermal halo model<sup>3</sup>:  $1.14 \times 10^{-44} \text{cm}^2$  ( $3.8 \times 10^{-44} \text{cm}^2$ ,  $3.4 \times 10^{-43} \text{cm}^2$ ) for a 100 GeV/c<sup>2</sup> (1 TeV/c<sup>2</sup>, 10 TeV/c<sup>2</sup>) WIMP particle

<sup>2</sup>The so-called  $f_{90}$  parameter is defined as the fraction of events collected during the first 90 ns of the prompt scintillation pulse.

<sup>3</sup>In the framework of the standard isothermal halo model  $\rho_{DM}=0.3 \text{ GeV}/c^2 \text{cm}^3$ ,  $v_{escape}=544 \text{ km}/\text{sec}$ ,  $v_0=220 \text{ km}/\text{sec}$  and  $v_{Earth}=232 \text{ km}/\text{sec}$ .

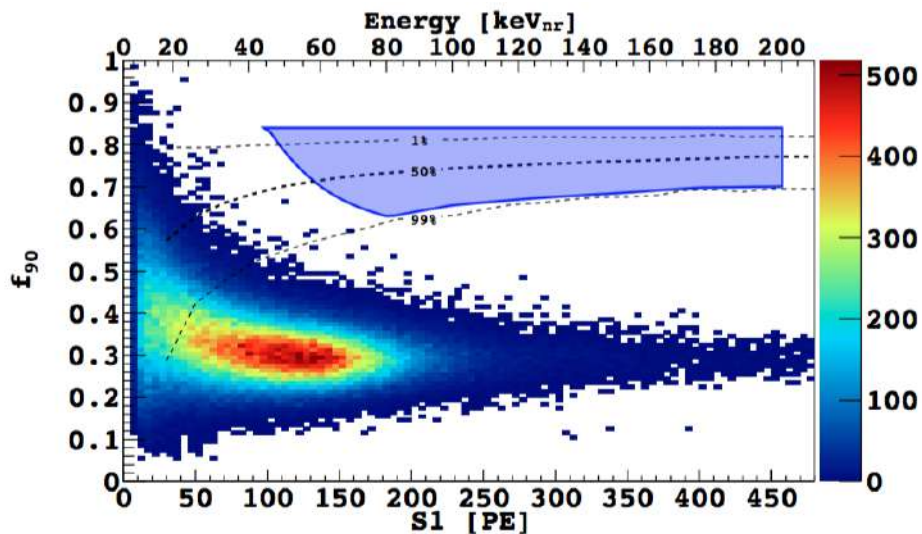


Figure 2.4:  $f_{90}$  vs S1 distribution of events in the energy range (solid blue box) of interest for dark matter detection in the DarkSide-50 experiment [27]. The 1%, 50% and the 99% acceptance contours for  $f_{90}$  are also shown.

(fig. 2.5).

The DarkSide collaboration also presented an important result on the search of the low mass WIMPs (below  $20 \text{ GeV}/c^2$ ) using the DarkSide-50 detector [49]. WIMPs in this mass range produce nuclear recoils well below  $10 \text{ keV}_{nr}$  where the efficiency for detecting the prompt scintillation signal S1 is low and pulse shape discrimination is no longer available. The analysis in this case is mainly based on the gain inherent in the ionization S2 signal of the dual-phase LAr TPC. S1 pulses are usually not large enough to be detectable, so no drift time is available in this case. The position of each event is then assigned as the center of the PMT receiving the largest number of S2 photoelectrons. The S2 photoelectron yield per extracted ionization electron,  $g_2$ , is then determined by studying single electron events obtained during a short period of time in which the inline argon purification system was turned off for maintenance purposes. This analysis settled up a new 90% C.L. exclusion limit above  $1.8 \text{ GeV}/c^2$  for the spin-independent WIMP-nucleon cross section [49] as shown in fig. 2.6.

## 2.3 The future of DarkSide

Although it is not competitive with more recent xenon detectors, the last DarkSide published results, showed in the previous section, allowed the col-

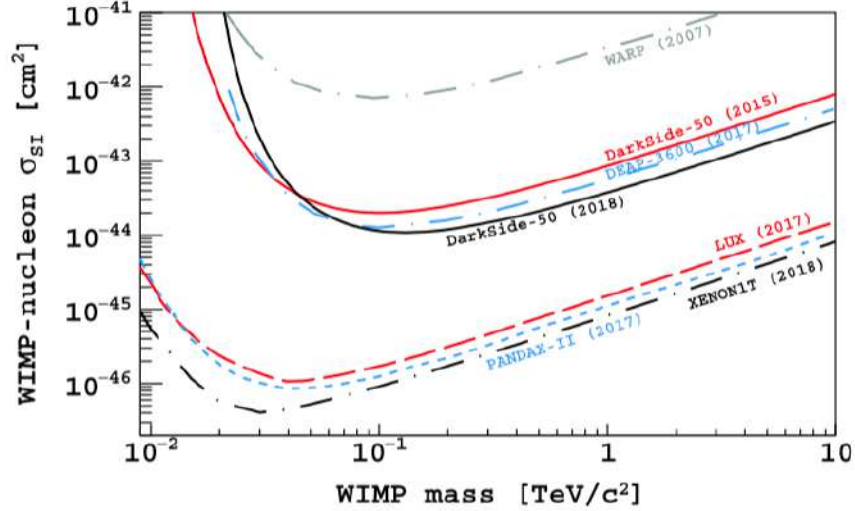


Figure 2.5: Upper limits for the spin independent WIMP-nucleon cross section at 90% C.L. from the analysis on the 532.4 live-days exposure of an underground liquid argon target as reported in [27], compared with results from other dark matter direct search experiments.

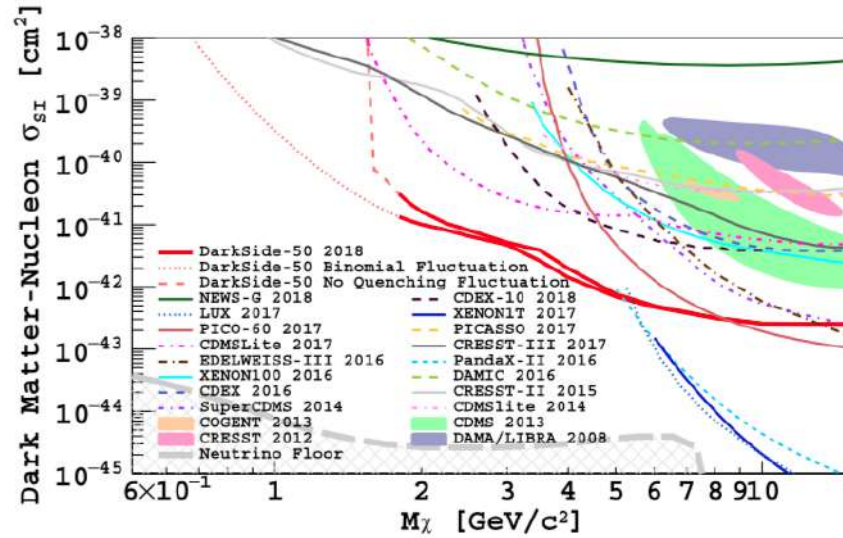


Figure 2.6: Upper limits for the spin independent WIMP-nucleon cross section at 90% C.L. for dark matter particle masses in the range above 1.8 GeV/\$c^2\$ using the DarkSide-50 detector as reported in [49], compared with results from other dark matter direct search experiments.

laboration to plan a great effort toward the upgrade of its detector. In 2015, an enlarged DarkSide Collaboration proposed a long-term program of dark matter searches (the so-called GADMC - Global Argon Dark Matter Collaboration), comprising the DarkSide-20k [34] and Argo experiments, which could cover the entire region of potential discovery at high (above a few hundred  $\text{GeV}/c^2$ ) masses with background-free exposures of 100 tons yr and 1000 tons yr, respectively. The DarkSide-20k experiment, in particular, aims at a significant improvement in the sensitivity for the direct detection of WIMPs in the mass range above a few hundred  $\text{GeV}/c^2$ , reaching  $7.4 \times 10^{-48} \text{ cm}^2$  ( $6.9 \times 10^{-47} \text{ cm}^2$ ) for WIMPs of 1  $\text{TeV}/c^2$  (10  $\text{TeV}/c^2$ ) mass. The collaboration proposed to achieve this goal with a LAr TPC experiment with a fiducial mass of about 30 tons, during a 5 yr run thanks to its low instrumental background [34].

The DarkSide-20k detector will be housed at LNGS as part of the DarkSide long term program of INFN. Its design is mainly based on the experience done with the DarkSide-50 detector: DarkSide-20k will house a dual phase TPC filled with depleted liquid argon (DAr) from underground sources, inside a completely new designed veto system with respect to DarkSide-50. The biggest difference from its predecessors, and from all the other direct search dark matter detectors, will be, however, the usage of about 5210 arrays (about  $15 \text{ m}^2$ ) of newer cryogenic Silicon PhotoMultipliers (SiPM) explicitly designed for this application by Fondazione Bruno Kessler (FBK), Italy, instead of the PMTs used in DarkSide-50. The TPC will have an octagonal shape of 263 cm height per 350 cm width and will be housed inside a cryostat derived from the ProtoDUNE neutrino experiment [50], that will allow to place the optical sensors outside the volume of the detector, thus reducing the radioactive internal background contamination [51]. The TPC will be filled with about 100 tons (about 30 tons in the active volume) of low-radioactive depleted underground argon. In this new detector, in fact, the underground argon will be produced in Colorado, USA, at the Kinder Morgan Doe Canyon Facility, with the extraction plant called *URANIA*, capable to procure 250 kg per day of UAr. This argon, once extracted, will be shipped to Sardinia, Italy, where the *ARIA* plant will proceed with a chemical distillation of the noble liquid, capable of depleting  $^{40}\text{Ar}$  by its radioactive isotope  $^{39}\text{Ar}$ .

As remarked at the beginning of this section, with this conditions, DarkSide-20k will be able to run in a background-free mode for 5 years, with a sensitivity of  $1.2 \times 10^{-47} \text{ cm}^2$  for a dark matter particle of 1  $\text{TeV}/c^2$  (fig. 2.8).

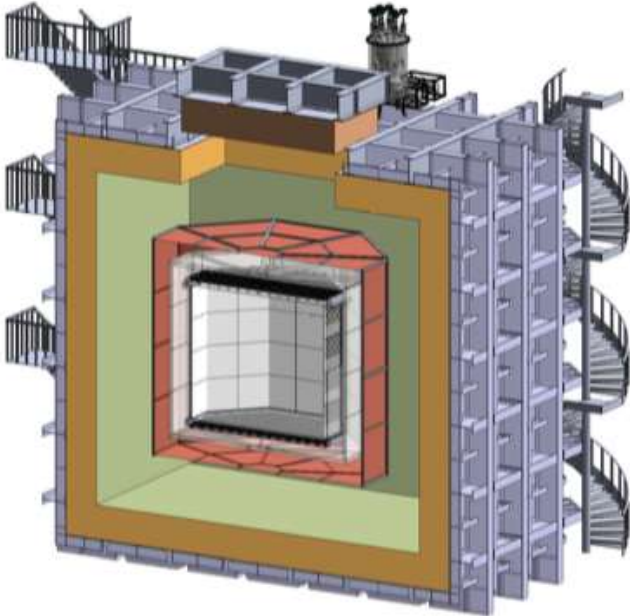


Figure 2.7: The DarkSide-20k conceptual design: the octagonal shape TPC is the innermost part of the detector, that, placed inside a ProtoDUNE-like cryostat [50] filled with atmospheric liquid argon as active neutron shield, is surrounded by a plastic structure that forms part of the neutron veto.

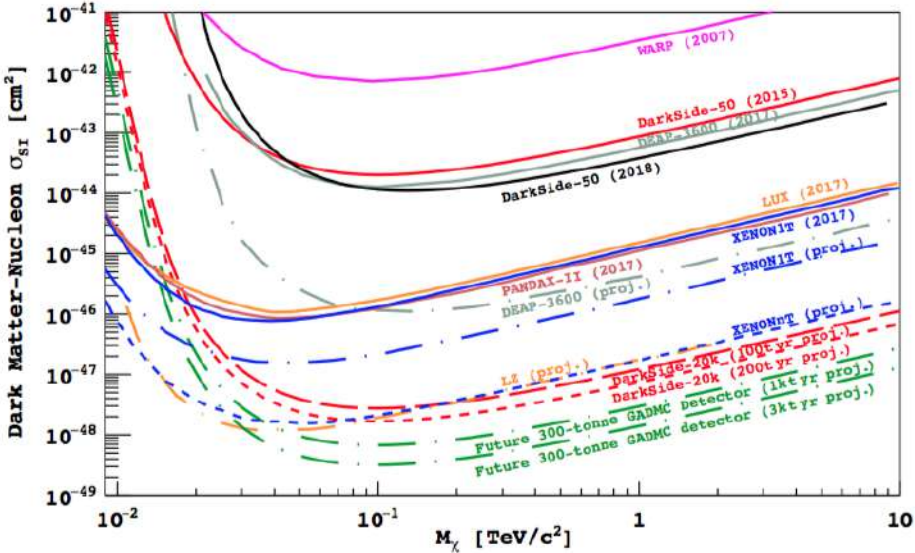


Figure 2.8: Upper limits for the spin independent WIMP-nucleon cross section at 90% C.L. from the recent results of DarkSide-50 compared with the projected sensitivity of DarkSide-20k and future detectors [51].

# Chapter 3

## The Recoil Directionality (ReD) Experiment

The long-term goal for the future direct dark matter detectors development, as seen in the previous chapter, is to reach the sensitivity set by the neutrino floor. It represents the dark matter sensitivity level where coherent nuclear scattering by atmospheric neutrinos provides one count of background. This sensitivity is considered the ultimate value achievable by direct matter searches in the absence of concurring measurements of the direction of the recoiling nuclei or temporal modulation. However, demonstrating that a possible detected signal is due to WIMPs is still possible if one can identify a signal from dark matter as opposed to many isotropic sources in the Universe. Direction-sensitivity is therefore a highly desirable characteristic for a direct detection experiment.

In this chapter, after an introduction on the physical goal, a proposed directional experiment, ReD (Recoil Directionality), will be discussed, while preliminary results will follow in the next chapters.

### 3.1 Recoil Directionality: the motivation

In the framework of the Standard Halo Model, if  $\mathbf{v}_i$  is the velocity of an upcoming WIMP of mass  $m_\chi$ , and  $\mathbf{u}$  is the velocity of a recoiling nucleus of mass  $m_N$  and momentum  $\mathbf{q} = m_N \mathbf{u}$ , and  $E_R = q^2/(2m_N)$  its energy, the Maxwell-Boltzmann WIMP velocity distribution in a reference frame with a velocity  $\mathbf{V}$  relative to the center of the Milky Way is:

$$f(\mathbf{v}) = \frac{1}{\sqrt{(2\pi\sigma_v^2)^3}} \exp \left[ -\frac{1}{2} \left( \frac{\mathbf{v} + \mathbf{V}}{\sigma_v} \right)^2 \right] \quad (3.1)$$

where  $\sigma_v$  is the width of the distribution in the reference frame. In order to make explicit the dependence on the minimum velocity of a WIMP that can transfer the momentum  $\mathbf{q}$  to a recoiling nucleus, and on the recoiling direction, it is more convenient to make a Radon transformation on the above equation:

$$\hat{f}(v_{min}, \hat{\mathbf{q}}) = \frac{1}{\sqrt{2\pi\sigma_v^2}} \exp \left[ -\frac{1}{2} \left( \frac{v_{min} + \hat{\mathbf{q}} \cdot \mathbf{V}}{\sigma_v} \right)^2 \right] \quad (3.2)$$

where  $v_{min} = \sqrt{2m_N E_R / (2\mu_N)}$ . Substituting the above equation in the 3.1, and integrating over the entire range of energy, it is possible to calculate the angle differential recoil rate per unit mass:

$$\frac{dR(E_{th}, E_{max}, \hat{\mathbf{q}})}{d\Omega_R} = \int_{E_{th}}^{E_{max}} dE_R \frac{d^2 R(E_R, \hat{\mathbf{q}})}{dE_R d\Omega_R}. \quad (3.3)$$

The integrand term in the above equation represents the double-differential recoil rate per unit mass as a function of the recoil energy of the nucleus ( $E_R$ ), and the recoil direction ( $\hat{\mathbf{q}}$ ):

$$\frac{d^2 R(E_R, \hat{\mathbf{q}})}{dE_R d\Omega_R} = \frac{\rho}{m_\chi} \frac{\sigma_{\chi-N} F^2(q)}{4\pi\mu_{\chi-N}^2} \hat{f}(v_{min}, \hat{\mathbf{q}}) \quad (3.4)$$

with  $\rho$  and  $m_\chi$  the WIMP density and the WIMP mass respectively,  $\sigma_{\chi-N}$  the total spin-independent WIMP-nucleus cross section,  $F(q)$  the nuclear form factor and  $\mu_{\chi-N}$  the reduced mass of the WIMP-nucleus system. The former depends on the velocity distribution through the  $\hat{f}(v_{min}, \hat{\mathbf{q}})$  term, that, by definition, depends on the velocity  $\mathbf{V}$ , that in turn depends on the reference frame. In particular, in a frame at rest with respect to the galactic center,  $\mathbf{V}$  is null by definition, so the recoil rate for an event measured in such a frame will be isotropic. If one considers a coordinate system at rest with respect to the Sun, on the other hand,  $\mathbf{V}$  represents the component of the velocity due to the motion of the Sun around the galactic center,  $\mathbf{V}_{SG}$ , in the direction of the Cygnus constellation<sup>1</sup>.

This represents a crucial point in the argument of the directionality: the effect of the motion of the Sun towards the galactic center is analogous to what would happen in case of the presence of an apparent WIMP wind coming from the opposite direction of this motion, i.e. the Cygnus constellation. Referring to the figure 3.1, it is interesting to note that the reddish region

<sup>1</sup>The component of the velocity  $\mathbf{V}$  due to the revolution motion of the solar system in the direction of the galactic center, in the framework of the SHM, is  $\mathbf{V} \simeq v_0 = 220$  km/s.

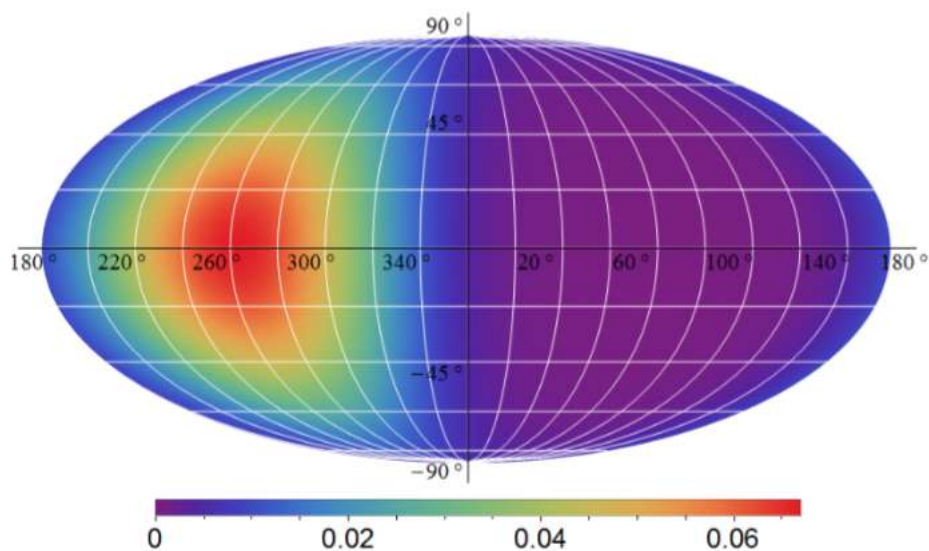


Figure 3.1: Mollweide plot of the differential recoil rate projected on a map of the celestial sphere in galactic coordinates. The energy range varies from 50 keV to 200 keV, the WIMP mass is  $200 \text{ GeV}/c^2$ , and the cross section of the WIMP-nucleus interaction is  $10^{-46} \text{ cm}^2$  [52].

shows a peak in the direction opposite to the Cygnus constellation, due to the WIMP wind, for a detector made with an argon target and considering a WIMP mass of about  $200 \text{ GeV}/c^2$ , a recoil energy in the range 50 keV - 200 keV and a WIMP-nucleus cross section of about  $10^{-46} \text{ cm}^2$  [52].

In a more realistic case, considering an Earthbound experiment, working with a reference frame at rest with the Sun is not the best choice one can make. So, for this reason, in the previous calculations, also the orbital velocity of Earth with respect to the Sun should be considered in order to have  $\mathbf{V} = \mathbf{V}_{\text{SG}} + \mathbf{V}_{\text{ES}}$ , with  $\mathbf{V}_{\text{ES}}$  orbital velocity of the Earth with respect to the Sun<sup>2</sup>. Furthermore, because of this motion, the annual periodicity of the motion of Earth around the Sun produces an annual modulation in the dark matter signal. The module of the total velocity,  $\mathbf{V}$ , changes during the year causing a similar effect on the expected dark matter flux. Indeed, the annual change of the WIMP average velocity produces a change, also, in the total annual rate that, depending on the position of Earth along its orbit, reaches a maximum around the end of May, and a minimum around the end of November. In addition, it has to be considered also the rotation

<sup>2</sup>In the framework of the SHM,  $\mathbf{V}_{\text{ES}}$  has the magnitude of about 30 km/s, about an order of magnitude smaller than the velocity of the Sun in the Cygnus direction.

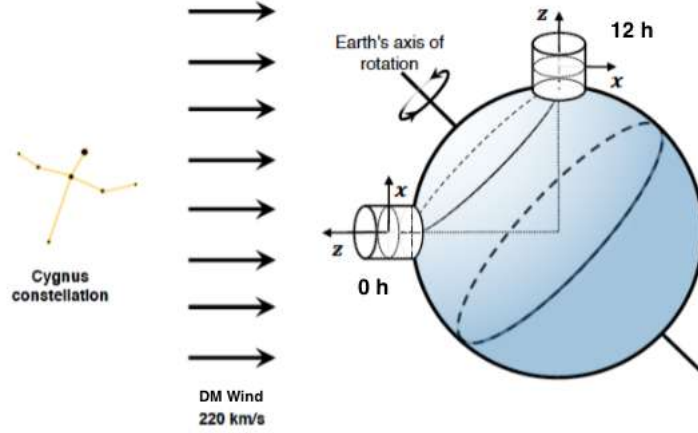


Figure 3.2: Drawing to show the variation of the total velocity  $\mathbf{V}$  during the sidereal day in a fixed Earthbound frame. The position of a dark matter detector is also sketched.

of Earth around its own axis in a so-called *sidereal day*<sup>3</sup>, so the direction of  $\mathbf{V}$  changes also during the day, as shown in the figure 3.2. Considering a reference frame that has the  $\hat{z}$  axis the direction towards the Cygnus constellation, the total  $\mathbf{V}$  at a given time  $t_0$  will be parallel to the axis, while 12 hours later it will be perpendicular to a hypothetical dark matter wind. Finally, a directional dark matter detector is mainly based on the study of the recoil events rate with respect to the recoil angle and the time of the day. As already said, if one considers a reference frame within the detector with the  $\hat{z}$  axis pointing toward the direction of the Cygnus constellation, the recoil angle  $\theta_R$  of a recoil nucleus is defined as the angle between the axis and the recoil direction of the nucleus after an interaction with a WIMP. If the detector is not able to distinguish between recoil tracks differing by  $180^\circ$ , the angular information is parametrized in the so-called *folded* angular recoil rate [52]:

$$\frac{dR_f(|\cos\theta_R|)}{d|\cos\theta_R|} \equiv \frac{dR}{d\cos\theta_R}(\cos\theta_R) + \frac{dR}{d\cos\theta_R}(-\cos\theta_R). \quad (3.5)$$

Events can so be distinguished as **vertical events** which recoils correspond to  $|\cos\theta_R| \geq 0.5$ , and **horizontal events** in the opposite case,  $|\cos\theta_R| \leq 0.5$ . The horizontal and vertical daily variation of the events rate, together

<sup>3</sup>By definition a sidereal day is the time difference between two culminations of the so-called  $\Upsilon$  point (a fixed point with respect to the stars on the sidereal sphere). The sidereal day is slightly shorter than a solar day, in fact one sidereal day is 23h56'04" long.

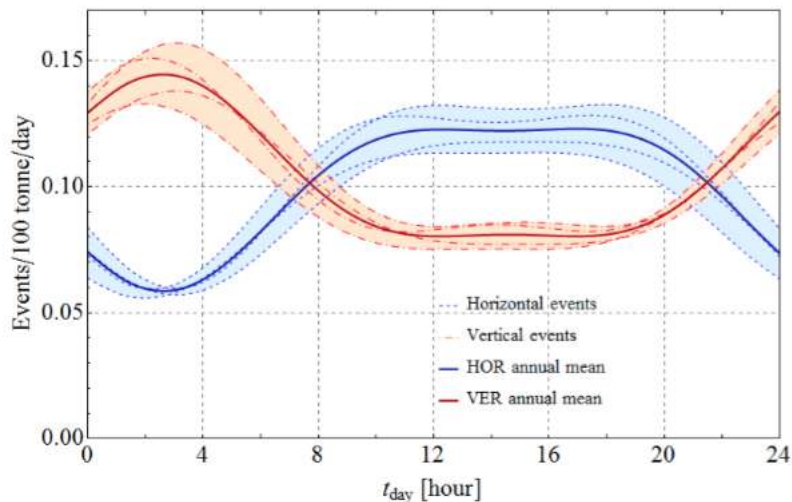


Figure 3.3: Horizontal and vertical daily variation of the events rate as a function of time for four different days during the year. Curves are calculated for a typical argon detector of 100 tonnes mass at the latitude of the Laboratori Nazionali del Gran Sasso [52].

with the annual average rates, is reported on figure 3.3. Here the trend is clear: between 0 and 8 hours vertical events show a peak, that means that the Cygnus constellation is at zenith, while on the other hand, between 10 and 20 hours, the trend is opposite (Cygnus constellation at the horizon) [52].

### Columnar Recombination

WIMP directional information is also potentially available, in a dual-phase Liquid Argon Time Projection Chamber (LAr TPC) by exploiting the columnar recombination effect. As already seen in chapter 2, in such a detector, recoiling nuclei cause argon excitation and ionization. Each event is then detected in two ways: the prompt scintillation light (S1), from the argon de-excitation, and the signal coming from free ionization electrons. The latter, thanks to an intense electric field, are drifted towards the top of the TPC, extracted into a confined argon gas pocket and accelerated by a second electric field. This acceleration produces, by electroluminescence, a secondary light pulse (S2). A fraction of free electrons, however, recombine with ions in the ion-electron cloud produced by the ionizing track itself, forming a short-lived excited diatomic argon molecules. These contribute directly to the S1 signal. Columnar recombination models [53, 54, 55] suggest that the

magnitude of the recombination effect should vary with the angle between the field and the track direction.

A difference in the electron-ion recombination effect is expected when the ionizing track is either parallel or perpendicular to the electric field. In the first case, the electrons have to drift in a *column* of ion-electron pairs, maximizing the recombination probability. On the other hand, in the latter case, the probability to cross the column is minimized, and so the recombination effects. In a more detailed view, one can say that the recombination mechanism takes place when an electron with a proper energy gets close enough to an ion. The distance for the electron capture is the so-called *Onsager radius*, the distance at which the electrostatic potential is balanced by the kinetic energy of the electron:

$$r_c = \frac{e^2}{\epsilon_r kT} \quad (3.6)$$

with  $\epsilon_r$  the dielectric constant of the medium. In liquid argon ( $T = 87$  K), the Onsager radius is about 80 nm that corresponds to a recoil energy of about 30 keV, so the necessary condition in order to have a directional signal in the framework of the columnar recombination, is that the recoil track exceeds the Onsager radius. Notice that, the value of 30 keV for the recoil energy is the energy region of interest for the detection of dark matter in the case of direct search [56]. The net effect of those recombinations is the reduction of the ionization signal S2, and the consequent enhancing of the primary scintillation pulse S1. Finally, S2 should have a maximum when  $\theta_R = 90^\circ$  and a minimum in the opposite case when  $\theta_R = 0^\circ$ , depending on the angle between the orthogonal component of the electric field and the recoil direction.

## 3.2 A hint to the directionality: the SCENE Experiment

The SCENE experiment [57] opened the possibility to build a dual-phase LAr TPC sensitive to the direction of nuclear recoils. Briefly, the SCENE detector is a small dual-phase LAr TPC exposed to a low energy pulsed neutron beam of the University of Notre Dame Institute for Structure and Nuclear Astrophysics. Protons from a Tandem accelerator hit a 0.20 mg/cm<sup>2</sup> thick LiF target in order to generate a narrow neutron beam through the nuclear reaction  ${}^7\text{Li}(p,n){}^7\text{Be}$ . Neutrons secondary beam were directed towards the TPC located 73.1 cm away from the LiF target during the first run (82.4

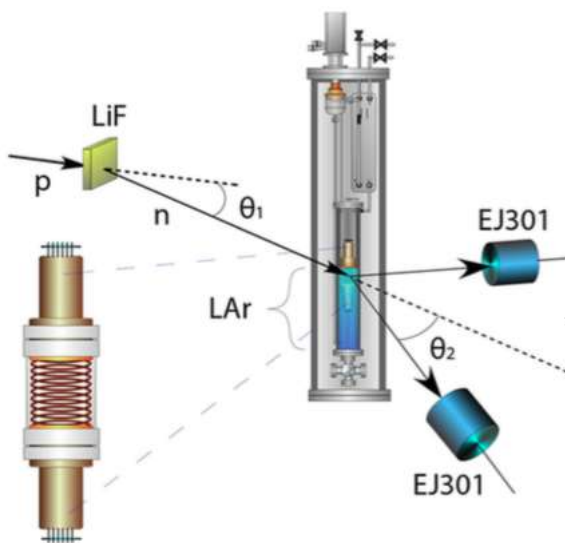


Figure 3.4: Drawing of the SCENE experimental apparatus [57].  $\theta_1$  is the neutron outgoing angle from the LiF target, while  $\theta_2$  is the recoil one after the interaction inside the LAr TPC (on the left) [57].

cm in the second one). After the interaction inside the active volume of the detector, the scattered neutrons were detected in three  $12.7 \text{ cm} \times 12.7 \text{ cm}$  cylindrical liquid scintillator neutron detectors, arranged on a circular stand at a distance of 71 cm from the TPC and at selected angles with respect to the primary beam line [57].

The goal of the experiment was to measure scintillation and ionization yields of recoiling nuclei in liquid argon as a function of the electric field applied to the chamber. In figure 3.5 are reported the results obtained in 2015 by the collaboration. They report scintillation yield (on the left) in the case of null fields, and ionization yield measurements (right panel) in case of an electric field was applied to the LAr TPC, for different nuclear recoil energies. In the figure are also reported the cases of nuclear recoil orthogonal (black line) and parallel (red line) with respect to the electric field. It is clear that, especially at nuclear recoil energy of 57.3 keV, there is an excess in the scintillation signal for nuclear recoil parallel to the field with respect to the orthogonal one [57].

This promising result pushes the DarkSide collaboration to further investigate the excess, given the importance it would have in the dark matter search with the future DarkSide-20k detector, with the design and the realization of a new prototype experiment, ReD (Recoil Directionality), to further scrutinize the hints given by SCENE but also to serve as a benchmark and key

### 3.2. A hint to the directionality: the SCENE Experiment

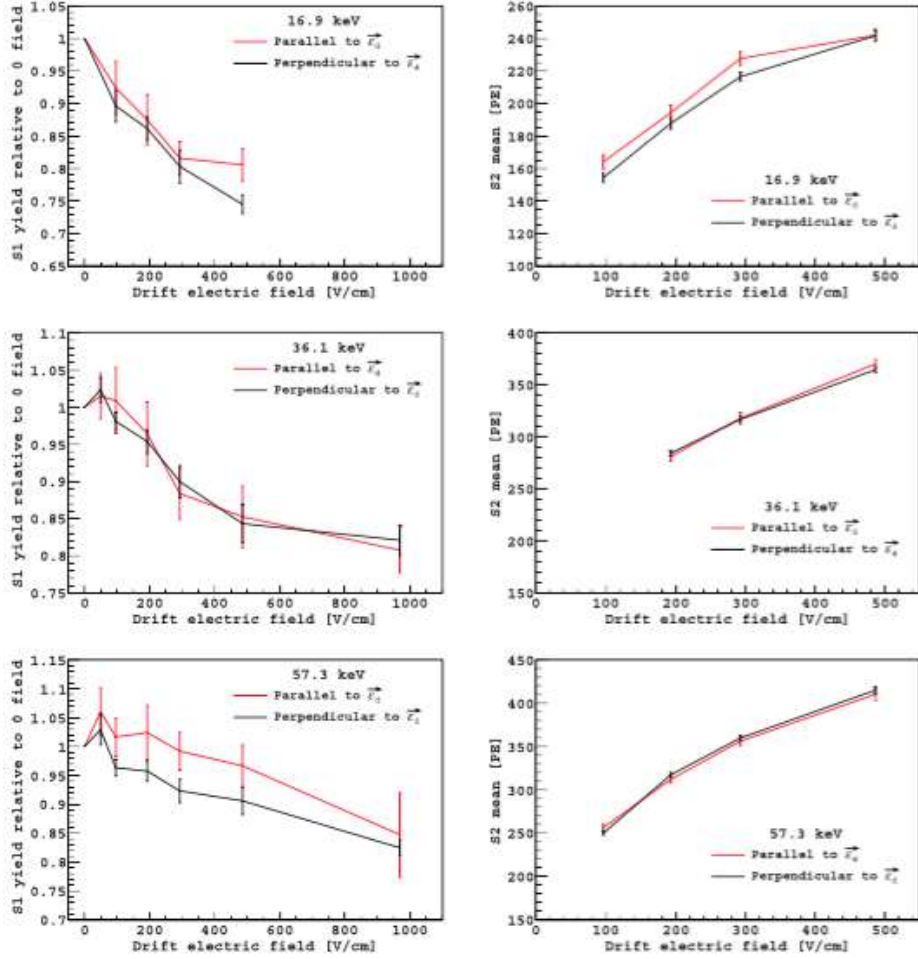


Figure 3.5: Scintillation (left panels) and ionization (right panel) yields from the SCENE experiment for nuclear recoils at different energies (16.9 keV, 36.1 keV and 57.3 keV respectively). The black line represents the case of nuclear recoil perpendicular to the electric field, while the red line is the parallel case [57].

test for the next generation of dark matter detectors.

### 3.3 The ReD Experiment

The main goal of the Recoil Directionality (ReD) experiment is to prove the directional sensitivity of a dual phase Liquid Argon Time Projection Chamber (LAr TPC). In this kind of detector it is possible to exploit the columnar recombination phenomenon of a nuclear recoil event by looking at the angle between the ionizing track and the electric field applied to the detector itself. Furthermore, since the promising results of DarkSide-50 detector on the low mass dark matter search by looking at the ionization signal (S2) only [49], ReD can contribute in the understanding of S2 for very low-energy events. The aim of the project is to irradiate the ReD LAr TPC with a neutron beam of known energy and direction by using the 15MV Tandem accelerator of the INFN - Laboratori Nazionali del Sud (LNS) in Catania, Italy. Neutrons are produced by means of the  $p(^7\text{Li},^7\text{Be})n$  two-body reaction in inverse kinematics, and then, thanks to the closed kinematics of the reaction, directed towards the TPC at an angle of about 22.3 degrees. Scattered neutrons are then detected by a neutron spectrometer made by nine 3-inch liquid scintillators neutron detectors located downstream of the TPC. Those detectors are positioned at fixed angles with respect to the primary neutron beam in order to detect neutrons that come out at different angles with respect to the electric field. This, together with the time-of-flight measurements and the pulse shape discrimination (PSD) of both the TPC and the neutron detectors, will allow a precise study of the dependence of the scintillation (S1) and ionization (S2) signals as a function of the angle between the recoil track and the electric field of the TPC. Moreover, it is possible to vary the energy of neutrons by varying the energy of the projectile of the main reaction. A drawing of the ReD geometrical scheme is shown in fig. 3.6.

As it is possible to note from the figure above, the ReD setup is mainly composed by three parts: the scattering chamber with the charged particle detectors, the LAr TPC and the neutron spectrometer. All of these components are capable to work independently each other, so one of the most challenging part of the experiment was to integrate them all together for the first time. In the following, a brief description of each component is presented together with Monte Carlo expectations. ReD, finally, saw beam in July 2018 and September 2018 for testing purposes, while a new physics run is foreseen early 2020.

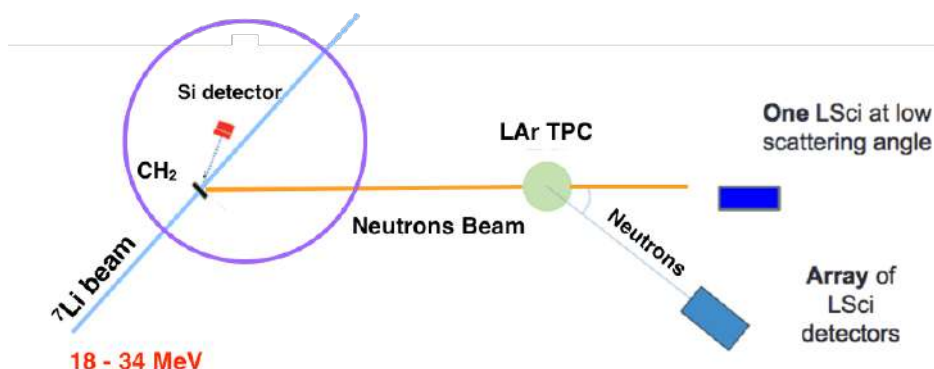


Figure 3.6: Drawing of the ReD geometrical scheme at LNS in Catania. Together with the scattering chamber (the big violet circle on the left part of the sketch), the neutron spectrometer (light blue box on the right bottom corner) and the low mass detector position (blue box on the right) are also represented. The light blue and the yellow lines are the  ${}^7\text{Li}$  and the neutrons beam line, respectively.

### 3.3.1 ReD: neutrons production and geometry

$p({}^7\text{Li}, {}^7\text{Be})n$  reaction is often used to produce quasi-mono-energetic and very collimated neutrons [58]. Since it has a negative  $Q$ -value (about  $-1.644$  MeV) and a threshold of about 13 MeV, increasing the beam energy opens up different exit reaction channels, in particular the first excited state of  ${}^7\text{Be}$  at 0.429 MeV with a threshold of 16.513 MeV, that corresponds to a 3.84 MeV neutrons, emitted at  $0^\circ$ , with a  ${}^7\text{Li}$  beam energy of 28 MeV. So, in order to exploit nuclear recoils between 20 keV and 100 keV (the range of interest in the direct search of dark matter experiments), it was chosen to operate the Tandem accelerator in order to produce lithium projectile energies from 18 MeV to 34 MeV, corresponding to neutron energies from about 3 MeV to about 10 MeV. Kinematical loci from the two-body relativistic calculations, made using a custom code, are shown in fig. 3.7, while angular distributions of neutrons ( $\theta_n$ ) and  ${}^7\text{Be}$  ( $\theta_{\text{Be}}$ ) are in fig. 3.8, where the red and black curves refer to the first  ${}^7\text{Be}$  excited state and to the ground state, respectively. It is also possible to note that, for this  ${}^7\text{Li}$  beam energy of 28 MeV, the maximum neutron emission angle is about  $47^\circ$  for the ground state beryllium, while it is about  $40^\circ$  for the 0.429 MeV excited state. Calculations also show that a value of  $\theta_n$  of  $22.3^\circ$ , corresponds to a neutron energy of about 7.4 MeV. The differential cross-section of the production reaction  $p({}^7\text{Li}, {}^7\text{Be})n$  in inverse kinematics, for a lithium beam of 28 MeV, in the case of a neutron exit angle of  $22.3^\circ$  is about 80 mb/sr [61, 62].

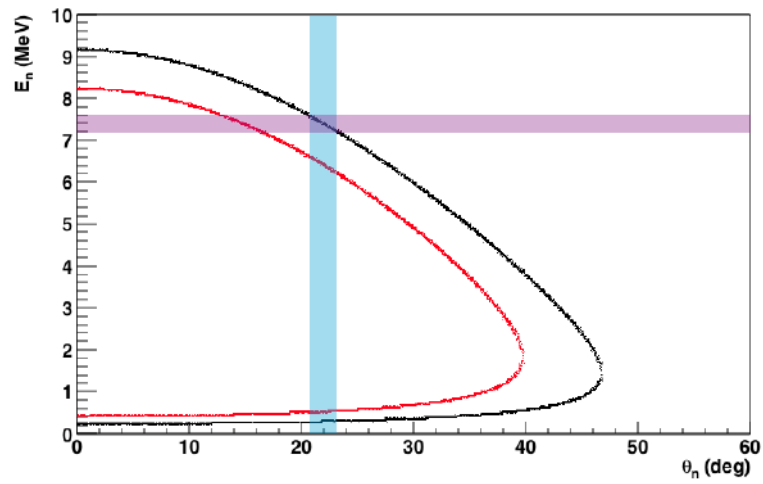


Figure 3.7: Kinematical loci of the  $p(^7\text{Li},^7\text{Be})n$  two body reaction at 28 MeV  $^7\text{Li}$  beam energy. It is shown, in particular, the energy of neutrons with respect to its emission angle. Red curve refers to the first excited state of  $^7\text{Be}$  (about 429 keV), while the black one to the ground state. The two colored bands are pictorially representations of the working range values chosen during the measurements (details in the text).

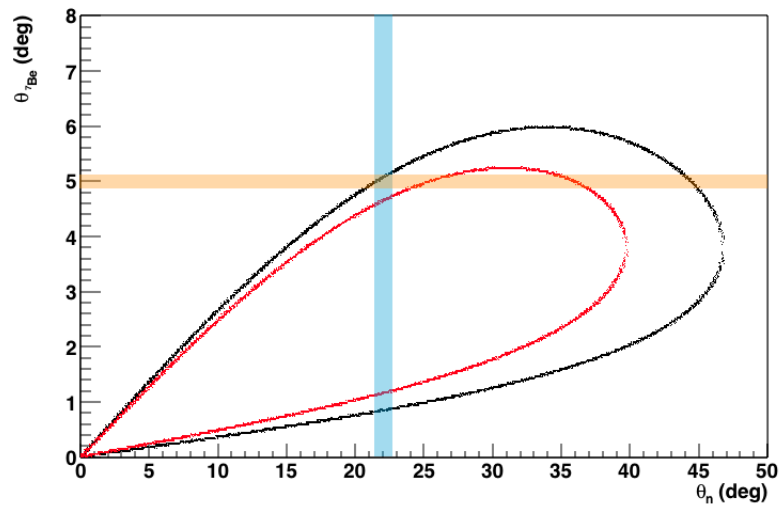


Figure 3.8: Angular correlation of neutrons and  ${}^7\text{Be}$  from the  $p({}^7\text{Li},{}^7\text{Be})n$  two body reaction at 28 MeV  ${}^7\text{Li}$  beam energy. The x axis shows, in particular, the exit angle of neutrons, while on the ordinate there is the  ${}^7\text{Be}$  emission angle. Red curve refers to the first excited state of  ${}^7\text{Be}$  (about 429 keV), while the black one to the ground state. The two colored bands are pictorially representations of the working range values chosen during the measurements (details in the text).

Finally, with the help of a custom made Geant4-based Monte Carlo simulation (G4DS, see the following), it was also possible to optimize the geometrical configuration of the experiment. In particular, in its final configuration, the TPC is located at 150 cm from the neutrons production target and at an angle of  $22.3^\circ$  with respect to the beam line. Since the 3-D configuration of the working space, the radial component of  $\theta_n$ ,  $\theta_{\text{TPC}}$  is defined as the angle between the beam line and the horizontal projection of the target - TPC vector (i.e. the neutron beam axis), and the azimuthal component  $\phi_{\text{TPC}}$  is the angle between the beam line horizontal plane and the neutron beam axis. Since  $\theta_n$  is  $22.3^\circ$ ,  $\theta_{\text{TPC}}$  and  $\phi_{\text{TPC}}$  are about  $12.8^\circ$  and  $18.4^\circ$ , respectively. Notice that, because of this particular geometrical configuration of the experimental setup the reaction plane is tilted, the inclination to be about  $56.37^\circ$  with respect to horizontal. Furthermore, the latter is a necessary condition in order to tag recoil angles parallel with respect to electric field.

### 3.3.2 ReD: inside the scattering chamber

The scattering chamber used in Catania is a 55 cm height stainless steel cylinder with a radius of 30 cm and 2 cm thick. It allows to allocate a stainless steel target holder with eleven different targets mounted on it, and three different silicon detectors for the detection of the charged particle that comes out from the two body reaction  $p(^7\text{Li}, ^7\text{Be})n$  (fig. 3.9). Since the Tandem accelerator at LNS cannot be operated in pulsed mode, it was necessary to have a hardware trigger for the time-of-flight (ToF) measurement and, at the same time, to allow for a better signal-to-noise discrimination. In this case the proper tag time for the event detection comes from the detection of the  $^7\text{Be}$  charged particle associated to the neutron production. Two silicon detectors are then placed at about  $5^\circ$  ( $\theta_{^7\text{Be}}$ ) from the beam line at a distance of about 46.5 cm from the target in the so-called telescope arrangement, while the azimuthal angle ( $\phi_{^7\text{Be}}$ ) was fixed by the using of different sets of thin aluminum collimators (the nominal one has a 3 mm diameter hole and 2 mm thickness). These were also used in order to prevent radiation damage of the silicon sensitive areas of the detectors. In this configuration one has a thinner detector followed with a thicker one in order to be able to reconstruct the  $\Delta E$ -E matrix that allows the Z identification (fig. 3.10). In the first stage of the telescope (the thinner  $\Delta E$ ) in fact, the charged particle loses its energy while it stops in the second stage. By means of the Bethe-Bloch relation, one is able to identify the impinging particles and to reconstruct their energy. In the case of ReD this technique allowed for the correct identification of the  $^7\text{Be}$ ,  $^7\text{Li}$  and other beam-related background components,

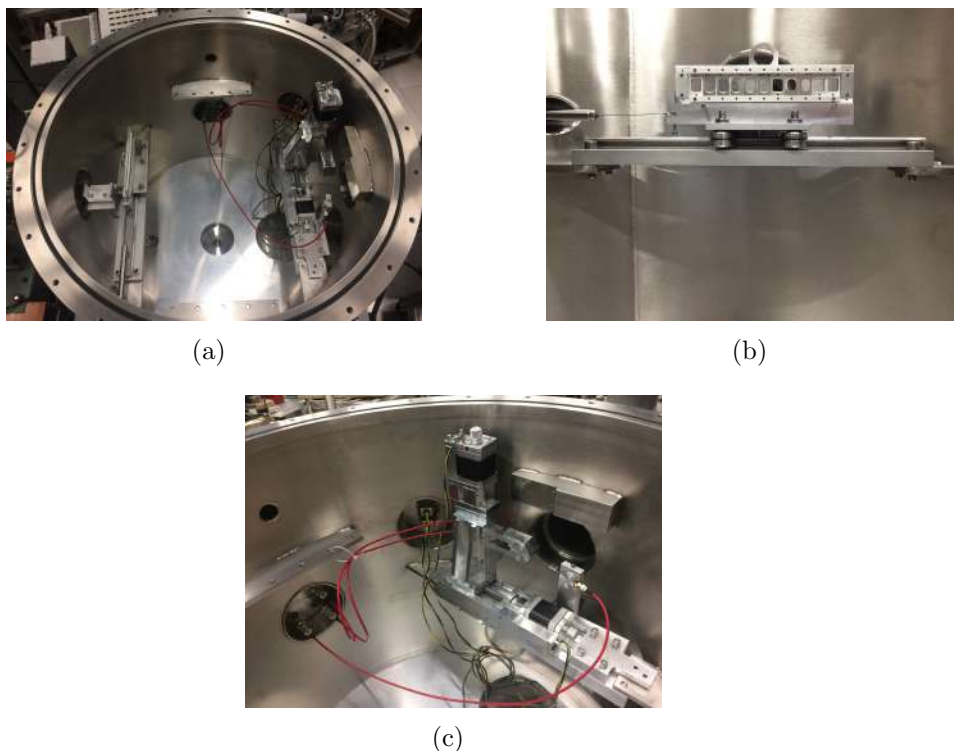


Figure 3.9: (a) Internal view of the scattering chamber during a mounting phase. It is possible to see the targets holder on the left and the silicon detectors mounted on the precision motor system for their correct positioning. (b) The holder and the targets used during a test beam at LNS. (c) The silicon detectors mounted on the movement system used during a test beam at LNS, details in the text.

and the correctness of the assumption of the neutron production with fixed energy and exit angle thanks to the closed kinematics of the reaction. During the run performed in July 2018 two ORTEC TB-series 50 mm<sup>2</sup> sensitive area Si-detectors of 20  $\mu\text{m}$  and 200  $\mu\text{m}$  for the  $\Delta E$  and E components of the telescope respectively were used. During the September 2018 run, in order to have a hint of the beam current impinging on the target, the Si-detectors configuration changed: the 200  $\mu\text{m}$  detector was used as a beam current monitor (placed at an angle of 23° with respect to the beam line<sup>4</sup>), while the Si-telescope was made by the same 20  $\mu\text{m}$  detector of July for the  $\Delta E$  stage coupled with a 1000  $\mu\text{m}$  one for the E. Furthermore, during a new

<sup>4</sup>At this angle, elastic scattering  ${}^7\text{Li} - {}^{12}\text{C}$  is dominant, so the aging of  ${}^{12}\text{C}$  from the target can be used as a good beam current estimator.

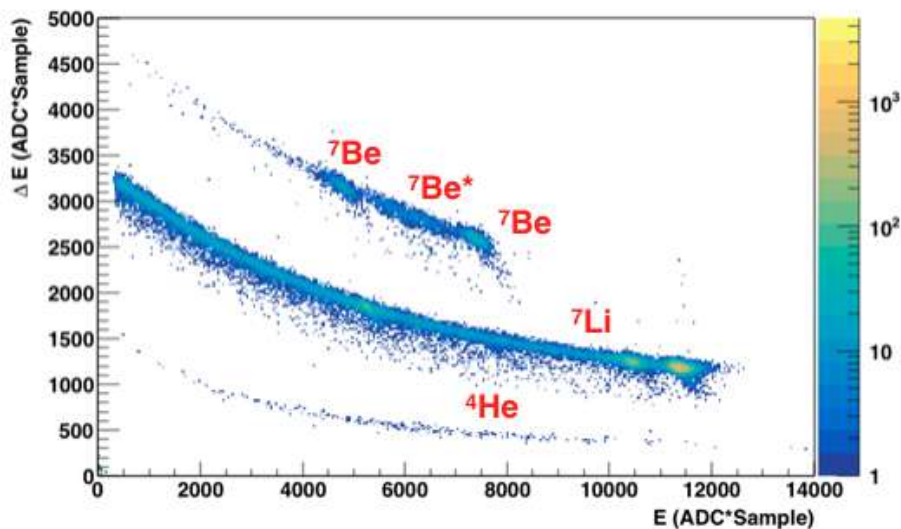


Figure 3.10: Scatter plot of the matrix  $\Delta E$ - $E$  of a run taken during the test beam campaign taken as a sample. It is possible to distinguish different traces for different particles that lost their energy in the Si-telescope (see the text for details).

testing phase in July 2019, the silicon detectors were mounted on a precision motor movement system that allows for their fine positioning with a tenth of millimeter precision. The signals coming from each of the detectors were finally sent to three ORTEC-142 pre-amplifiers modules that provided a fast rise time signal (the so-called time signal) useful to perform timing measurements, and a slower one, called energy signal, to have an improved energy resolution. The fast signal was finally sent to a NIM module for the fast amplification and then to a CAEN daisy chain for the acquisition. The fast signal only takes part to the trigger logic.

### 3.3.3 ReD: TPC and cryogenics

Figure 3.11 represents a picture of the ReD Liquid Argon Time Projection Chamber (LAr TPC) during a mounting phase in Catania. It was designed and built by the University of California Los Angeles (UCLA) group of Dark-Side project, it has a squared shape of 5 cm length  $\times$  5 cm wide  $\times$  6 cm height and its inner volume is enclosed by two acrylic windows, one on the top and one on the bottom, 4.5 mm thick, and by a reflecting sandwich-style structure of acrylic on the walls. This consists in two acrylic plates of 1.5

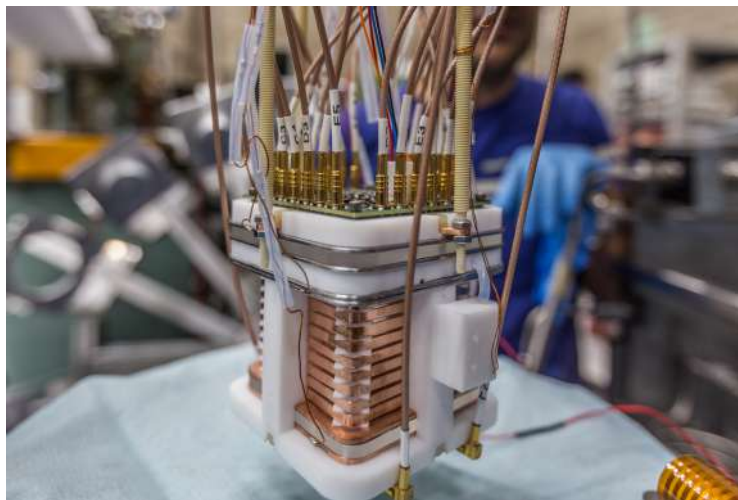


Figure 3.11: A picture of the ReD Liquid Argon Time Projection Chamber (LAr TPC) during a mounting phase in Catania. It is possible to note its teflon pillars structure, the field cage (copper rings that provide homogeneous electric field), the bubbler with the gas inlet tube that provides the formation of the gas pocket and the 28 signal cables from the SiPMs channels.

mm thickness with a 3M Enhanced Specular Reflector film (3M<sup>TM</sup> ESR) in between that enhances the light amount inside the detector and, more important, avoids the use of the PTFE reflector which is a proven Cherenkov background source [27], useful in particular in the case of background minimization for the future DarkSide-20k detector. Since argon scintillation emits 128 nm VUV photons, in order to be detected by the optical sensors, this light has to be converted in the visible range: this is done thanks to the evaporation on both the windows and all around the walls of the TPC, of a thick layer of *Tetraphenyl Butadiene* (TPB) wavelength shifter (the thickness can vary from about  $160 \mu\text{g}/\text{cm}^2$  to about  $200 \mu\text{g}/\text{cm}^2$ ). Finally, in order to use each window as electrodes for the electric field formation, each of them is coated with a 25 nm thick of *Tin-Indium-Oxide* (ITO) as the DarkSide-50 detector.

In order to establish and maintain the electric field inside the TPC, its active volume is bounded with nine copper shaping rings, the so-called field cage, at a distance of 0.5 cm each other. This will ensure the homogeneity and the uniformity of the drift field. In the standard configuration, three different fields are established inside the TPC: a drift and an extraction field at 200 V/cm and 3.8 kV/cm, respectively in liquid, and a multiplication or electroluminescence field of 5.7 kV/cm in the gas region. In order to main-

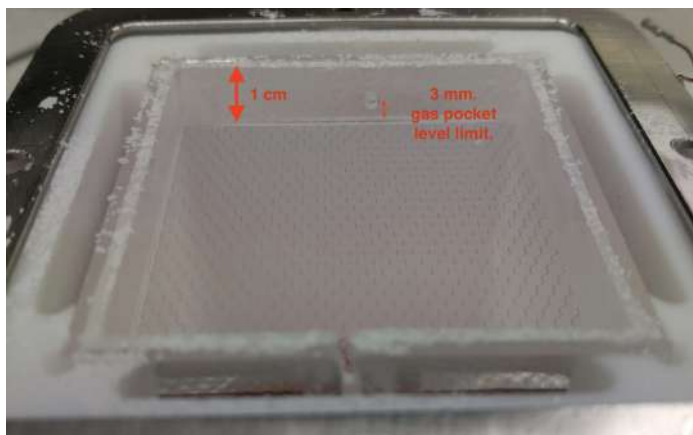


Figure 3.12: A picture of the top view of ReD TPC taken during a maintenance phase. The squared PTFE frame in this picture (the white squared box) is the so-called diving-bell, while the inner piece is the active volume of the TPC (the sandwich in the text). In the upper part of the picture it is clearly visible the hole of the overfull system, while in the opposite side there is an inlet that allows the entrance of the argon gas into the active volume of the detector. The hexagonal cells grid is also visible.

tain a higher extraction field in the gas and allow a field discontinuity in the liquid gas interface, inside the active volume of the TPC and at a distance of about 1 cm from the anode window, there is also a  $50 \mu\text{m}$  thick stainless steel etched mesh made by hexagon cells with a 95% transparency. The gas pocket is created by means of a bubbler (the external box in the fig. 3.11) that, thanks to a PT-1000 resistor, boils the liquid argon and force it to be released (by a teflon inlet tube) inside the so-called diving-bell: a narrow region inside the detector between the external PTFE frame and the active volume from which the gas reaches the active volume of the detector (fig. 3.12). The height of the gas pocket is mechanically fixed at 7 mm because of the presence of a hole in the diving-bell that acts as an overfull system. So, in the double phase configuration the TPC has a 5 cm maximum drift length (the distance between the grid and the cathode), a 3 mm thick layer of liquid argon above the grid that in the standard configuration operates at a 0 voltage potential, and finally a 7 mm thick gas layer. Finally, the PTFE supporting structure of the TPC is hanged to the cryostat main flange by the use of four threaded rods (fig. 3.11).

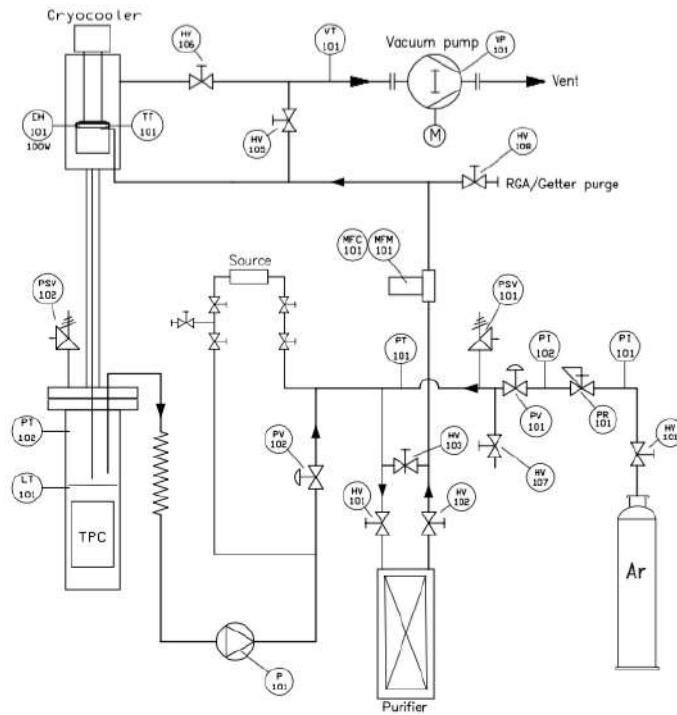


Figure 3.13: Drawing of the ReD cryogenic system. Argon gas from a commercial bottle is pushed inside the condenser where liquid is produced by means of a cold head connected to a cryocooler. Liquid argon then drops inside the cryostat which contains the TPC. During a regular data taking phase, the pump P101 on the bottom of the drawing provides recirculation of the gas through the purifier and once again into the condenser in a continuous loop.

### The cryogenic system

ReD is equipped with a custom made cryogenic system developed by the Criotec company. This system allows the liquefaction of commercial 6.0 gas argon, its recirculation inside the system and the purification. The entire system, including electronics and electrical connections, is deployed into a cart which allows the system to be moved.

Following the fig. 3.13, during the filling phase, the argon gas from a commercial bottle is pushed into the system. Here, through a Mass Flow Controller (MFC), it reaches the condenser where it is cooled down by the presence of a copper cold head. Then, the gas enters the dewar where the ReD TPC is allocated: continuous circulation of gas argon with increasingly lower temperature together with the cool down of all the mechanical components allows for the liquefaction of argon. The dewar is a double wall container that hosts the TPC and the liquid argon. It has a conical shape and its internal diameter varies from about 13 cm at the bottom to about 25 cm at the top where it is closed by a CF250 flange. For the purposes of the experiment, about 30 cm of liquid argon are produced inside the dewar, a level that in standard conditions is reached in about 12 hours of continuous cooling down. Once the level inside the dewar reaches the desired value, the system is switched to the recirculation mode. The argon gas flow is stopped and, by means of open/closing valves, the argon vapor is pushed through a recirculation pump inside the purifier system. Here the argon gas is purified and then pushed again into the system, and the loop can start again.

#### 3.3.4 The ReD optical readout

The ReD TPC is the first TPC equipped with cryogenic Silicon Photomultipliers (SiPMs). SiPMs are constituted by several so-called Single Photon Avalanche Diodes (SPADs) that, connected together in parallel, work in Geiger mode, i.e. every time a photon generates an electron/hole pair, they are drifted by an electric field in the multiplication region where they induce an avalanche. The voltage at which the avalanche is triggered is the so-called breakdown voltage [59]. So, usually SPADs work a few volts above this threshold value:

$$V_{bias} = V_{bd} + V_{ov} \quad (3.7)$$

where  $V_{ov}$  is the so-called over voltage value. Since the discharge is self-sustaining, a quenching resistance is placed in series with every single SPAD so that, after the discharge phase, the diode recharges in order to be ready for the detection of a new signal. Basically a SPAD is a binary device, so it is common in the application to group thousands of them to have a SiPM

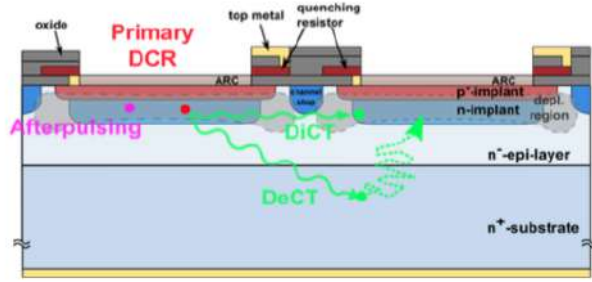


Figure 3.14: Schematic representation of noise generation in SiPMs in two adjacent SPADs (sketched in a cross section view) [59].

of few millimeters.

Signals that come from SiPMs presents a fast rise, of the order of few nanoseconds, followed by a slower tail, of the order of  $\mu s$ , depending on the recharge time of the devices. Compared with standard PMTs, SiPMs have also higher gain (in a range between  $10^5$  and  $10^7$ ) and better Photon Detection Efficiency (PDE). PDE is defined as:

$$PDE = QE \times P \times \epsilon_{geom} \quad (3.8)$$

with QE quantum efficiency, i.e. the probability for an incident photon to generate an electron/hole pair, P the generating avalanche probability and  $\epsilon_{geom}$  geometrical efficiency of the devices. PDE increases also with the increasing of over voltage bias [59].

Several mechanisms can contribute to noise in SiPMs (fig. 3.14). The main one is the so-called Dark Count Rate (DCR). It comes from the generation of electrons even in absence of hitting photons. Those electrons are able to produce avalanches and the resulting signal is almost identical to the one produced by a “real” photon. DCR decreases with decreasing temperature but it also increases with the increasing over voltage bias, so it is crucial to have a good estimation of  $V_{ov}$  at cryogenic temperature in order to have the least possible DCR. Other sources of noise in SiPMs are the correlated noises, and they are mainly optical cross-talks and afterpulsing. While the former are generated by photons that are produced during an avalanche that can in turn trigger an avalanche in a near SPAD, the latter generates when, during an avalanche, electrons are trapped by impurities in the silicon lattice of SPAD and then released generating another avalanche. Since afterpulses generate in the same cell of a primary event, it is possible to distinguish them by the identification of the time delay and the amplitude of the pulse. They also increase as the over voltage bias increases.

Furthermore, optical cross-talks can be distinguished in two different types:

- direct cross-talks (DiCTs): are produced when a photon triggers an avalanche in a neighboring SPAD producing a secondary avalanche. The event generated by a DiCT is indistinguishable from a primary event, so the signal will have an amplitude of at least two photons even if only one of them was absorbed;
- delayed cross-talks (DeCTs): are due to photons absorbed in the non-depleted region of a neighboring SPAD. Since the electrons have to drift in the high field region before to trigger an avalanche, it is in general possible to distinguish a delayed pulse from the primary one. Typical time for the formation of a DeCT is of the order of few to tens of nanoseconds.

As the other sources of noise, cross-talks, direct and delayed one, increase with over voltage because higher gains correspond to a high number of generated carriers.

The ReD LAr TPC uses  $11.7 \times 7.9 \text{ mm}^2$  NUV-HD rectangular shape SiPMs with maximum PDE at about 420 nm in the near UV region of electromagnetic spectrum. The SiPMs are made by *Fondazione Bruno Kessler* (FBK) in Trento, Italy, and they have triple doping concentration together with a  $25 \mu\text{m}$  cell pitch and a  $10 \text{ M}\Omega$  quenching resistance. They are assembled in

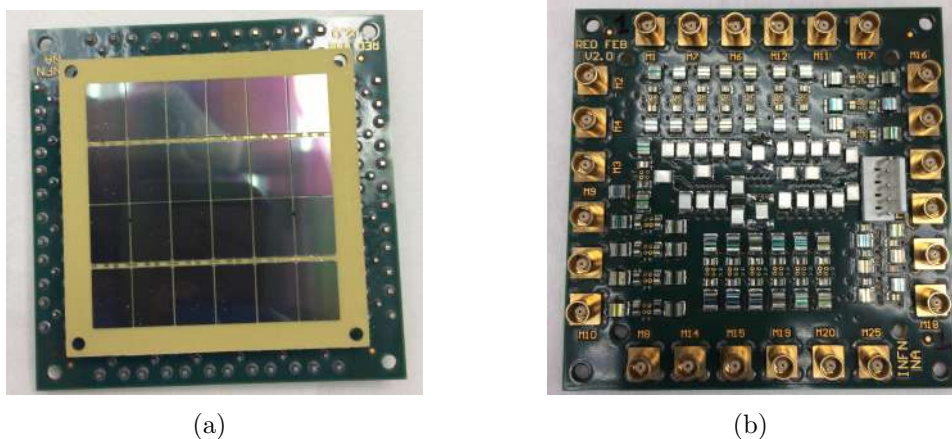


Figure 3.15: (a) Front view of one of the NUV-HD SiPM tiles used for the ReD experiment. It has a rectangular shape and is made by 24 SiPMs bounded together by several micro length wires. (b) Top view of the top Front-End Board (FEB) with 24 channels read-out, made in Naples with the collaboration of INFN - LNGS and INFN - Bologna groups of DarkSide collaboration.

two different tiles, as shown in fig. 3.15(a), (top and bottom of the TPC (sec.

3.3.3)) coupled with two different Front-End Boards (FEBs) (fig. 3.15(b)) for the electronic read-out, and both operated at +7 V of over voltage bias. The FEBs in ReD are in charge to distribute the voltages to the SiPMs and to amplify the output signals. They are coupled directly to the tiles. The bottom tile, in particular, is arranged in such a way to group the SiPMs in four groups each made by six SiPMs, coupled in series and then summed in parallel, each other. They are also amplified with an independent low-noise Transimpedance Amplifier (TIA). The output read-out is made by a four channel FEB realized at INFN - LNGS used at the  $V_{bias}$  of 68 V. On the other hand, the top tile has a single-SiPM read-out in order to improve the xy resolution on the ionization signal. In this case the SiPM matrix is coupled with a 24 channel FEB read-out designed and realized by the INFN - Napoli in collaboration with INFN - LNGS and INFN - Bologna groups of the DarkSide collaboration. As shown in fig. 3.15(b) it has 24 MCX connectors for cabling each single SiPM of the tile. Finally, as described in the following, the SiPMs are biased via a CAEN SY 5527 power supply module, while signals are acquired, digitized and stored via two CAEN V1730 Flash ADC boards 16 channels each and 500 MHz sampling rate.

### 3.3.5 ReD: the neutrons spectrometer

The neutron spectrometer used in ReD is an array of nine 3-inch liquid scintillator (LSci) detectors coupled with standard PMTs (fig. 3.16). Each component, made by the SCIONIX company, contains a commercial organic liquid scintillator mixture EJ-309 from Eljen Technology and is coupled with a 3-inch ETL 9821 PMT. The holding structure of the array, custom made by INFN - Cagliari, allows the placement of the neutron detectors on the base of a cone with the vertex on the center of the TPC and the main axis centered on the target-TPC direction. The opening angle of the cone is equal to the neutron scattering angle of  $\theta'_n = 36.8^\circ$ . This kind of configuration allows the simultaneous detection of scattered neutrons coming from the TPC with fixed recoil energies but different azimuthal angles  $\phi_{LSci}$ . As described in the table 3.1, this allows to tag different Ar recoil angles with respect to the electric field applied to the TPC (see par. 3.1).

Finally, among the nine LSci detectors, one of them (LSci #0) is devoted to the low energy recoil measurement, so it is not positioned in the same configuration of the others but, in normal conditions, at about 97 cm from the center of the TPC in the lowest central point of the holding structure. The angle between the target-TPC direction and target-LSci #0 direction is about  $3^\circ$ .

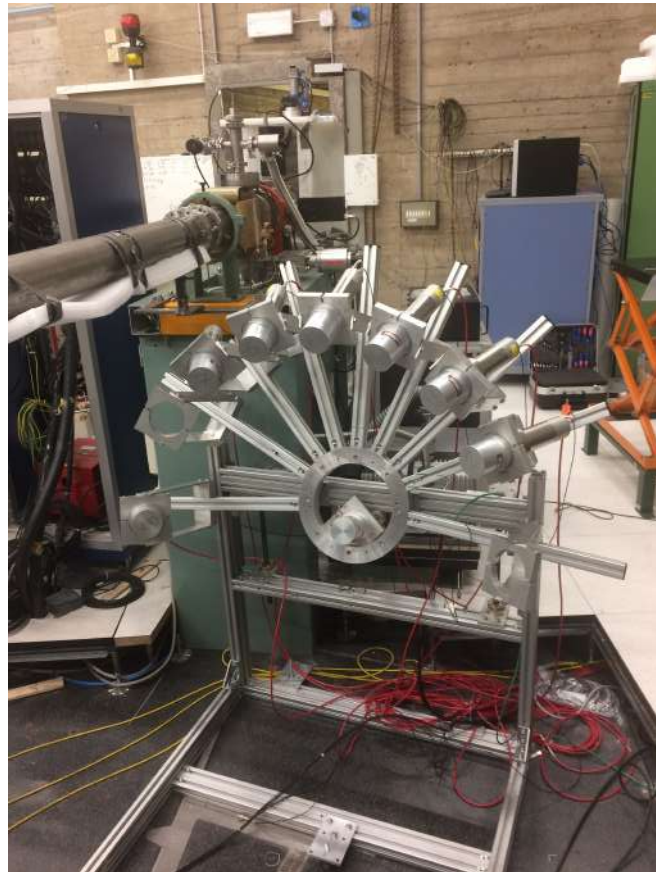


Figure 3.16: Photo of the neutron spectrometer used in ReD. As mentioned in the text it is made by nine 3-inch neutron liquid scintillator detectors arranged on a custom made structure at fixed angles with respect to the TPC. This photo, in particular, was taken during a calibration phase of the spectrometer, so only eight neutron detectors are shown, while one of them is placed at low recoil angle.

$\theta_n$ (deg)	$\phi_{LSci}$ (deg)	$d_{TPC-LSci}$ (cm)	$\theta_R$ (deg)
36.8	83.6 - 276.4	80	90
36.8	116.4 - 243.6	80	60
36.8	137.7 - 222.3	80	40
36.8	158.9 - 201.1	80	20
36.8	180	80	0

Table 3.1: Positioning angles of the ReD neutron detectors. As mentioned in the text they correspond to the same neutrons recoil angle (about  $36.8^\circ$ ) but different azimuthal angles  $\phi_{LSci}$ .

### 3.3.6 Data Acquisition and software

The ReD Data Acquisition (DAQ) system is made by three CAEN V1730 Flash ADC boards, 16 channels each with a 14-bit resolution, a  $2 V_{pp}$  input range and 500 MHz sampling rate. SiPMs are supplied by a CAEN SY 5527 power supply module together with two Agilent 32250A for the FEBs biases, while a CAEN 1471 power supply module is used to set-up the fields of the TPC. A Lakeshore 336 Temperature Controller is also used to monitor the liquid argon temperature inside the cryostat, while a Keithley 2280S allows to create and control the gas pocket inside the TPC. Trigger logic is set-up by using a standard NIM logical module by ORTEC coupled with a Lecroy 428F linear FAN-IN/FAN-OUT module (fig. 3.17). All the sub-systems are, finally, remotely controlled by a Slow Control system developed and maintained by the INFN - Genova group. This, via an user-friendly graphical interface developed in LabView language, allows the operator to control all electronic components of the system and to monitor all parameters of the cryogenic system, too, saving all the important parameters of the experiment in a proper database.

The DAQ software is a custom made version of the PADME experiment [60] code which allows the data taking via a graphical interface. Several trigger conditions can be set by changing some parameters inside a configuration file of the software: a typical single phase run, for example, is taken with a  $20 \mu s$  long window with a  $6 \mu s$  pre-trigger, while during a double phase run (in which the TPC operates both in ionization and scintillation mode), the acquisition window is larger, about  $100 \mu s$  with  $10 \mu s$  of pre-trigger. The pre-trigger is used for the baseline estimation that is then subtracted to the total integral of the signal. Data acquisition rate, generally, is limited to 40 MB/s by disk access, the best limit available with the disk mounted on the DAQ machine. Raw data are then stored in three different machines

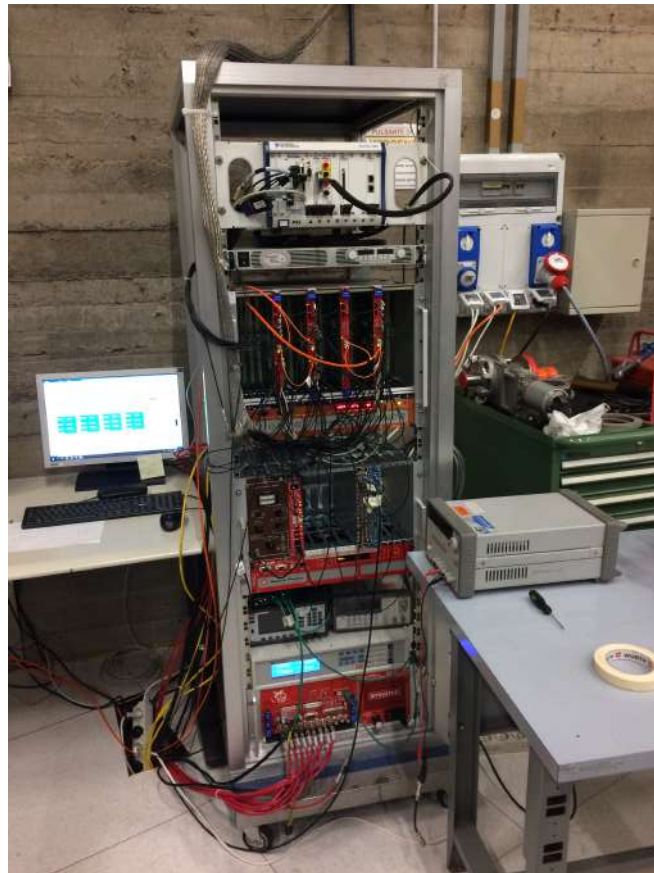


Figure 3.17: Photo of the DAQ system used in Catania during a test phase. See the text for details.

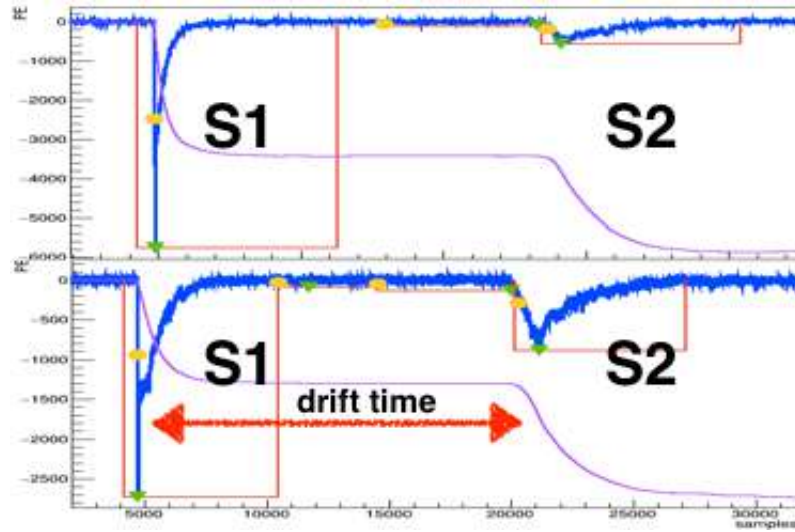


Figure 3.18: Raw waveforms of ReD experiment as computed by the low-level reconstruction algorithm. Note the difference in shape and in time of the scintillation (S1) and ionization (S2) signals, as described in the text.

for security reasons: INFN - Roma Tre tier and INFN - CNAF (both on disk and on tape) tier1, who provides, at the moment of writing, very large amount of disk space (of the order of Petabyte). Finally, ROOT trees are created via a custom made reconstruction software developed inside the ReD working group (at which the author of this dissertation also contributed), and the output files made available to the entire DarkSide collaboration for the offline and high-level analysis. Two typical raw waveforms with some low-level analysis performed with the reconstruction algorithm are displayed in fig. 3.18.

### 3.4 Monte Carlo expectations

Monte Carlo simulations were performed in order to have an indication on the expected rates, on the recoil neutron energies inside the TPC and a cross-check of the geometrical configuration. The author of this dissertation also contributed to develop and maintaining a custom made Geant4-based application in the framework of the Geant4-based Monte Carlo code used inside the DarkSide collaboration (G4DS [47]). The ReD branch of the code, other than the complete geometrical setup of the experiment, also contains the physics of ReD with a particular attention on the neutrons production cross sections for the involved reactions. The code was, in fact,

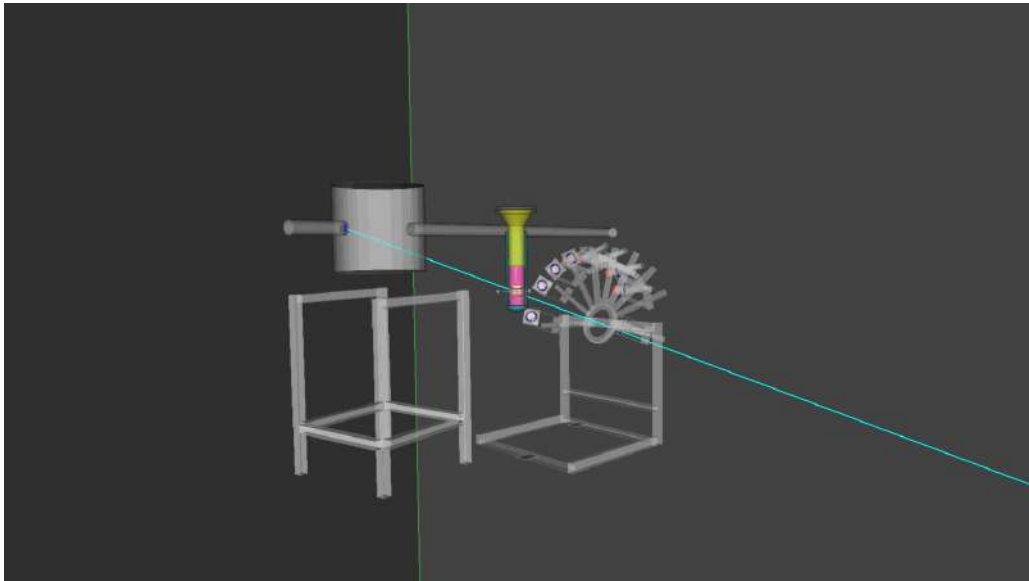


Figure 3.19: Rendering of the Geant4-based custom made application for ReD simulation. It is possible to note the presence of the scattering chamber, the TPC inside the cryostat, the beam line and the neutron spectrometer. The light blue line represents the neutron incoming direction towards the TPC, while the blue rectangle, from which the neutron track departs, is the  $\text{CH}_2$  target for the production of the neutrons and the pink region inside the cryostat represents the liquid argon level.

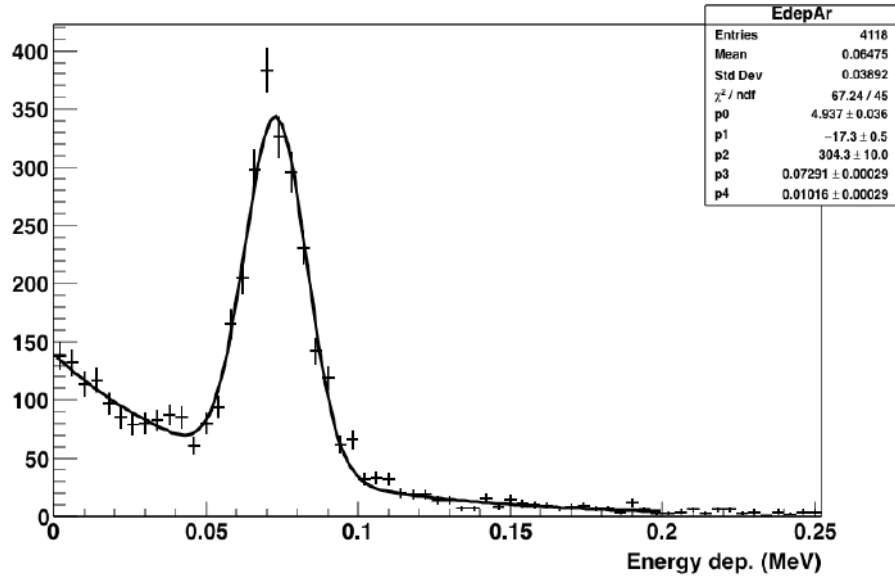


Figure 3.20: Simulated spectrum of the energy deposition in liquid argon. Neutrons produced via the  $p(^7\text{Li}, ^7\text{Be})n$  two-body reaction, for a 28 MeV projectile energy, deposit about 70 keV in liquid argon. Data are fitted with a sum of a Gaussian distribution plus an exponential function (black solid line).

used, not only for the finalization of the design of the scattering chamber and the other hardware components, but also in order to exploit all the possible neutrons production channels within the requested specifications of the experiment. Fig. 3.19 shows, for instance, a rendering of the complete setup in the Catania configuration. It contains the scattering chamber, the cryostat and the TPC, the beam line for the beam induced background evaluation and the neutron spectrometer. The  $\text{CH}_2$  target for the production of the neutrons and the liquid argon inside the cryostat are also shown (tiny blue rectangle at the beginning of the scattering chamber and the pink region inside the cryostat, respectively). So, in order to have a measurement for directionality, ReD looks for triple coincidences from silicon telescope inside the scattering chamber, TPC neutron scattering and neutrons tagged in the neutron spectrometer. A simulated spectrum of the energy deposition in liquid argon is shown in fig. 3.20: a  $^7\text{Li}$  beam of 28 MeV produces neutrons of about 7 MeV at about  $22.3^\circ$  (see par. 3.3) with respect to the neutron beam axis that deposit about 70 keV in liquid argon.

The expected neutrons rate per unit time is a function of the following

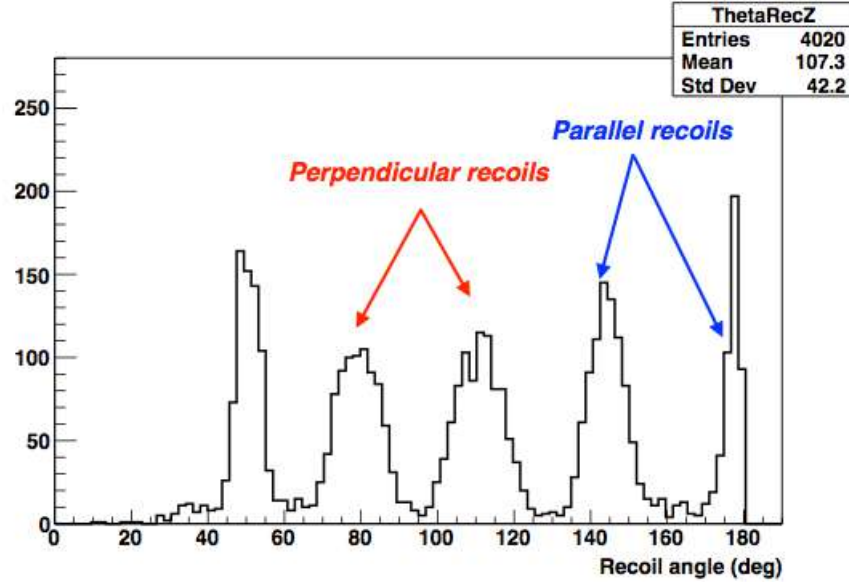


Figure 3.21: Simulated spectrum of the argon recoil angles after the interaction with neutrons in the active volume of the TPC. Red and blue arrows point to perpendicular and parallel recoils with respect to the electric field, respectively.

parameters:

- the beam current  $\frac{dN}{dt}$ ;
- the number density of protons in the target  $\rho_H$ ;
- the thickness of the target  $d_t$ ;
- the  $p(^7\text{Li}, ^7\text{Be})n$  differential cross section  $\frac{d\sigma}{d\Omega}$ , and
- the solid angle subtended by the TPC with respect to the target interaction point  $d\Omega_{TPC}$ .

So, entering the above defined parameters in the simulation, and assuming a current beam of 3 nA (about  $6.25 \times 10^9$  particles per second, pps) and a reference  $\text{CH}_2$  target of  $300 \mu\text{g}/\text{cm}^2$ , giving the already mentioned beam energy and reaction cross section, a neutrons rate of about 12 Hz crossing the active volume of the TPC is expected. From the same Monte Carlo simulation, it is also possible to compute the neutrons rate on one liquid scintillator detector of the neutron spectrometer per single nA of  $^7\text{Li}$  beam current (1 nA means about  $2.08 \times 10^9$  pps) in case of triple-coincidences.

Giving the elastic scattering cross section of the n+Ar interaction (about 0.7 b/sr [62]), the expected neutrons rate on one neutron detector per single nA of  $^7\text{Li}$  beam current is about  $1.8 \times 10^{-3}$  Hz, that, considering the TPC and the LScis detection efficiencies (about 20% and about 30% for TPC and liquid scintillator, respectively) corresponds to a triple-coincidence rate of about 6 cph (counts per hour), or about 155 cpd (counts per day).

# Chapter 4

## Characterization and Optimization of the TPC

The Time Projection Chamber (TPC) used in ReD (see par. 3.3.3) was tested for the first time during Spring 2018 at Università degli Studi di Napoli Federico II, in collaboration with INFN - Sezione di Napoli. Several tests were performed since then, also with the beam in Catania (see following chapters). In this chapter, an overview of the results obtained in the final configuration only will be presented.

In order to measure the response of the TPC to the argon scintillation light (S1), energy calibrations with gamma sources were taken. Table 4.1 summarizes the sources used in the following analysis.  $^{241}\text{Am}$ , in particular,  $\alpha$ -decays ( $T_{1/2} = 432.6$  y) producing gamma rays of 59.54 keV with 35.9% intensity, and  $^{237}\text{Np}$  as daughter nucleus [63].  $^{133}\text{Ba}$  undergoes isomeric tran-

Source	Activity (kBq)	$\gamma$ peak (keV)	Intensity (%)	Compton edge (keV)
$^{83m}\text{Kr}$	0.015	9.41	5.5	-
		32.15	0.062	-
$^{133}\text{Ba}$	23.4	80.99	32.9	-
		302.85	18.34	164.27
		356.01	62.05	207.26
$^{241}\text{Am}$	36.1	59.54	35.9	-

Table 4.1: Sources used to calibrate the energy response of the TPC: it reports the used gamma sources, the activities, the intensity of the gamma lines and the Compton edges if relevant.

---

sition (IT) with  $T_{1/2} = 10.511$  y, producing  $^{133m}\text{Ba}^1$  [63]. Both these sources were placed externally of the dewar, being the emission lines capable to pass through its walls and interact in the active region of the TPC.

The acquired data sets also include background and laser runs. Estimations of the SiPMs gains by laser runs, in fact, were used to convert charge spectra in number of photoelectrons (PE), so by fitting the gamma peaks of every calibration sources the light yield of the TPC can be extracted and an evaluation of the S1 performances can be done (see par. 4.1).

The TPC was operated in both single and double phase modes and two sets of data with different values of electric drift fields were also collected. The latter, in order to characterize the quenching effect due to the different fields (see par. 4.2 and par. 4.3). An average of about 100k events for each run, 200k in the case of  $^{83m}\text{Kr}$ , were acquired: all waveforms from all SiPMs channels were also stored. A 20  $\mu\text{s}$  long window, with a 6  $\mu\text{s}$  pre-trigger in the case of single phase runs, and a 100  $\mu\text{s}$  long window, with a 10  $\mu\text{s}$  pre-trigger in the case of double phase, were then integrated in the reconstruction software in order to produce the energy spectra (see par. 3.3.6). During all the data taking campaigns, the  $V_{bias}$  of the SiPMs was always kept constant ( $V_{top} = 34$  V,  $V_{bottom} = 68$  V, with  $V_{ov} = +7$  V).

### The $^{83m}\text{Kr}$ source

$^{83m}\text{Kr}$  is the daughter nucleus that comes from the electron capture decay of  $^{83}\text{Rb}$  ( $T_{1/2} = 86.2$  d).  $^{83m}\text{Kr}$  shows a cascade of two emission lines at 32.15 keV ( $T_{1/2} = 1.83$  h) and at 9.41 keV ( $T_{1/2} = 154.4$  ns), producing an emission of electrons totaling about 41.56 keV energy [63].

Usually this source is made by evaporating  $^{83}\text{Rb}$  on carbon coal grains that are then sealed for the integration in the experimental setup. Figure 4.1 shows the mechanical component containing the  $^{83m}\text{Kr}$  source before the installation in the recirculation loop of ReD (see fig. 3.13). So, by opening the proper valve, the  $^{83m}\text{Kr}$  is completely dissolved within the liquid argon inside the active volume of the TPC in about 24 hours.

For the purposes of ReD, a 1.5 kBq  $^{83m}\text{Kr}$  (estimated on 11th September 2018) has been used in order to check the uniformity response of the TPC.

---

<sup>1</sup>Isomeric Transition (IT) is a decay of a nucleus to a lower-energy nuclear state. The process is similar to gamma emission from an excited nuclear state, but differs from it by involving meta-stable states or longer half-lives nuclear states.  $^{133}\text{Ba}$ , in particular, undergoes isomeric transition with 99.99% probability into  $^{133m}\text{Ba}$  that 0.0096% times produces  $^{133}\text{Cs}$  [63].



Figure 4.1: Photo of the  $^{83}\text{Rb}$  trap deployed in the recirculation loop of ReD used for the calibration measurements with the  $^{83\text{m}}\text{Kr}$   $\gamma$ -rays source.

## 4.1 Single Electron Response of SiPM

The silicon photomultiplier detectors (SiPMs) used in ReD can be calibrated in order to obtain a normalization factor that allows a conversion from charge to energy, expressed in terms of photoelectrons (PE) produced per single hitting photon. This can be done by studying the so-called Single Electron Response (SER) spectrum, i.e. by integrating the charge of each detected pulse to form a charge spectrum in which every peak is given by one or multiple photoelectrons. In the photoelectron spectrum or SER, the distance between two adjacent peaks is constant and it can be used for the calculation of the gain, that corresponds to the charge released by a single SPAD.

The SER in ReD is studied with a Hamamatsu PLP-10 pulsed diode laser, externally triggered at 100 Hz, with a wavelength of 403 nm and 50 ps long pulses emissions, using a bunch of optical fibers that reach the inner volume of the TPC. The DAQ is controlled by the same external trigger signal. After the subtraction of the average baseline from the sampled waveform, charge is integrated along a fixed gate of 4  $\mu\text{s}$ , which extends from -600 ns to +3400 ns with respect to the trigger position from the DAQ. Similarly, the amplitude is taken as the maximum of the baseline-subtracted waveform along the same 4  $\mu\text{s}$  interval above.

The output spectra are fitted channel by channel with a sum of Gaussian distributions; the value of each peak is then fitted by using a linear function and the SER parameter is finally extrapolated (see fig. 4.4 and fig. 4.5). This is used within the reconstruction algorithm for the subsequent energy calibration of the detector with gamma sources. Examples of the single electron response measured in ReD are shown in figures 4.2, 4.3, 4.6 and

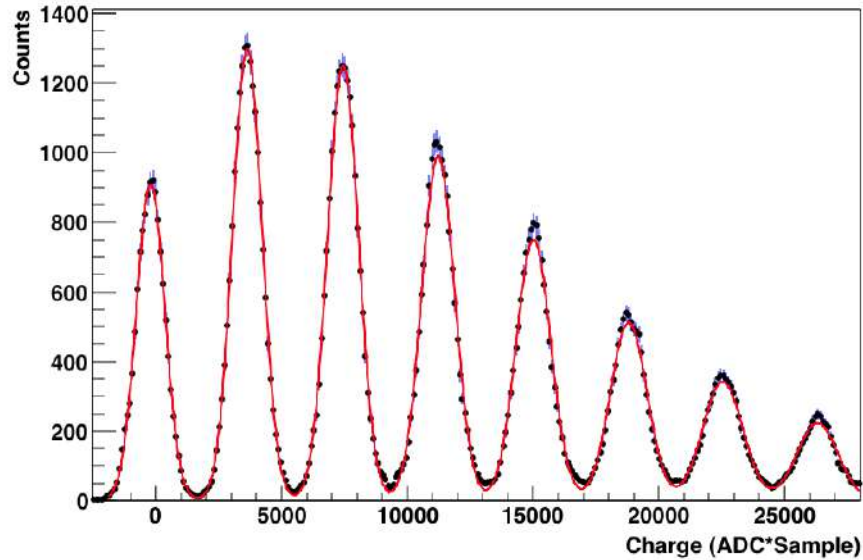


Figure 4.2: Measured charge spectrum from a bottom tile channel. Using the procedure described in the text, the spectrum is then fitted to extract the corresponding Single Electron Response (SER) value.

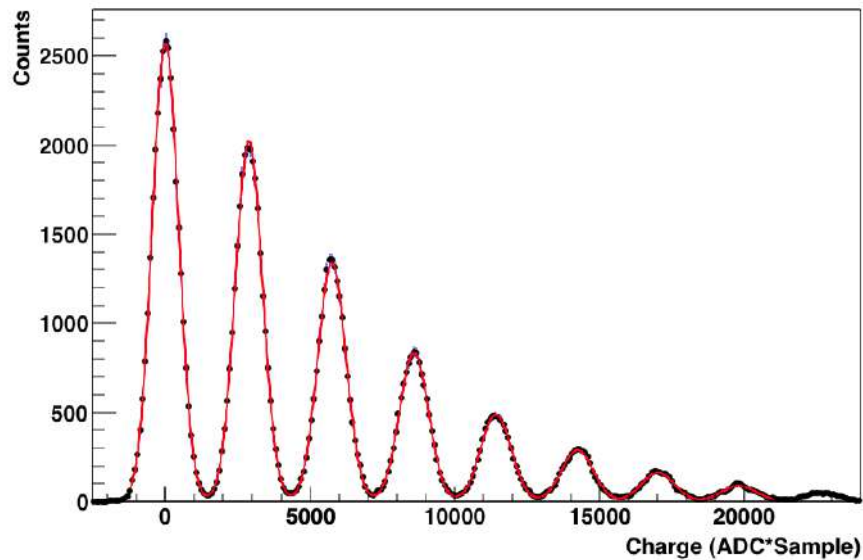


Figure 4.3: Measured charge spectrum from a top tile channel. Using the procedure described in the text, the spectrum is then fitted to extract the corresponding Single Electron Response (SER) value.

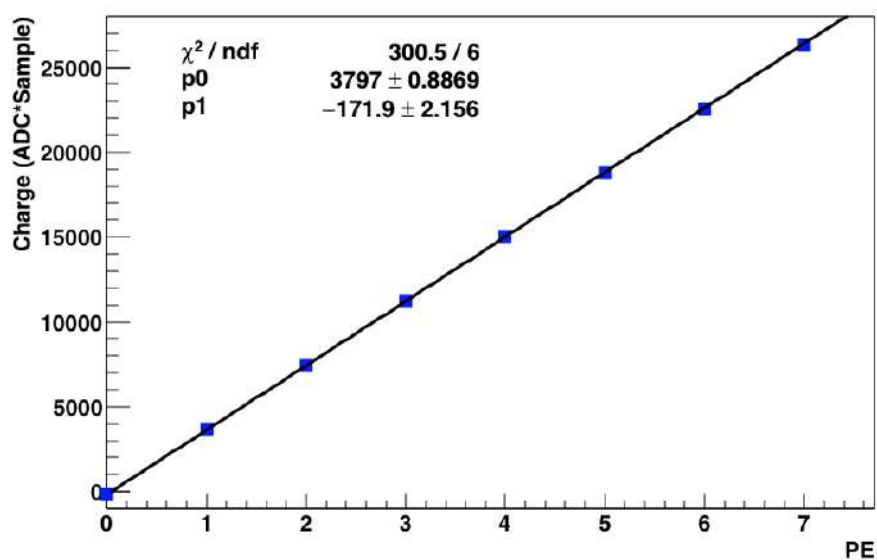


Figure 4.4: SER calibration function from a bottom tile channel. As described in the text, after the fit of the single electron response curve, the mean value of each peak is linearly fitted in order to extrapolate the calibration SER value. The noise pedestal systematically shows a negative charge ( $\sim -0.05$  PE), which is likely due to correlated low-frequency noise between the individual SiPMs.

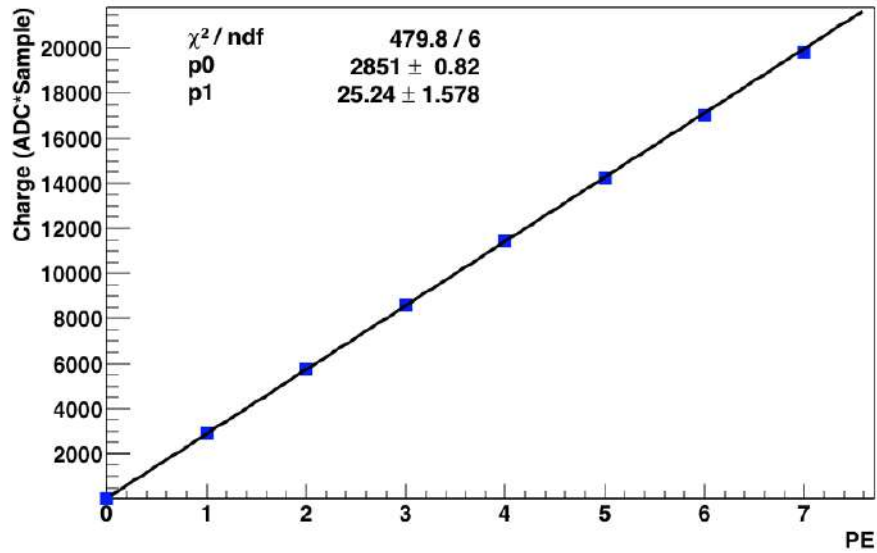


Figure 4.5: The same as the fig. 4.4, but from a top tile channel.

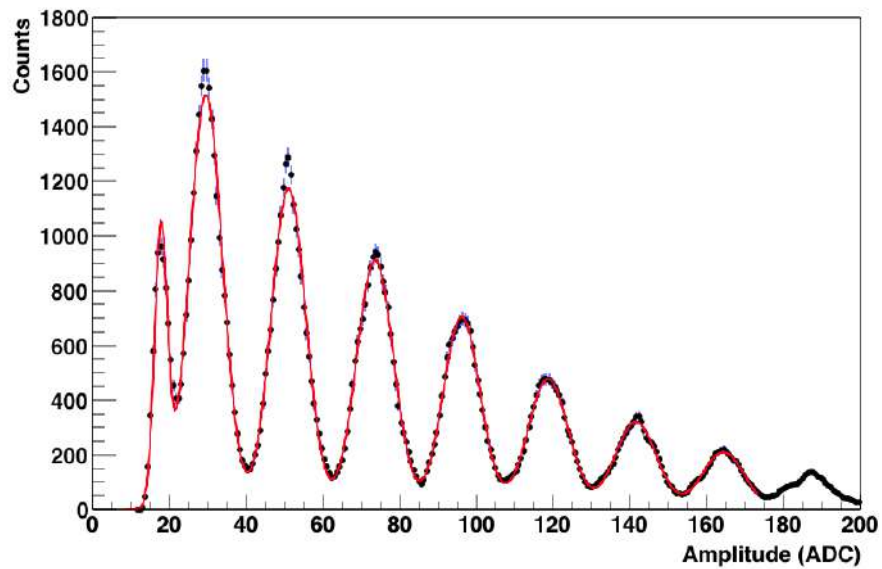


Figure 4.6: SER spectrum from a bottom tile channel expressed in terms of pulse amplitude.

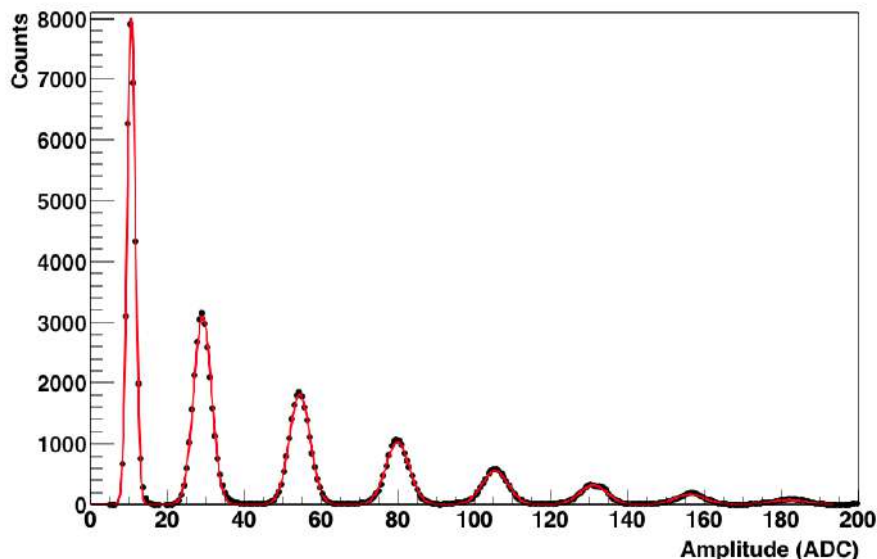


Figure 4.7: SER spectrum from a top tile channel expressed in terms of pulse amplitude.

4.7 for bottom and top tile channels respectively, together with an example of the same response expressed in terms of amplitude. The noise pedestal is centered around zero in charge<sup>2</sup>, as noise is averaged out along the  $4 \mu\text{s}$  integration gate, but has a non-zero value in amplitude, which is related to the noise fluctuations. The typical charge of the single photoelectron in the standard conditions for the used bias voltage is about  $3400 \text{ ADC} \cdot \text{Sample}$  for the bottom channels and about  $2500 \text{ ADC} \cdot \text{Sample}$  for the top channels. Laser runs were also continuously taken for monitoring purposes, showing a stable behavior of the SiPMs over the whole data taking period. Once the values of the bias voltage is fixed to  $34 \text{ V}$  and  $68 \text{ V}$  for the top and bottom tiles, respectively, the values of the SERs are stable within less than  $1\%$  in charge (less than  $0.5\%$  in the best cases). A few channels showed in the past variations up to  $5\text{-}10\%$  between consecutive calibrations.

In Digital Signal Processing (DSP), finally, it is a common procedure to apply a software matched filter to the digitized waveforms in order to clean the signals from noise and to have a better outcome in terms of signal-to-noise ratio. The application of the filtering algorithm for the SER spectrum

<sup>2</sup>In the case of the bottom tile, the noise pedestal systematically shows a negative charge ( $\sim -0.05 \text{ PE}$ ) which is likely due to correlated low-frequency noise between the individual SiPMs.

is described in appendix A.

### The Vinogradov model

The silicon photomultipliers used in ReD work in the so-called Geiger mode avalanche breakdown. As already seen (par. 3.3.4), in this kind of detectors high gain and very low noise, during the avalanche multiplication, offers the possibility to detect single photons. On the other hand, however, this implies also that afterpulsing and cross-talk processes distort the shape of the output signals arising an excess of noise. Referring to [64] for more details, this means that there is, on average, more than one photoelectron eventually detected per each primary single-photoelectron emission. In this condition, the probability distribution for the number of detected photoelectrons  $N_{ph}$  is not a Poisson distribution, due to the correlated production of secondary photoelectrons<sup>3</sup>. The resulting amplitude distribution can be described from the Vinogradov model [64] which employs a compound Poisson distribution. In the Vinogradov model, this results in the definition of a so-called coefficient of duplication ( $K_{dup}$ ):

$$K_{dup} = \frac{p}{1-p} \quad (4.1)$$

where  $p$  represents the cross-talks probability (i.e. the probability that a photon will trigger a secondary avalanche in a neighboring SiPM cell, see par. 3.3.4). The value  $(1+K_{dup})$  represents the number of detected photoelectrons per one real one, or one primary event. The mean ( $EX$ ) and the variance ( $Var(X)$ ) of the compound Poisson distribution are:

$$\begin{aligned} EX &= L \cdot (1 + K_{dup}) \\ Var(X) &= EX \cdot (1 + 2K_{dup}) \end{aligned} \quad (4.2)$$

where  $L$  is the mean of the Poisson distribution, while the term  $1+2K_{dup}$  is the so-called Fano factor<sup>4</sup> and represents the deviation from the pure Poisson distribution [64]. The ideal case (and so the Poisson distribution) is

<sup>3</sup>Due to the presence of correlated noise and delayed pulses in the multiplication region of SiPMs, the probability to detect “fake” events is higher than in the ideal case.

<sup>4</sup>The Fano factor is defined as the ratio between the variance of the experimental Poisson distribution and its theoretical value [65], or alternatively:

$$F = \frac{\sigma^2}{\mu} \quad (4.3)$$

with  $\sigma^2$  and  $\mu$  the variance and the mean of the Poisson distribution, respectively.

restored for  $p = 0$ , which yields  $K_{dup} = 0$  and  $EX = \text{Var}(X) = L$ .

In ReD, the Vinogradov model is applied by fitting the above defined SER amplitude spectrum with a logarithmic likelihood function in order to extract the probability term  $p$  for the calculation of the coefficient of duplication (eq. 4.1) and the Fano factor (eq. 4.2). The typical values obtained for the  $K_{dup}$  ( $p$ ) are 0.36 (26%) and 0.33 (25%) for the bottom and top channels, respectively. The values of  $K_{dup}$  are stable within 2% between subsequent calibrations.

In general the light output response of SiPMs, the so-called Light Yield (LY), is the average number of the photoelectrons detected per unit of deposited energy, and it is mathematically defined as:

$$LY = \frac{\mu}{E} \quad (4.4)$$

where  $\mu$  is the mean value of the deposited energy expressed in units of photoelectrons (PE), and  $E$  its expected value expressed in multiples of electron-Volts (eV). Following, then, the same arguments as above, and by using the Vinogradov model, it is also possible to have an estimate of the LY, corrected for the correlated noise of the SiPMs:

$$LY_{corr} = \frac{LY}{1 + K_{dup}} \quad (4.5)$$

with  $LY_{corr}$  the corrected LY.

### Resolution model

The resolution of a Poisson distribution is given by:

$$\text{Res} = \frac{\sigma}{N_{PE}} = \frac{1}{\sqrt{N_{PE}}} \quad (4.6)$$

where  $N_{PE}$  is the number of photoelectrons detected by the SiPMs and  $\sqrt{N_{PE}}$  is the root-mean-square of the Poisson distribution. In the above model used to fit the S1 distribution, however, sigma ( $\sigma_{exp}$ ) is enlarged, as the root-mean-square of the Fano factor and the number of photoelectrons (see eq. 4.2):

$$\sigma_{exp} = \sqrt{N_{PE} \times F} \quad (4.7)$$

and so the experimental resolution is:

$$\text{Res}_{exp} = \frac{\sigma_{exp}}{N_{PE}} = \frac{\sqrt{F}}{\sqrt{N_{PE}}}, \quad (4.8)$$

i.e. the experimental resolution is degraded by the  $\sqrt{F}$  with respect to pure Poisson distribution.

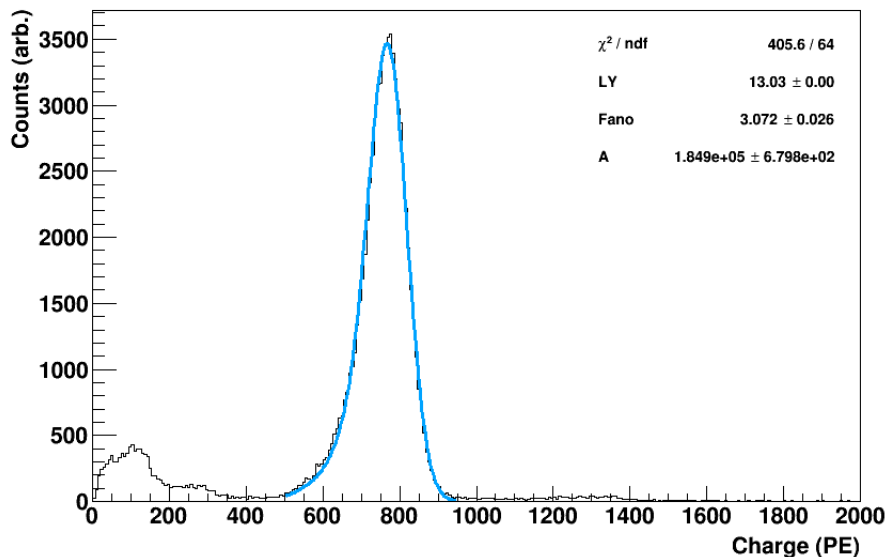


Figure 4.8: S1 light yield calibration spectrum with  $^{241}\text{Am}$  source from run 1137 taken in single phase at null fields. The peak is fitted with a simulated energy deposits of  $^{241}\text{Am}$   $\gamma$ -rays in LAr convolved with an output response function (light blue line).

## 4.2 S1 studies and quenching factor

In figure 4.8, an example of  $^{241}\text{Am}$  spectrum is shown. Compton scattering is unlikely and gamma interactions with LAr is fully dominated by the photoelectric absorption. The resulting 59.54 keV  $\gamma$ -ray peak is then fitted by using a simulated energy deposit of the  $^{241}\text{Am}$   $\gamma$ s in LAr convolved with a Gaussian response function. The latter is generated by a Monte Carlo simulation in order to take into account events in the tails of the distribution, in particular events with energy smaller than 59.54 keV.

All the spectra presented in this analysis were produced using the following conditions:

- requiring that the prompt signal is fully contained in a gate window, or a cluster<sup>5</sup>, of about 12  $\mu\text{s}$  (see par. 3.3.6);

<sup>5</sup>In the reconstruction, the algorithm scans the waveforms looking for a signal below a defined threshold. If this happens, it opens a so-called cluster, i.e. a gate window that contains the entire signal. When the signal comes up again over the threshold limit, the algorithm closes the cluster searching for the next ones. In a typical double-phase run, the time difference between an S1-like and an S2-like cluster is defined as the electrons

- avoiding pile-up events on the same cluster;
- requiring an S1-like signal by means of the pulse shape discrimination parameter (see the definition on par. 4.2.2), and
- select on the  $^{241}\text{Am}$  peak events only, to avoid pile-up or accidental events in the analysis.

### Top/Bottom Asymmetry

Due to the geometry of the ReD TPC, photons are distributed on top and on bottom tiles depending on the position of the scintillation event along the  $z$ -axis (the vertical one). This creates a specific S1 light yield position dependence that can be measured with the  $\gamma$  calibration sources, such as  $^{241}\text{Am}$  and  $^{83\text{m}}\text{Kr}$ . Furthermore, since the ReD TPC is a dual-phase detector in which there is a mesh along the interface between the gas and the liquid argon (see par. 3.3.3), there is an intrinsic asymmetry in the light collection. Due to the presence of the mesh and except for events that occur very close to the top tile, typically the bottom tile receives more light than the top one because of the non-perfect transparency of the mesh and the reflections at the liquid-gas interface. So, for the S1 analysis reported here, and for the following S1 quenching factor determination, a correction for the aforementioned light collection asymmetry was applied to the data set.

The Top/Bottom Asymmetry (TBA) is defined as the difference between the light collected in the top and in the bottom tiles with respect to the total:

$$\text{TBA} = \frac{\text{charge}_{\text{top}} - \text{charge}_{\text{bottom}}}{\text{charge}_{\text{total}}} \quad (4.9)$$

where  $\text{charge}_{\text{top}}$ ,  $\text{charge}_{\text{bottom}}$  and  $\text{charge}_{\text{total}}$  are the charge collected at the top tile, at the bottom one and the sum of them, respectively.

An example of the distribution of S1 charge versus the TBA for a run taken at nominal 200 V/cm drift field configuration is shown in the upper panel of fig. 4.9. From the spectrum, a second order polynomial fit function,  $f(\text{tba})$ , was used to fit the data for each drift field configuration. The same function was then used to evaluate the TBA along the detector on an event per event basis. Then, a correction to the S1 spectrum was applied as the ratio between the fit function evaluate along the detector, and the one calculated at the value of the TBA corresponding to the mean height of the TPC  $f(t_0)$  (about -0.15). The lower panel of the same figure 4.9 reports the application of TBA correction. From the spectrum is evident that the effect of such a

---

drift time.

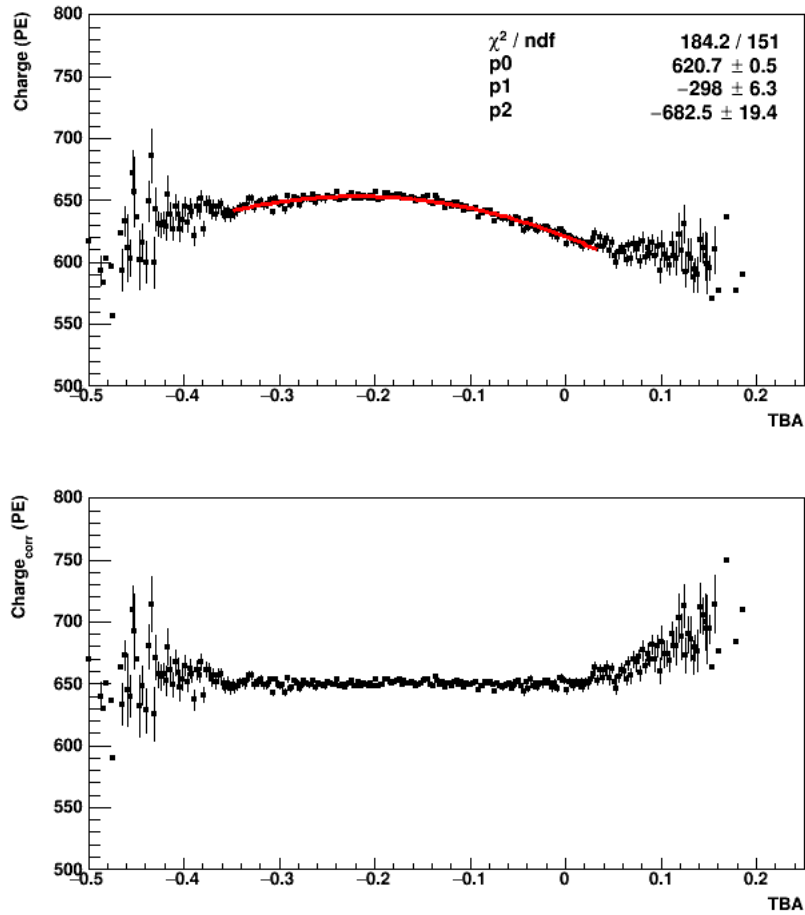


Figure 4.9: Comparison between S1 pulse integral distributions versus TBA before (upper panel) and after (lower panel) the applied corrections, from a 200 V/cm drift field  $^{241}\text{Am}$  run. The effects of the correction (also visible from the spectrum) imply an uniform events distribution between the bottom and top SiPM tiles.

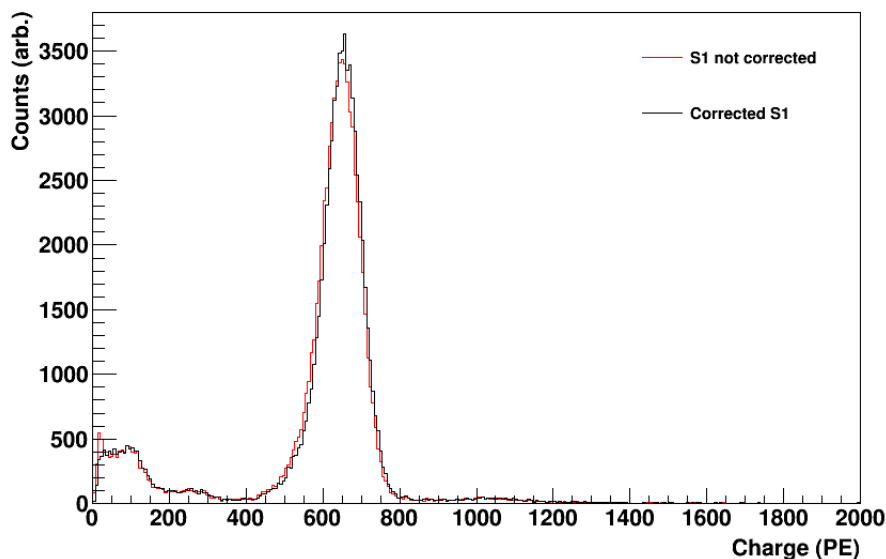


Figure 4.10: Comparison between  $^{241}\text{Am}$  calibration peaks taken at 200 V/cm drift field, before (red line) and after (black line) the application of TBA corrections. TBA corrections, in fact, improves the peak resolution from about 6.9% to about 6.6%.

correction implies the assumption that both the bottom and the top SiPMs tiles detect the same amount of light (charge).

Figure 4.10 shows the effect of the above TBA correction on the resolution of the same  $^{241}\text{Am}$  peak taken at 200 V/cm drift field, before (red line) and after (black line) the application of the corrections. In this case the resolution,  $\sigma/\mu$ , improves from about 6.9% to about 6.6% without and with the corrections, respectively.

After the correction for the TBA, S1 spectra are then fitted with the simulated energy distributions with the LY as the only free parameter.

### 4.2.1 S1 Light Yield determination

Figure 4.11 shows the gamma peak of  $^{241}\text{Am}$  taken with a nominal electric drift field value of 200 V/cm, set by a proper tuning of the voltages of the electrodes of the TPC. The anode in particular was kept at a voltage of +200 V, while the cathode and the first ring at a voltage of -1000 V and -100 V, respectively. A shift to lower values of the charge (about 100 PE) of the  $^{241}\text{Am}$  gamma peak is evident from the fig. 4.12, where two runs taken at 0 V/cm (black line) and 200 V/cm (red line), respectively, are re-

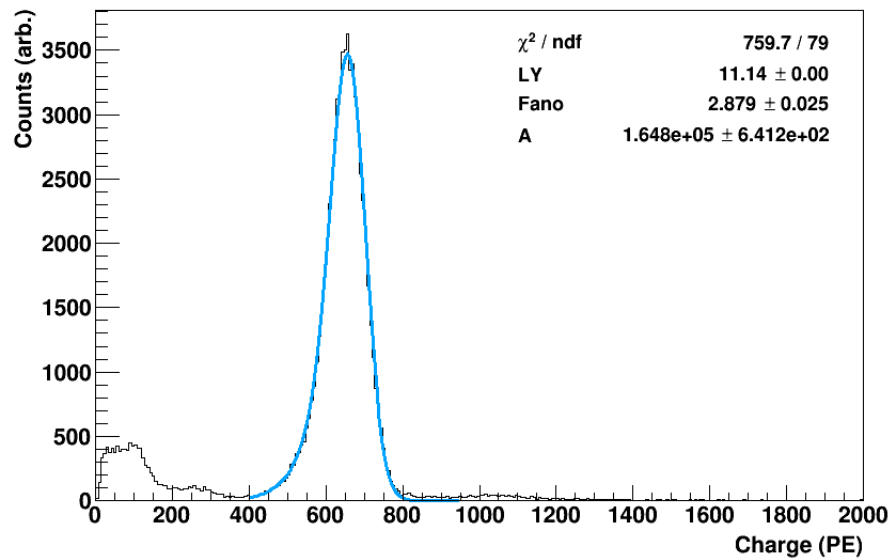


Figure 4.11: S1 light yield calibration spectrum with  $^{241}\text{Am}$  source from run 1145 taken in single phase with 200 V/cm electric drift field value. The peak, in this case, is shifted to lower charge values (about 100 PE) with respect to the same gamma peak but taken at null fields. The light blue line, is the fit to the peak by using the fit function described in the text.

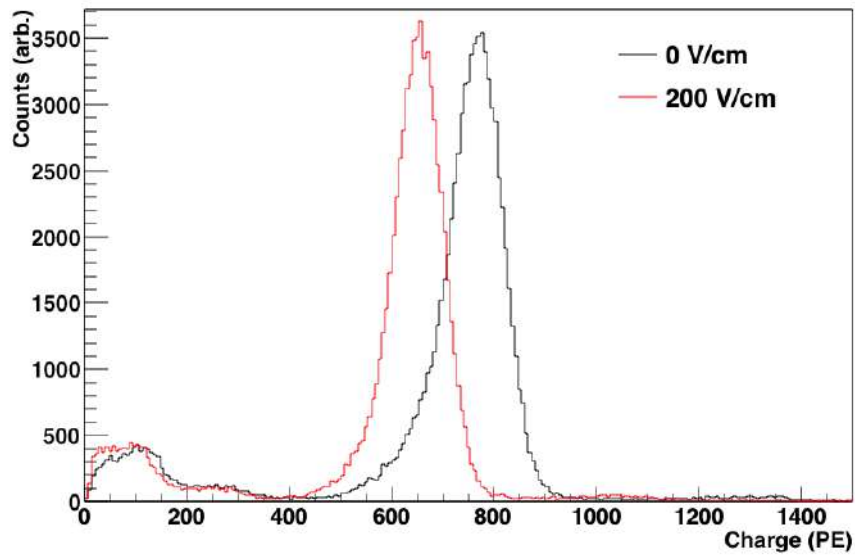


Figure 4.12: Comparison between  $^{241}\text{Am}$  peaks taken at 0 V/cm and at 200 V/cm electric drift field values, respectively. The peak at 200 V/cm (red line) is shifted to lower charge values (about 100 PE) with respect to the same gamma peak but taken at null fields (black line) because of the quenching effect, as reported in par. 4.2.3.

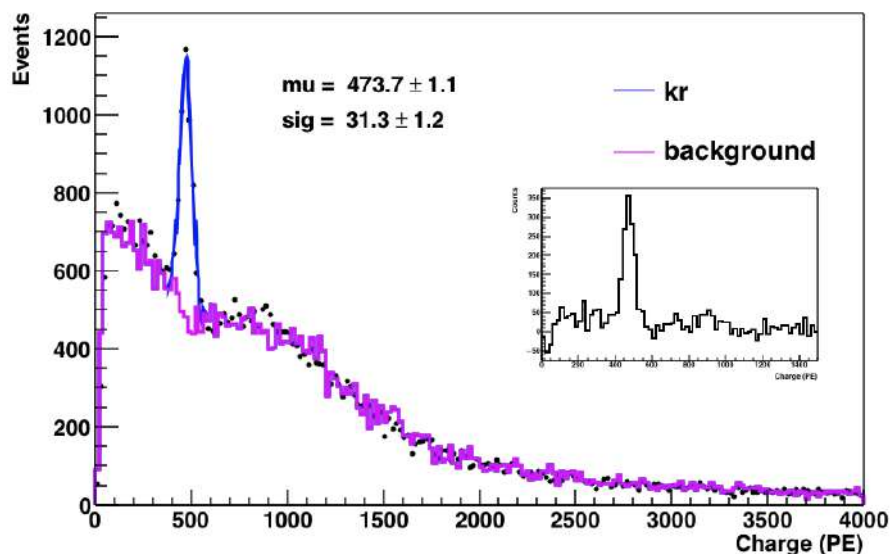


Figure 4.13: S1 light yield calibration spectrum with  $^{83m}\text{Kr}$  source from a run taken at 200 V/cm fields configuration. The fit is performed by using a RooFit algorithm (blue line), and shows an overlaying with the corresponding background spectrum (violet line). The inset shows the spectrum after the background subtraction.

ported. This is mainly due to the presence of the electric field that inhibits the recombination of the electron-ion pairs due to the primary scintillation process, reducing the total light output (see the following par. 4.2.3).

Following the analytical procedure described so far, from the fit, the measured LY is 11.144(4) PE/keV that correspond to a  $\text{LY}_{\text{corr}}$  of 8.358(4) PE/keV if one takes into account the correlated noise of the optical readout devices, as mentioned in par. 4.1. Furthermore, the measured resolution ( $\sigma/\mu$ ) is about 6.6%.

Further calibration spectra, obtained from  $^{83m}\text{Kr}$  and  $^{133}\text{Ba}$ , are shown in figures 4.13 and 4.14, respectively. Both spectra are fitted by using a RooFit algorithm, and are shown together with a corresponding background superimposed (violet lines). The insets represent the source spectra after the statistical background subtractions. They confirmed the LY value at 200 V/cm drift field computed from the americium runs, while the barium data were also used in the calculation of the following electric field quenching parameter (see par. 4.2.3).

Results are summarized in table 4.2: it reports the light yield values from the S1 fit spectra corrected for the TBA dependance (LY column), together with the ones from the cross-talks and afterpulsing probabilities corrections

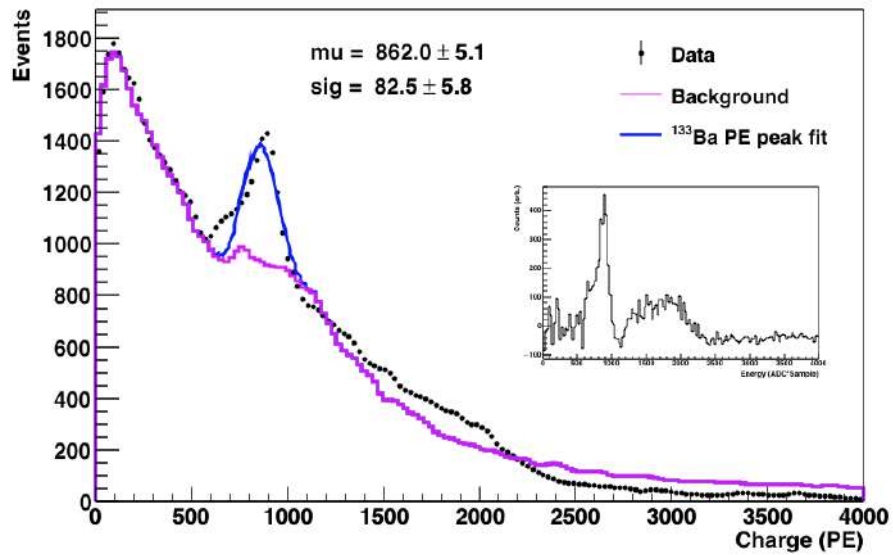


Figure 4.14: S1 light yield calibration spectrum with  $^{133}\text{Ba}$  source from a run taken at 200 V/cm fields configuration. The fit is performed by using a RooFit algorithm (blue line), and shows an overlaying with the corresponding background spectrum (violet line). The inset shows the spectrum with a background subtraction.

Run no.	Source	$E_d$ (V/cm)	LY (PE/keV)	$LY_{corr}$ (PE/keV)	Res. (%)
1137	$^{241}\text{Am}$	0	13.026(4)	9.794(4)	6.3
1141	$^{241}\text{Am}$	50	12.346(4)	9.263(4)	6.2
1144	$^{241}\text{Am}$	100	11.901(3)	8.929(3)	6.3
1145	$^{241}\text{Am}$	200	11.144(4)	8.358(4)	6.6
1148	$^{241}\text{Am}$	300	10.557(4)	7.918(4)	6.9
1151	$^{241}\text{Am}$	400	10.065(3)	7.549(3)	7.3
1152	$^{241}\text{Am}$	500	9.642(4)	7.232(4)	7.6
1155	$^{241}\text{Am}$	700	8.933(3)	6.701(3)	8.3
1156	$^{241}\text{Am}$	1000	7.970(3)	5.978(3)	10.2
1065	$^{83m}\text{Kr}$	200	11.41(1)	8.48(1)	15.5
1168	$^{133}\text{Ba}$	200	10.64(2)	7.91(2)	9.6

Table 4.2: Light Yields from single phase runs used for the following electric field quenching studies. Numbers are extracted from the S1 fit spectra (LY column) and corrected for the cross-talks and afterpulsing probabilities ( $LY_{corr}$  column) and for TBA dependence. The reported errors are from fit only. Refer to text for more details.

( $LY_{corr}$  column). From the above table, comparing the two extreme values of corrected light yields at null fields and at 1000 V/cm, a variation of about 40% is achieved. This is mainly due to the presence of the electric drift field that introduces a quenching: higher values of electric fields reduce the electron-ion recombination in liquid argon, and this implies a reduction of the prompt scintillation signal S1.

### 4.2.2 Pulse shape discrimination

The Pulse Shape Discrimination (PSD) performance of the ReD TPC was evaluated using an AmBe neutron source, comparing the data with a simple model in order to optimize the value of the PSD parameter needed to distinguish between NRs and ERs. From the analysis of the raw waveforms acquired with this source, an average recovery time of about  $0.5 \mu\text{s}$  for the SPADs was found, comparable with the argon triplet decay time constant ( $\tau_t = 1.5 \mu\text{s}$ , see par. 2.1). Since this is related with the formation of the prompt signal, from the NRs data one can define the best value of the pulse shape discrimination parameter ( $f_{prompt}$ ) as the fraction of prompt signal occurring in the first 700 ns:

$$f_{prompt} = \frac{\int_0^{700\text{ns}} S1 dt}{\int_0^t S1 dt}, \quad (4.10)$$

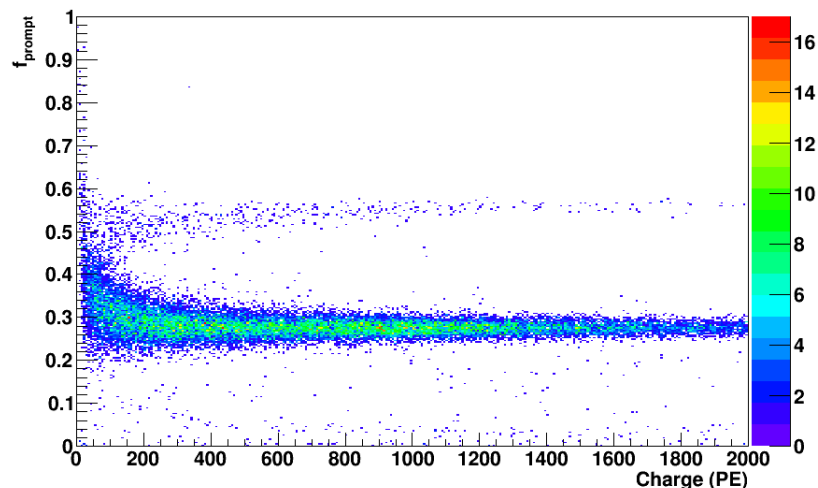


Figure 4.15: Scatter plot of  $f_{prompt}$  distribution versus S1 from AmBe calibration run taken at 200 V/cm drift field configuration and with a 5.79 kV/cm multiplication field. The  $f_{prompt}$  allows to distinguish between NRs and ERs as mentioned in the text.

where the time interval for the complete formation of the signal starts from 0 and ends at  $t$ . Figure 4.15 shows a scatter plot of  $f_{prompt}$  over the pulse integral S1 taken from an AmBe run with nominal fields configuration. From the spectrum it is possible to distinguish between nuclear and electron recoils,  $0.45 < f_{prompt} < 0.6$  and  $0.2 < f_{prompt} < 0.4$ , respectively. The spectrum is obtained requiring the presence of two clusters and avoiding multiple-scatter or pile-up events.

The same PSD calibration analysis was also performed by using a portable neutron gun, i.e. a commercially available API-120 Deuteron - Deuteron generator. This system is capable to provides neutrons at very high intensity (about  $10^4$  n/s at  $4\pi$  steradians) and isotropically distributed with a quasi-monoenergetic kinetic energy. The generator produces, in fact, neutrons of about 2.5 MeV, by means of  $d(d,n)^3\text{He}$  reaction, that release in liquid argon about 250 keV kinetic energy at maximum. During the performed tests, then, the neutron gun was installed very close to the ReD system in order to increase the probability to have neutron interactions with the TPC. A sample spectrum of the  $f_{prompt}$  distribution versus the S1 charge is shown in figure 4.16. The two NRs and ERs bands are clearly separated and a total of about 5000 neutron-like events passed the analysis cuts. The inset shows a 1-D projection of the same  $f_{prompt}$  parameter: here the two classes of events are well distinguished with a little contamination in the region between 0.38

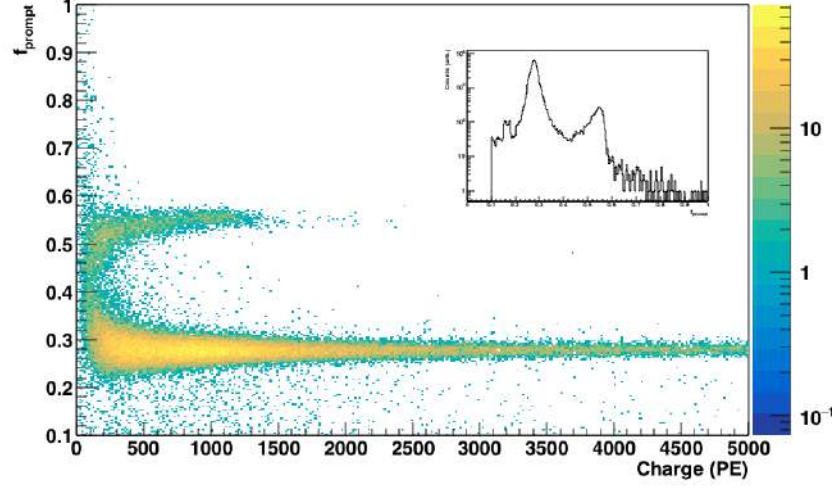


Figure 4.16: Scatter plot of  $f_{prompt}$  distribution versus S1 from  $d(d,n)^3\text{He}$  reaction produced by using a neutron gun, taken at 200 V/cm drift field configuration and with a 5.79 kV/cm multiplication field. The inset shows a projection on the x-axis of the same  $f_{prompt}$  parameter.

and 0.42 due to overlapped events. These events might be reduced with a proper selection on TBA.

### 4.2.3 S1 quenching

In order to fully characterize the S1 response of the ReD TPC at fields configurations other than 0 V/cm, a set of data with electric drift fields ( $E_d$ ) from 50 V/cm up to 1000 V/cm were also collected. The presence of an electric field in the active region of the TPC, in fact, increases the probability that electrons escape the recombination effect. In this case the prompt signal S1 is expected to decrease with the increase of drift electric field, i.e. electric field quenching phenomenon.

If  $N_{ex}$  is the number of excitons and  $N_i$  is the number of electron-ion pairs produced by an ionizing particle in the TPC, the total scintillation signal is generated by the de-excitation of the  $N_{ex}$  excitons and of the secondary excitons,  $R \times N_i$ , that are generated from recombination of the electron-ion pairs with probability  $R$ . If  $\alpha$  is the ratio  $N_{ex}/N_i$ , this be expressed as

$$S1 = g_1(N_{ex} + R \times N_i) = g_1(\alpha + R) \times N_i, \quad (4.11)$$

where  $g_1$  is the total optical efficiency of the TPC (i.e. number of photoelectrons per each scintillation photon emitted in the TPC). The parameter  $g_1$

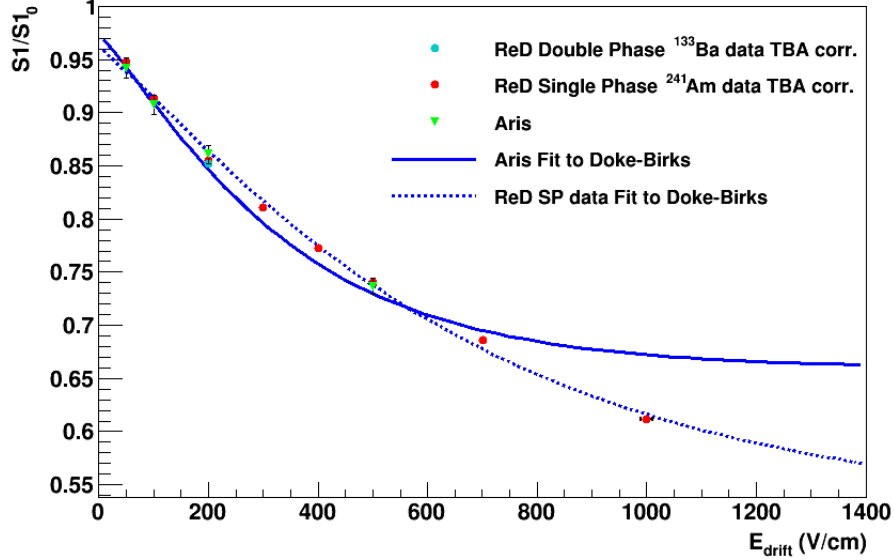


Figure 4.17: Electric field quenching of the S1 prompt signal measured in ReD and extracted using ERs data at different drift field values compared with ARIS data (green triangles) [67], fitted with the Doke-Birks recombination model [66] (dashed blue line). Red points are from  $^{241}\text{Am}$  data while the dark cyan one is from  $^{133}\text{Ba}$  data. The solid blue line is the same model fitting the ARIS data points (see ref. [67] for the details).

is a detector intrinsic property and accounts for the geometrical collection efficiency of the scintillation light, for the wavelength-shifting and for the quantum efficiency of the SiPMs. The typical value of  $\alpha$ , which depends on the ionization density, is 0.21 for electron recoils (ERs) and  $\sim 1$  for nuclear recoils (NRs) [66], while the recombination probability  $R$  is a function of the drift field  $E_d$ .

Following the same arguments reported in [67], the electric field quenching can be studied by looking at the distribution of the ratio between the S1 signal taken at a proper value of  $E_d$  and the S1 taken at null fields ( $S1/S1_0$ ), versus the values of the field. In the Doke-Birks model, the recombination probability  $R$  can be parametrized as a function of the stopping power  $dE/dx$  and of the electric field as

$$R = \frac{A \, dE/dx}{1 + B \, dE/dx} + C \quad (4.12)$$

Run no.	Source	$E_d$ (V/cm)	$S1/S1_0$	Res. (%)
1137	$^{241}\text{Am}$	0	1	6.3
1141	$^{241}\text{Am}$	50	0.947(4)	6.2
1144	$^{241}\text{Am}$	100	0.914(4)	6.3
1145	$^{241}\text{Am}$	200	0.855(4)	6.6
1148	$^{241}\text{Am}$	300	0.810(4)	6.9
1151	$^{241}\text{Am}$	400	0.772(3)	7.3
1152	$^{241}\text{Am}$	500	0.740(3)	7.6
1155	$^{241}\text{Am}$	700	0.686(3)	8.3
1156	$^{241}\text{Am}$	1000	0.612(3)	10.2
1168	$^{133}\text{Ba}$	200	0.85(2)	9.6

Table 4.3: Scintillation quenching ( $S1/S1_0$ ) from  $^{241}\text{Am}$  single phase runs and  $^{133}\text{Ba}$  run taken with different values of electric drift field. Numbers are extracted from the procedure described in the text, and the reported errors are statistical only.

with  $B = A/(1 - Ce^{-DE_d})$ , or explicitly

$$R = \frac{A \, dE/dx}{1 + \frac{A}{1 - Ce^{-DE_d}} \, dE/dx} + Ce^{-DE_d}. \quad (4.13)$$

The dependence  $R(E_d)$  can be studied by taking the ratio between the scintillation light at a given  $E_d$ ,  $S1$ , and the ones taken at null fields  $S1_0$ :

$$S1/S1_0 = \frac{\alpha + R(E_d)}{\alpha + R_0}. \quad (4.14)$$

In this work, the ( $S1/S1_0$ ) ratio (fig. 4.17), extracted from the July 2019 calibration campaign (red and dark cyan points), is compared with the ARIS experiment (green triangles) [67] and fitted by using the same Doke-Birks empirical recombination model [66] used in ref. [67] (blue dashed line). Red points, in particular, comes from  $^{241}\text{Am}$  data, while the dark cyan one, at 200 V/cm, correspond to a  $^{133}\text{Ba}$  run. The solid blue line is the fit of ARIS points with a modified version of the Doke-Birks recombination model (see ref. [67] for the details). So, data from ReD can be fitted against the combination of eq. 4.14 with the Doke-Birks model of eq. 4.13. The  $S1/S1_0$  values of  $^{241}\text{Am}$  runs taken in ReD (single phase) with drift field between 0 and 1000 V/cm are summarized in table 4.3, together with the results from one  $^{133}\text{Ba}$  run taken in double phase at 200 V/cm. The ReD data agree very well with the data from ARIS [67], taken with fields up to 500 V/cm. The parameters

	A	C	D
	cm/MeV		cm/V
This work	0.001(8)	0.79(7)	0.00172(1)
ARIS [67]	0.0025(2)	0.77(1)	0.0035(3)

Table 4.4: Fit parameters to the Doke-Birks recombination model [66] used for the calculation of the quenching factor induced by the drift field in ReD. The table also contains the values from ARIS experiment [67], see text for details.

from the fit against the Doke-Birks parametrization of eqs. 4.13 and 4.14 are reported in table 4.4 for ReD and ARIS, respectively. The ARIS fit, which is limited by the last point at 500 V/cm, fails to reproduce the points taken in ReD at 700 and 1000 V/cm. The main difference is in the value of the coefficient  $D$  which drives the exponential electric field dependence. The values of  $D$  derived from ARIS and ReD are anyway consistent within the fit uncertainties.

### 4.3 S2 and charge yield determination

Together with scintillation-only runs in different fields conditions, runs with ionization and scintillation were also acquired running the TPC in the so-called double phase mode. In this case, in order to produce the ionization signal (S2), a fine tuning of the operational parameters of the detector was made. So, in the following, only runs taken in the nominal configuration of extraction and multiplication fields (3.8 kV/cm and 5.79 kV/cm, respectively) will be considered. A scan in drift field was performed by varying the field from 0 V/cm up to 1 kV/cm. The power of bubbler, used for the formation of about 7 mm of gas pocket, was then kept at 1.4 W for all the duration of the data taking phase (see par. 3.3.3).

Table 4.5 summarizes the runs used in the following analysis.

#### 4.3.1 Electrons drift time and lifetime

The electron drift time ( $\tau_{drift}$ ) is defined as the difference between the start time of the prompt scintillation signal S1 and the ionization one S2. It allows for a precise z-position determination of the events. On figure 4.18 an electron drift time distribution spectrum is presented from an  $^{241}\text{Am}$  run with nominal fields configuration. The distribution presents a cut-off at about 62  $\mu\text{s}$  that, for this run, represents the maximum electron drift time inside the

Run no.	Source	$E_d$ (V/cm)	$E_{ex}$ (kV/cm)	$E_{el}$ (kV/cm)
1159	$^{241}\text{Am}$	0	0	0
1164	$^{241}\text{Am}$	100	3.8	5.79
1135	$^{241}\text{Am}$	200	3.8	5.79
1165	$^{241}\text{Am}$	400	3.8	5.79
1160	$^{241}\text{Am}$	700	3.8	5.79
1161	$^{241}\text{Am}$	1000	3.8	5.79
1191-1193	AmBe	200	3.8	5.79

Table 4.5: Dataset used to calibrate the S2 response of the TPC: it reports the run number, the used source and the fields (drift, extraction and electroluminescence) configurations used for the subsequent analysis.

TPC, i.e. events that occurred very close to the cathode (the bottom of the TPC). The maximum electron drift time ranges from about  $80 \mu\text{s}$  for a drift field of  $100 \text{ V/cm}$  down to about  $24 \mu\text{s}$  for a drift field of  $1\text{kV/cm}$ . Considering the geometry of the detector, the maximum value of the electron drift time at  $200 \text{ V/cm}$  drift field leads to an electron drift velocity<sup>6</sup> of about  $0.8 \text{ mm}/\mu\text{s}$ .

Finally, as it is possible to see from the figure itself, the reconstruction algorithm is not able to resolve between two clusters if they are very close: this is the main reason why the electron drift time spectrum starts from about  $12 \mu\text{s}$  instead of zero, i.e. this is the time difference between the end of the first cluster and the start of the next one. Furthermore, the kind of peak structure showed in the figure is due to the presence of the copper field rings of the TPC that absorb events coming from the interaction of  $^{241}\text{Am}$   $\gamma$ -rays (the valleys between each peak in the spectrum). For comparison purposes, in figure 4.19, the electron drift time distribution from a  $^{83\text{m}}\text{Kr}$  run is shown. The main difference between the two is due to the fact that the  $^{83\text{m}}\text{Kr}$  is dissolved within the liquid argon inside the TPC, so the events are uniformly distributed in the active volume of the detector.

The electrons lifetime ( $\tau$ ) is the time interval required for the drifting electrons to be reduced by a factor  $1/e$ , and it is related to the number of electrons at a given instant  $t$ ,  $N_e(t)$ , by the relation:

$$N_e(t) = N_e(0)e^{-\frac{t}{\tau}} \quad (4.15)$$

<sup>6</sup>The electron drift velocity depends on the value of the electric drift field and on the LAr temperature [68], and in this case it was derived as the ratio between the anode-cathode distance over the electron drift time.

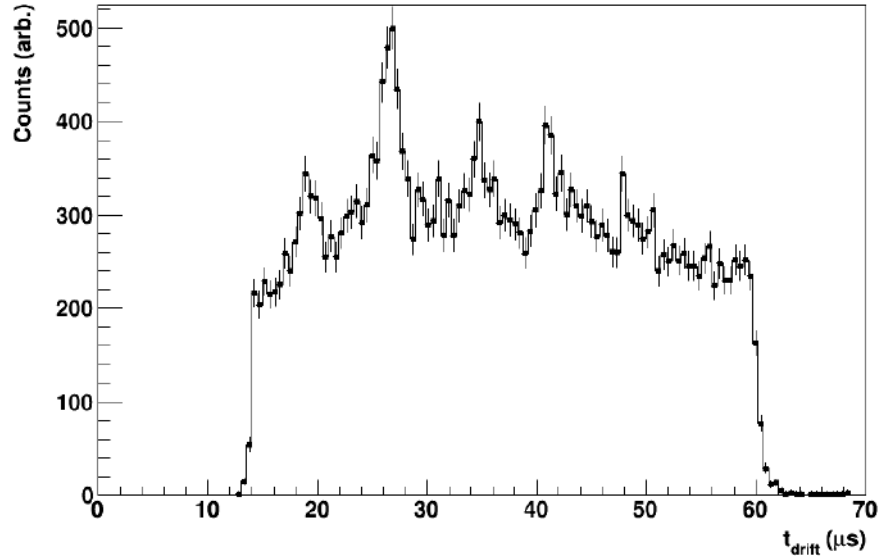


Figure 4.18: Electron drift time distribution calculated as the start time difference between the S1 and S2 signals and expressed in  $\mu\text{s}$  from an  $^{241}\text{Am}$  run with nominal fields configuration.

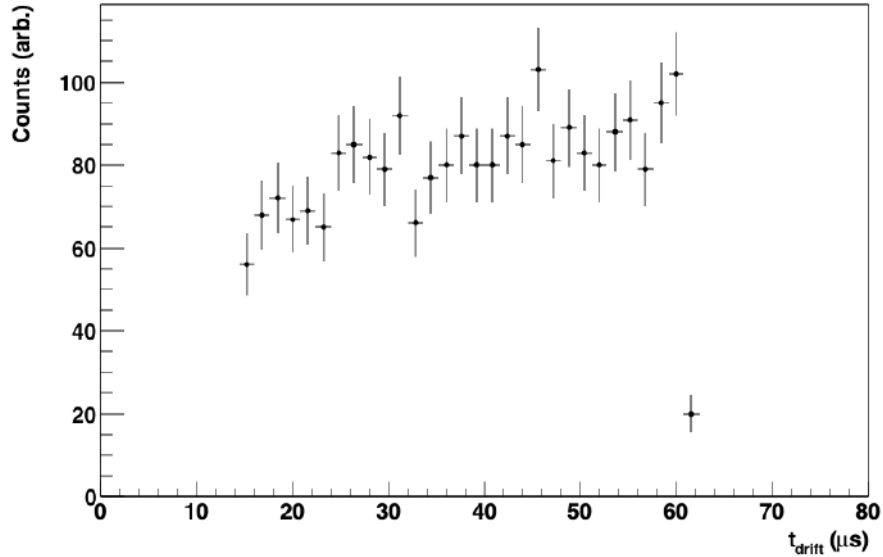


Figure 4.19: The same as the fig. 4.18 but extracted from a  $^{83m}\text{Kr}$  run with nominal fields configuration.

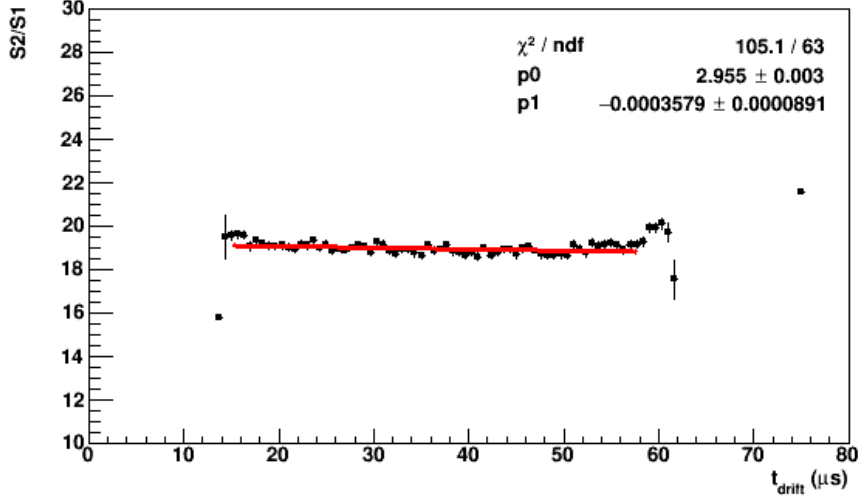


Figure 4.20: Scatter plot of the S2/S1 ratio versus electron drift time used for the electron drift lifetime. The red solid line is the exponential fit to the experimental data.

where  $N_e(0)$  is the number of drifting electrons at a given starting time. The quantity just defined is important in order to quantify the purity of the liquid argon during the regular data taking phase, since the drift electron lifetime is related to the number of impurities dissolved in the LAr. For this purpose, in ReD, there is a liquid and gas recirculation system that prevents the impurities coming from potential leaks in the cryogenic system, or from outgassing from the internal component of the detector (such as cables or other mechanical parts not immersed in LAr), to be dissolved in the active volume of the TPC (see par. 3.3.3).

In ReD, the electrons lifetime is evaluated by measuring the correlation between the S2/S1 ratio versus the drift time distribution in the TPC, fitted with an exponential function according to eq. 4.15. The electron drift lifetime  $\tau$  comes from the inverse of the slope of the fit function. In figure 4.20, a valuation of  $\tau$  from an  $^{241}\text{Am}$  run is shown: with the nominal fields configuration, and after a recirculation period of about one month (the system was cooled down at the beginning of June 2019, while the data set analyzed in this work was taken in the second half of July 2019), the drift electron lifetime is about  $(2.79 \pm 0.01)$  ms (error from the fit). For comparison, on figure 4.21, electron drift lifetime is reported from an  $^{241}\text{Am}$  run taken four days after the cool down of the system. The drift lifetime is about  $(290.9 \pm 3.0)$   $\mu\text{s}$ , an order of magnitude smaller than the previous one. This is mainly

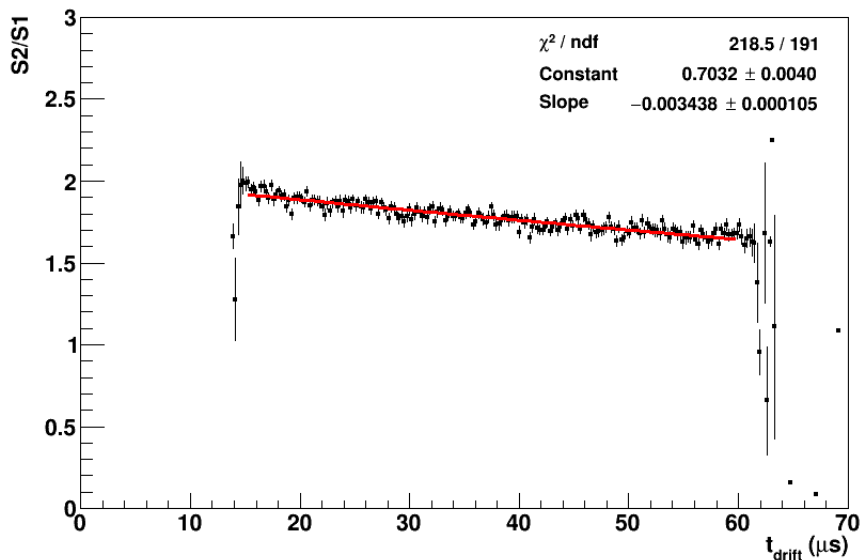


Figure 4.21: Scatter plot of the S2/S1 ratio versus electron drift time as the one reports in fig. 4.20 taken from a very first run after the cooling of the system, shown for comparison purposes.

due to the outgassing of the hot components and to the LAr dissolved impurities.

### 4.3.2 The S1-S2 anti-correlation

Figure 4.22 reports the simultaneous measurements of S1 and S2 yields from  $^{241}\text{Am}$  runs taken with varying electric drift field but with the same multiplication fields as reported on table 4.5. It is evident that a decrease of S1 yield with the drift field is followed by an increase of S2 yield. As already mentioned in par. 4.2.3, for the single phase measurements, the decrease of the S1 yield is due to the presence of the drift field that partially inhibits the electron-ion pairs recombination [69], while the increasing of S2 yield is linked to the higher number of drifting electrons that reach the extraction and then the multiplication region.

In the following, the anti-correlation between S1 and S2 is used to derive the S1 and S2 gains ( $g_1$  and  $g_2$ , respectively) from a set of dual-phase data in the framework of the recombination model. A typical interaction inside a liquified noble gas produces excited atoms and a short track of ionization. Following ionization, electron-ions pairs are produced together with excited diatomic molecules ( $R_2^*$ ) that, after their decay, emit scintillation photons

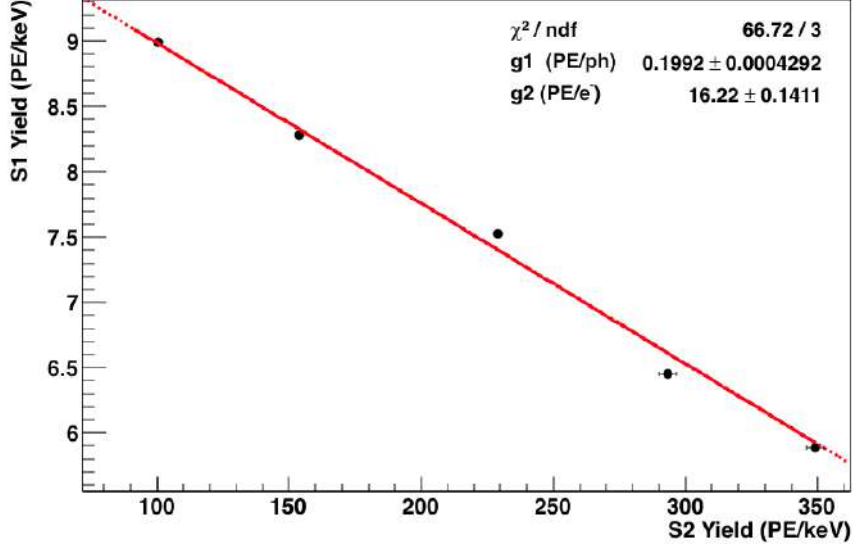


Figure 4.22: S1 yield versus S1 yield from  $^{241}\text{Am}$  runs obtained by varying the drift field from 0 up to 1000 V/cm.

( $R_2^* \rightarrow 2R + h\nu$ ). Referring to ref. [57], developing the equation 4.11, the total number of scintillation photons (S1) is:

$$N_{ph} = \eta_{ex}N_{ex} + \eta_iRN_i \quad (4.16)$$

with  $N_{ex}$  and  $N_i$  the number of excitons and the number of electron-ion pairs, respectively,  $R$  the recombination probability and  $\eta_{ex}$  and  $\eta_i$  the efficiencies of producing scintillation light by direct excitons and recombined ions, respectively. Since, in absence of any photon non-radiative relaxation process,  $\eta_{ex}$  and  $\eta_i$  are expected to be unity, the S1 and S2 yields, and the  $g_1$  and  $g_2$  gains can be derived directly from the following:

$$S1 = g_1N_{ph} \quad (4.17)$$

and

$$S2 = g_2(1 - R)N_i. \quad (4.18)$$

In the above equations S1 and S2 are the scintillation and ionization signals respectively, both corrected for the top/bottom asymmetry and the drift time dependences (following the same method described in sec. 4.2), expressed in terms of PE. In the assumption that  $g_1$  and  $g_2$  are detector properties, in the limit where  $R \rightarrow 1$ , the average energy necessary for the

Run no.	Source	$E_{drift}$ (V/cm)	S1 yield (PE/keV)	S2 yield (PE/keV)
1159	$^{241}\text{Am}$	0	9.649(5)	-
1164	$^{241}\text{Am}$	100	8.994(6)	100.6(2)
1135	$^{241}\text{Am}$	200	8.281(5)	153.9(3)
1165	$^{241}\text{Am}$	400	7.528(7)	229.2(6)
1160	$^{241}\text{Am}$	700	6.450(1)	293.3(15)
1161	$^{241}\text{Am}$	1000	5.890(1)	349.0(16)

Table 4.6: S1 and S2 yields used for the  $g_1$  and  $g_2$  calculation extracted from the S1 and S2 fitted spectra and corrected for the cross-talks and afterpulsing probabilities and for TBA and drift time dependences. The reported errors are from fit only. Refer to text for more details.

production of the single scintillation photon,  $W_{ph}(\text{max})$ , is defined as [66]:

$$W_{ph}(\text{max}) = \frac{E}{N_{ex} + N_i} = \frac{W}{1 + N_{ex}/N_i} = \frac{W}{1 + \alpha}, \quad (4.19)$$

where  $W$  is the so-called W-value, equal to  $23.6 \pm 0.3$  eV in LAr using measurements from  $^{207}\text{Bi}$  [71], and represents the average energy necessary for the production of an electron-ion pair. The anti-correlation between S1 and S2 can, then, be written as:

$$\frac{S1}{E} = \frac{g_1}{W_{ph}(\text{max})} - \frac{g_1}{g_2} \frac{S2}{E} \quad (4.20)$$

where  $E$  is the deposited energy. The parameters  $g_1$  and  $g_2$  are expressed as the number of photoelectrons following the production of one scintillation photon or of one ionization electron, respectively.

In ReD, assuming  $W_{ph}(\text{max})$  to be  $19.5 \pm 1.0$  eV for  $^{241}\text{Am}$  electrons [66], from the fit parameters of fig. 4.22,  $g_1 = (0.1991 \pm 0.0004)$  PE/photon and  $g_2 = (16.22 \pm 0.14)$  PE/e $^-$  were obtained. The S1 gain of ReD can be compared with the values 0.157(1) PE/photon from DarkSide-50 [47] and 0.104(6) PE/photon from SCENE [57], respectively. The higher value of  $g_1$  achieved in ReD is driven by the better quantum efficiency of the SiPMs with respect to photomultipliers. The S2 gain of ReD is slightly worse than DarkSide-50, 23(1) PE/e $^-$  [49], and much higher than SCENE, 3.1(3) PE/e $^-$  [57]. The different gains  $g_2$  are mostly ascribed to a different configuration of the multiplication and electroluminescence fields. The parameter  $g_2$  derived in this analysis is smaller than the value obtained from the study of S2-echo single-electron signals (see par. 4.3.3).

S1 and S2 yields used for the above analysis are summarized in the table 4.6.

Run no.	Source	$E_{drift}$ (V/cm)	$Q_y$ ( $e^-/keV$ )
1159	$^{241}\text{Am}$	0	-
1164	$^{241}\text{Am}$	100	6.2(3)
1135	$^{241}\text{Am}$	200	9.5(5)
1165	$^{241}\text{Am}$	400	14.1(7)
1160	$^{241}\text{Am}$	700	18.1(9)
1161	$^{241}\text{Am}$	1000	21.5(11)

Table 4.7: Charge yield values from double phase ReD data obtained following the analysis reported in the text. Errors are statistical only.

### Determination of the charge yield

The determination of the  $g_2$  factor can be used in order to convert the ionization yield, for the moment expressed in  $\text{PE}/e^-$ , in detector-independent units such as  $e^-/\text{keV}$ , i.e. extracted electrons per unit of recoil energy. In this case it will be the so-called charge yield ( $Q_y$ ).

The charge yield values of double phase  $^{241}\text{Am}$  runs taken in ReD with drift field between 0 and 1000 V/cm are summarized in table 4.7.  $Q_y$  is derived by dividing the S2 yields of tab. 4.6 to the factor  $g_2$  which describes the response in S2 of the TPC to a single electron. For the calculation, the value  $g_2 = (16.22 \pm 0.14) \text{ PE}/e^-$  derived from the S1-S2 anti-correlation was adopted. All S2 yields were corrected to account for electron losses by impurities along the drift path, as described in par. 4.3.1. Furthermore, the figure 4.23 shows the ReD experimental points together with two predictions obtained using the same Doke-Birks modified model used in the ARIS experiment [67]. The violet band, in particular, comes from Doke-Birks parametrization in case of ERs from  $^{241}\text{Am}$  S1/S1<sub>0</sub> data fit (the band is taken as statistical uncertainties), while the orange ones refer to ARIS published data taken as reference. ReD data are marginally consistent with the predictions. Possible reasons could be systematic uncertainties, for instance on the  $W$ -value, or a bias in  $g_2$ .

Following the same arguments of par. 4.2.3, the charge yield coming from an empirical modification of the Doke-Birks recombination model [67] is:

$$Q_y = \frac{N_i}{E}(1 - R) = \frac{1 - R}{W} \quad (4.21)$$

where  $N_i$  is the number of electron-ion pairs,  $R$  is the recombination probability and  $E$  is the recoil energy. The former, derived from double phase  $^{241}\text{Am}$  data and defined in eq. 4.13, is displayed versus electric drift field in figure 4.24.

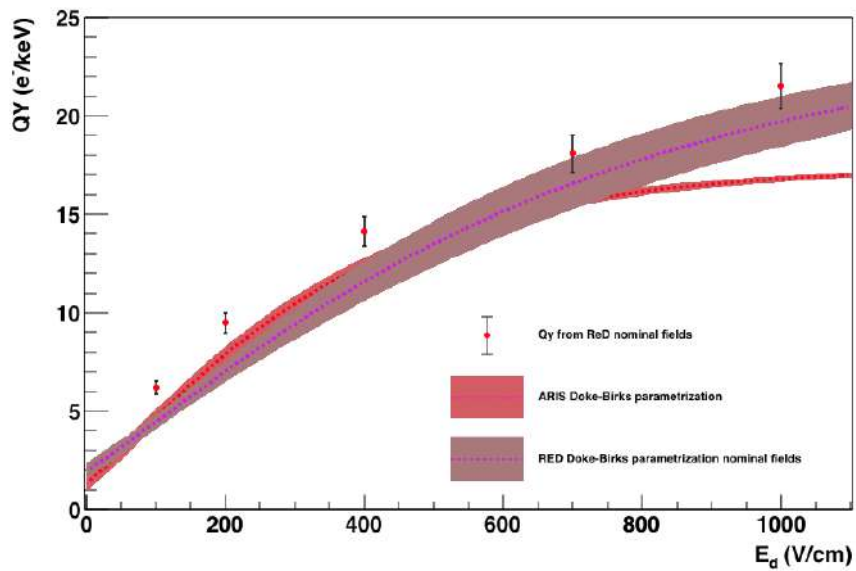


Figure 4.23: Charge yield ( $Q_y$ ) versus drift field for  $^{241}\text{Am}$  runs. Data come from ReD measurements are reported as red points together with a prediction from the modified Doke-Birks recombination model [67] to the ReD data (violet dotted line). The violet band is taken as statistical uncertainties, while the orange one refers to ARIS published data [67].

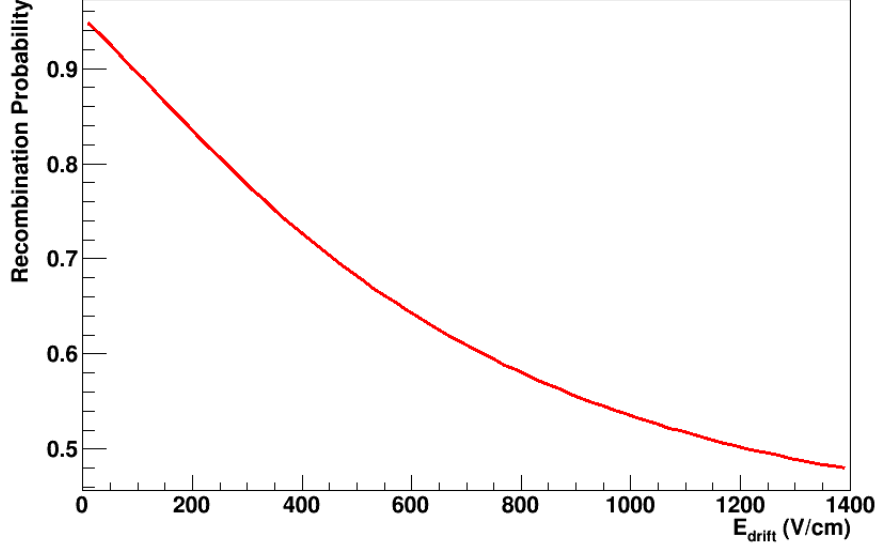


Figure 4.24: Recombination probability versus drift field from  $^{241}\text{Am}$  double phase data as defined in eq. 4.13.

### 4.3.3 S2 echoes: a tool to estimate $g_2$

An independent measurement of the photoelectron yield per extracted electron in the gas phase,  $g_2$ , can be done by looking at the so-called single-electron events. These are defined as events where a single electron is extracted in the gas phase, and the corresponding electroluminescence emission is the single-electron signal, i.e. S2 echo signals or S3s. S3s, in particular, are produced when a photon from S2 hits the cathode and extract a further photoelectron. Therefore, S3s come one maximum drift time later than the S2 signals. In ReD, with the nominal configuration of 200 V/cm, the maximum drift time,  $\tau_{drift}$ , is about 62  $\mu\text{s}$  (see par. 4.3.1). Figure 4.25 shows the raw waveform of a typical ionization signal with an S3 located at a maximum drift time (about 60  $\mu\text{s}$ ), while on figure 4.26, the drift time distribution of echo events is reported. The latter shows, in particular, drift time from S3 events (black line) together with time delay of S2 from S1 events as red line. The presence of a distribution of events peaked at about 60  $\mu\text{s}$  confirms that S3 events are detected one maximum drift time after the ionization signal S2 in the same DAQ window.

$^{83m}\text{Kr}$  data were used in order to perform the analysis reported here. As already mentioned, see par. 4, since electrons from krypton are uniformly distributed inside the active volume of the TPC, with this data sample, a



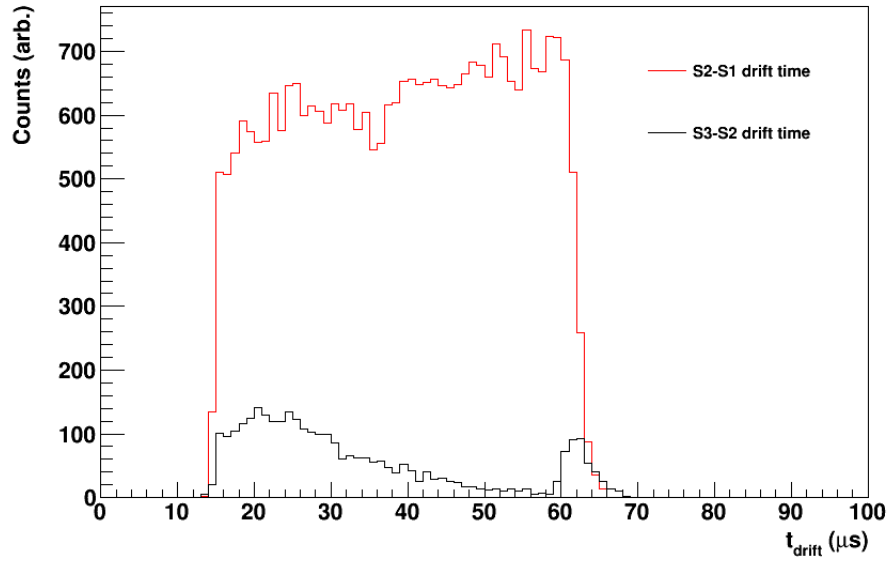


Figure 4.26: Drift time distribution of S2 echo events (S3s, black line) compared with S2 - S1 drift time distribution (red line). As mentioned in the text, S2 echoes are extracted from the cathode of the TPC. They have one maximum drift time difference with S2 on the same DAQ window.

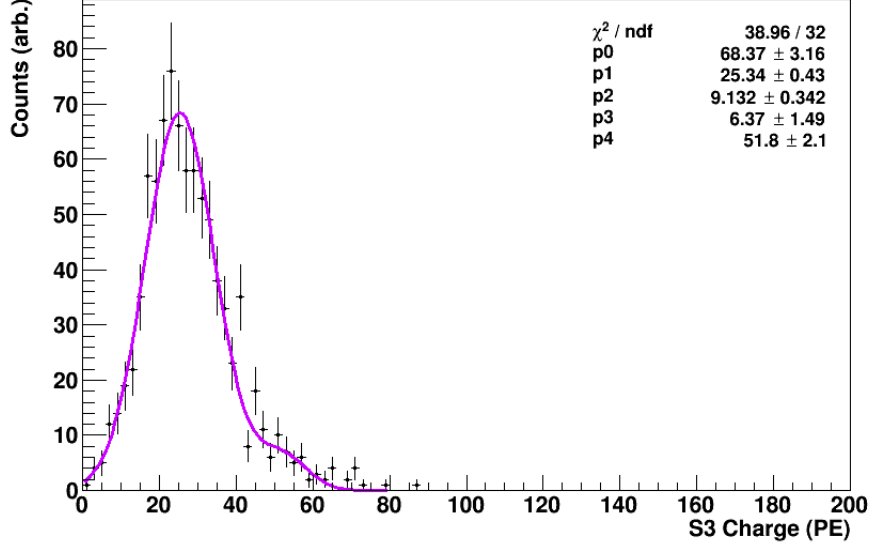


Figure 4.27: Spectrum of S3 events in  $^{83m}\text{Kr}$  data. The violet line is a fit from a sum of Gaussian functions (see text for details).

XY map of the events distribution inside the detector is also useful in order to understand the position of echoes. S3 charge distribution from  $^{83m}\text{Kr}$  data is shown in figure 4.27. Since S3s are produced by light pulses, like S1s and S2s, they have to be corrected for the same duplication factor ( $K_{dup}$ , see par. 4.1) of the latter. Violet line is a fit to a sum of Gaussian functions with means equal to  $g_2$ ,  $2 \times g_2$  and so on. The RMS in the fit was also fixed to  $2 \times \sqrt{g_2}$ , i.e. twice the expected value from a Poisson distribution. From the fit, the estimated value of  $g_2$  from S2 echoes is  $(25.34 \pm 0.43)$  PE/ $e^-$  with uncertainties from the fit. The latter is about 30% larger than the value reported in par. 4.3.2 ( $16.22(4)$  PE/ $e^-$ ) whose origin is still under investigation. A possible explanation can be related to the low efficiency of the clustering algorithm, that could not be able to identify lower pulse signals like S3s.

A proposed further independent investigation method is to looking for the  $g_2$  value from data taken with the getter turned-off. The getter cartridge, in fact, allows for the purification of liquid argon in the recirculation system (see par. 3.3.3). Searching for S2-like single scatter events after a standard S2 - S1 signal from contaminations, in fact, allows the possibility to use the position of i.e. normal events as the one of the single drifted ioniza-

tion electron<sup>7</sup>. In such a way, the large uncertainties on XY position of the reconstructed echo events can be also further reduced.

---

<sup>7</sup>Contamination elements like oxygen inside the liquid argon can capture drift electrons and release them in a short time at the same position.

# Chapter 5

## Liquid Scintillator Characterization

This chapter is devoted to the characterization of the neutron spectrometer used in ReD. The test was performed at INFN - Laboratori Nazionali del Sud (LNS) in Catania, at the end of February 2019 during a beam stop phase, by using a  $^{252}\text{Cf}$  neutron fission source and several radioactive sources for the gamma-rays calibration. Neutrons of  $O$  (MeV) must be detected in ReD in order to probe the angular dependence of the ionization signal (S2) with respect to the electric drift field. For this reason it is of extreme importance to have a precise knowledge of the absolute efficiency of the neutron detectors (LScis) composing the neutron spectrometer of ReD.

In the following an overview of the results on the absolute efficiencies of the LScis and the performance of the pulse shape discrimination (PSD) method used in the offline analysis, will be reported. The performed test also served as a benchmark for the timing performance of the data acquisition system (DAQ). Finally, from the  $\gamma$  calibration sources, a study of the linearity response of the detectors will be presented.

### 5.1 Organic liquid scintillators

Organic liquid scintillators are widely used for the detection of fast neutrons, also thanks to their powerful capability in discriminating neutrons and gamma components of an incoming radiation. Liquid scintillators often use a solvent, i.e. a liquid with a high concentration of hydrogen molecules for neutron interactions and electrons for gamma rays. Furthermore, an organic scintillator mixture can be added with a wavelength shifter, which absorbs the prompt scintillation light (the so-called *fluorescence*) remitting

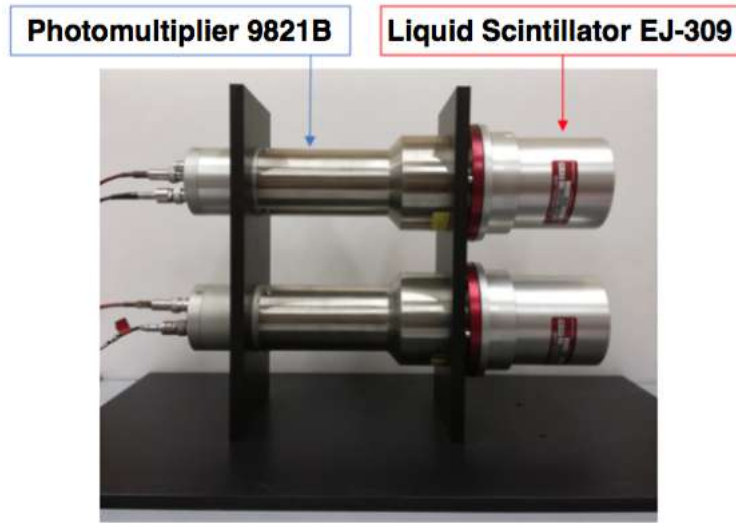


Figure 5.1: Two of the nine SCIONIX liquid scintillator detectors used for the neutron spectrometer of the ReD experiment, during a testing phase.

it at a longer wavelength. This is particularly useful when a liquid scintillator is coupled with a photomultiplier tube, like in the case of those used in the ReD experiment. The scintillation yield of any scintillator is defined as the fraction of the total particle energy released in the scintillator that produces visible light. This can be reduced by the so-called quenching processes: all mechanisms that degrade the light output, such as de-excitation processes or the presence of impurities, i.e. oxygen, dissolved in the scintillator, provide quenching mechanism for the excitation energy. Another important characteristic of radiation detectors is the linear response upon the energy of charged particles of the light output.

Finally, the capability to scintillate together with their fast response and the low  $Z$ -value of their mixture elements, makes the organic scintillators excellent candidates to detect fast neutrons.

Table 5.1 summarizes the properties of the EJ-309 scintillator used in ReD.

### 5.1.1 Pulse Shape Discrimination

As already shown in par. 2.1, also in the case of organic scintillators, by analyzing the prompt to slow component ratio of the signals, it is possible to distinguish the interacting ionizing particles. More specifically, i.e. scintillation light from fast electrons shows that the greater part of the signal is generated within the prompt component, compared to recoil protons from,

Properties	EJ-309
Light output (rel. to Antracene)	75%
Proton yield / MeV electrons	11.500
Maximum of emission wavelength	424 nm
Density (15°)	0.964 g/cm <sup>3</sup>
H:C ratio	1.25
C atoms per cm <sup>3</sup>	4.37×10 <sup>22</sup>
H atoms per cm <sup>3</sup>	5.46×10 <sup>22</sup>
Electrons per cm <sup>3</sup>	3.17×10 <sup>23</sup>
Flash point	144°C
Decay time short component	≈ 3.5 ns
Refractive index	1.57
Light attenuation coefficient	1 m

Table 5.1: Properties of the Eljen Technology EJ-309 scintillator used in ReD. It is not listed as dangerous material and, in order to increase the neutron sensitivity, can be doped with Boron up to a weight percent of 5% of natural boron (EJ309:B5).

e.g. neutron interactions.

Several methods were developed in order to discriminate events in a liquid scintillator, but the simplest one is the so-called charge integration method. It simply consists in the integration of the pulse amplitude of a signal over two time intervals. The long gate is a time interval that contains the entire pulse, while the short one contains only the fast component. The pulse shape discrimination (PSD) parameter, is then, by definition, the fraction of the slow component with respect to the total [73]:

$$PSD = \frac{Q_{long} - Q_{short}}{Q_{long}} \quad (5.1)$$

where  $Q_{long}$  and  $Q_{short}$  are charge integrals of the long and short gates, respectively.

Finally, a conventional method to characterize the PSD discrimination capability of the detector is to quantify the so-called Figure of Merit (FoM), defined as:

$$FoM = \frac{S}{\sqrt{\sigma_e^2 + \sigma_p^2}} \quad (5.2)$$

with  $S$  the distance between the neutrons and gammas centroids, and  $\sigma_e^2 + \sigma_p^2$  the sum in quadrature of sigmas of each peak [73]. Detailed description of FoM analysis is reported in appendix C.

## 5.2 Experimental setup

The ReD neutron spectrometer experimental apparatus consists of an array of nine 3-inch liquid scintillator detectors, made by the SCIONIX company, containing a commercial organic liquid scintillator mixture EJ-309 from Eljen Technology, coupled with a 3-inch ETL 9821B PMT. The latter, in particular, is a 78 mm (3-inch) diameter end window photomultiplier with blue-green sensitive bialkali photocathode mounted on a plano-concave window, and twelve BeCu dynodes of linear focused design to guarantee good linearity and timing. The bulk system (fig. 5.2) has a 32.5 cm height aluminum, 3.81 cm radius cylindrical enclosure in which the EJ-309 liquid scintillator and the PMT are hermetically sealed in a light-tight housing with a beryllium optical window. It also has two BNC-type connectors (Anode and Dynode) for the signal acquisition and a SHV-type connector for the voltage supply.

The setup used during the test (fig. 5.3) employed a  $^{252}\text{Cf}$  neutron fission source and the neutron spectrometer array of ReD. Eight of the nine liquid scintillator detectors (far LScis), in particular, were placed on their own supporting structure (wheel). The ninth one, called near detector, faced a 65.6 kB  $^{252}\text{Cf}$  source. The far detectors were then used to detect neutrons and/or gammas from a fission event. In such a way a measure of absolute efficiency can be obtained by the so-called tag-and-probe method: the near detector is used to trigger on fission products (either  $\gamma$ s or neutron), searching for neutron coincidence events in the far ones, delayed by the time-of-flight (ToF) [74]. In such a way, and in order to perform timing studies on the DAQ system, the method was used to have a measure of the ToF distribution of neutrons events which can be converted in a kinetic energy distribution for neutrons. The mean distance between the near and the far detectors was about 1 m. The source was placed on an *ad-hoc* supporting holder and, during all the data taking phase, at a distance of about 3.3 cm from the near detector. A top view of the experimental setup is drawn on figure 5.4. The electronics used during this measurement were almost the same used during the ReD standard data taking: signals coming from the neutron detectors were digitized by two CAEN V1730D Flash ADC boards, 8 channels each with a 14-bit resolution, a 2 V<sub>pp</sub> input range and 500 MHz sampling rate, while a hardware trigger was set-up by using a standard NIM logical module by ORTEC coupled with a Lecroy 428F linear FAN-IN/FAN-OUT module. Voltage to the photomultipliers was supplied by the same CAEN SY 5527 power supply module used in ReD. Slow control system, DAQ and reconstruction softwares were also the same as used during the standard ReD operations.

## 5.2. Experimental setup

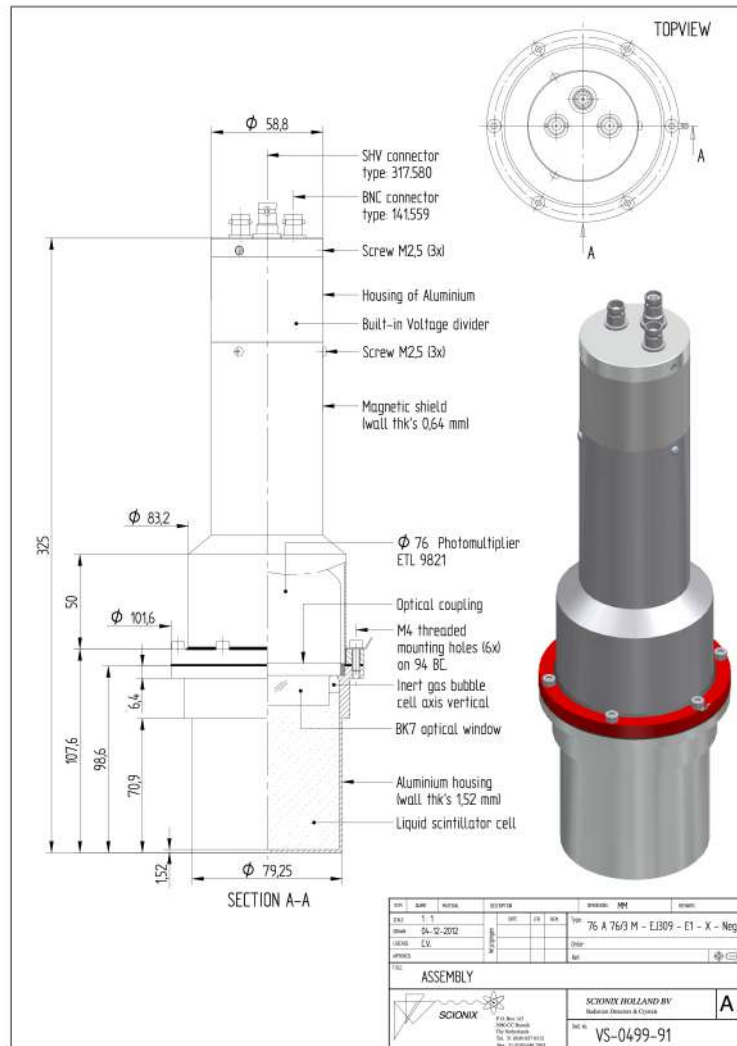


Figure 5.2: Technical design of the ReD liquid scintillator neutron detector (<https://scionix.nl/standard/tab-id-3>).



Figure 5.3: Experimental setup used at LNS to calibrate the ReD neutron spectrometer. Eight of the nine liquid scintillator detectors were placed on the supporting structure (far detectors), while the ninth (near detector) faced a  $^{252}\text{Cf}$  neutron fission source in order to tag fission events (details in the text).

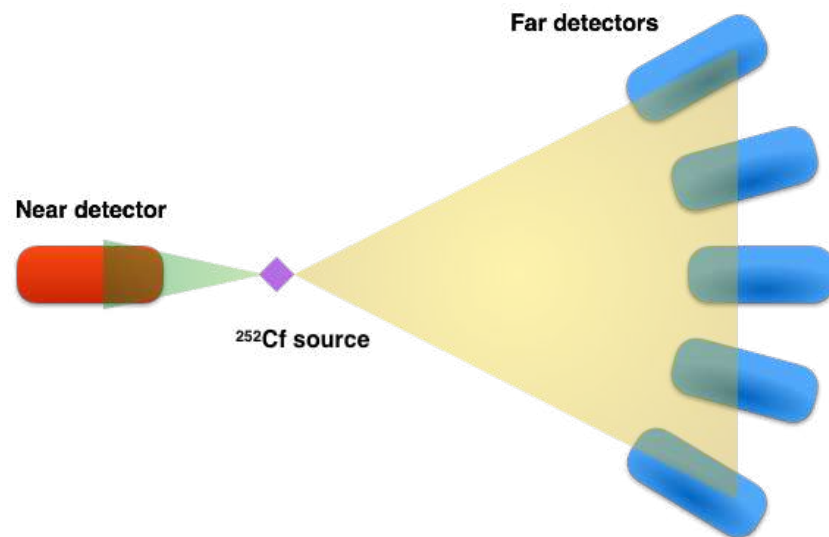


Figure 5.4: Drawing of the setup from a top point of view: neutron detectors are shown (colored cylinders) together with the neutron source (violet) and a pictorial representation of the particle beams (green and yellow cones). The hardware components are not into scale.

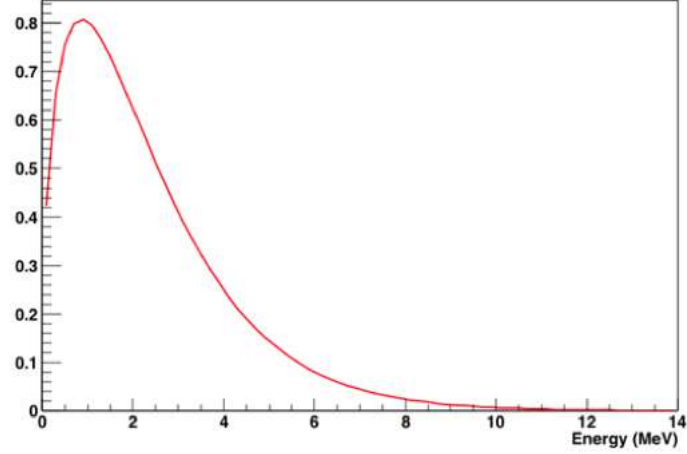


Figure 5.5: Calculated spectrum of  $^{252}\text{Cf}$  neutron fission source (eq. 5.4).

Energy calibrations of the scintillation light with  $\gamma$ -sources ( $^{22}\text{Na}$ ,  $^{137}\text{Cs}$  and  $^{241}\text{Am}$ ) were performed using a RooFit numerical convolution algorithm of the Klein-Nishina formula<sup>1</sup> [75] with a Gaussian resolution function.

### 5.2.1 Theoretical spectrum and expected rates

$^{252}\text{Cf}$  is a spontaneous neutrons fission source. It shows  $\alpha$  decay with 96.908% occurrence to form  $^{248}\text{Cm}$ , while undergoes spontaneous fission in the 3.1% of cases producing neutrons with a multiplicity of 3.76 events per fission, energy in the range between 0 and 13 MeV, a mean energy of 2.3 MeV and a most probable value at 1 MeV [76].

The theoretical shape of the fission neutrons energy spectrum is taken according to the Maxwellian distribution:

$$f(E) = a\sqrt{ET}^{3/2}e^{-E/T} \quad (5.4)$$

with  $a$  normalization constant and  $T = 1.406$  MeV. The distribution is taken between 0 and 14 MeV (fig. 5.5).

<sup>1</sup>The Klein-Nishina formula is:

$$\frac{d\sigma}{dT} = \frac{\pi r_e^2}{m_e c^2 \alpha^2} \left( 2 + \frac{s^2}{\alpha^2 (1-s)^2} + \frac{s}{(1-s)} \left( s - \frac{2}{\alpha} \right) \right) \quad (5.3)$$

whit  $T$  kinetic energy of the scattered electron,  $r_e$  is the classical radius of electron,  $\alpha = h\nu/m_e c^2$  and  $s = T/h\nu$ , where  $h\nu$  is the photon energy [75].

Energy (MeV)	Measured Efficiency ( $\epsilon$ ) (%)	Exp. from MC (%)
2.4	$35.2 \pm 5.4$	$32.73 \pm 0.05$
7	$28.3 \pm 6.1$	$23.63 \pm 0.05$

Table 5.2: Measured and expected absolute efficiencies of the neutron liquid scintillator cells used in ReD for the neutron spectrometer, for a neutron energy of 2.4 MeV and 7 MeV at an energy threshold of 100 keV<sub>ee</sub> on both near and far detectors. Errors are statistical only.

For the purposes of the measurements presented here, the number of neutrons impinging on the far detectors is calculated such that:

$$\int f(E)dE = N_{fiss}n_m \frac{\Delta\Omega}{4\pi} \quad (5.5)$$

where  $N_{fiss}$  is the total number of fissions tagged by the near detector<sup>2</sup>,  $n_m = 3.76$  is the average number of neutrons per fission [77] and  $\Delta\Omega = 0.03695$  sr is the total solid angle from the eight far detectors. About  $10^4$  neutrons are expected to leave an energy deposit into any of the far detectors in about 1 hour.

Monte Carlo simulations were also performed using an *ad-hoc* modified version of the G4DS code (see par. 3.4) used for ReD. The simulation considers two 3-inch liquid scintillator cells filled with EJ-309 organic material, with a density of 959 kg/m<sup>3</sup> and a H:C ratio of 1.25. A simulated <sup>252</sup>Cf source at about 0.5 cm from the face of the tagger LSci, produces fission neutrons with a multiplicity value of 3.76, that are revealed in coincidence with a far detector at a distance of about 1 m. A total of 1M events are generated per each run. Results of expected and measured absolute efficiency at 2.4 MeV and 7 MeV energy at 100 keV<sub>ee</sub> (i.e. keV-electron-equivalent<sup>3</sup>) energy threshold are reported on table 5.2 together with the statistical errors.

<sup>2</sup>If the detectors had 100% efficiency, one would expect to detect about 1.1 coincidences for 100 fission events in the near detectors, due to pure solid angle effects.

<sup>3</sup>The notation *electron equivalent* is often used to have the light yield output of a scintillator on an absolute scale. In this case, by definition, in order to produce 1 MeV<sub>ee</sub> of light output, a particle energy of 1 MeV (several MeV) is required for fast electrons (protons) [72].

Source	Activity (kBq)	$\gamma$ peak (keV)	Compton edge (keV)
$^{22}\text{Na}$	2	511	340.67
		1274.54	1061.71
$^{137}\text{Cs}$	24.8	661.66	477.34
$^{241}\text{Am}$	34.2	59.54	-

Table 5.3: Activities,  $\gamma$ -peaks and Compton edges of used sources during the calibration measurements of the ReD neutron spectrometer.

## 5.3 Experimental results

### 5.3.1 Energy calibrations

In order to have an energy calibration of each detector, runs with  $^{22}\text{Na}$ ,  $^{137}\text{Cs}$  and  $^{241}\text{Am}$   $\gamma$ -sources were performed prior to the irradiation with  $^{252}\text{Cf}$ . Table 5.3 summarizes the characteristic of used sources.

The yield of the scintillation light in a liquid scintillator depends on the nature of the particle involved in the process, while the light output can be not linear, for example for electrons below 40 keV or above 1.6 MeV [72]. Furthermore, because of the finite resolution of the detectors, the Compton edges of the sources are smeared. This represents the main reason why the analysis of the calibration data presented in this chapter was performed using a RooFit numerical convolution algorithm of the Klein-Nishina formula [75] with a Gaussian resolution function, in order to reproduce the resolution of the detectors. As an example of the fit procedure used to the calibration data, figure 5.6 shows the  $^{137}\text{Cs}$  spectrum taken with one of the nine liquid scintillator detectors. The best-fit of the Compton edge at 477.34 keV (corresponding to 661.66 keV full-energy peak) is also reported (green line) together with the background spectrum taken with the same detector. The energy resolution, defined as  $\sigma/E$  with  $E$  the energy of the Compton edge, is  $\sigma/E = (1.6 \pm 0.1)\%$ . Figures 5.7 and 5.8 report the best-fits of the  $^{241}\text{Am}$  59.54 keV full-energy peak and the two Compton edges of the  $^{22}\text{Na}$  calibration energy spectrum (340.67 keV and 1061.71 keV respectively, corresponding to 511 keV and 1274.54 keV full-energy peaks).

Figure 5.9 reports, as example, the linearity response of one liquid scintillator detector in the energy range from 59.54 keV ( $^{241}\text{Am}$  full-energy peak) to 1274.54 keV  $\gamma$ -ray by  $^{22}\text{Na}$ . The curve was obtained by using the  $^{22}\text{Na}$  and the  $^{137}\text{Cs}$  Compton edge energy measurements (see the following appendix B for quenching studies.)

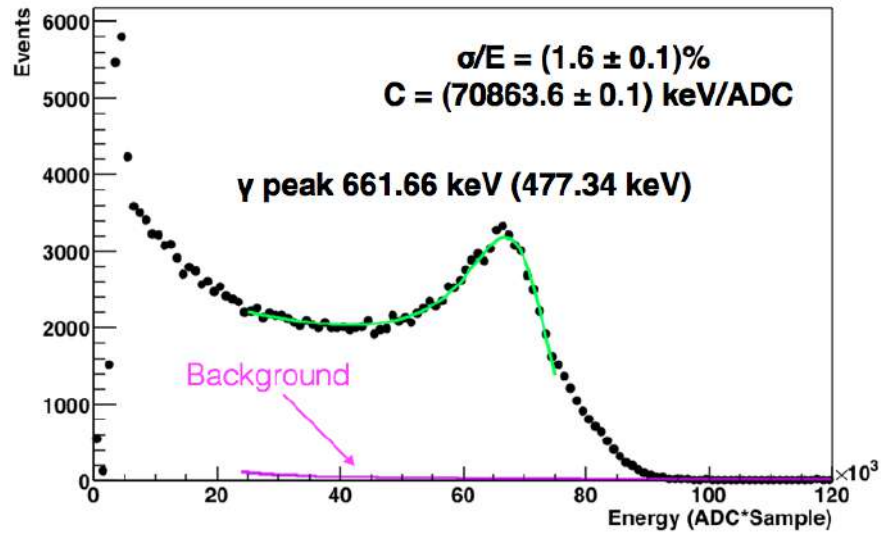


Figure 5.6:  $^{137}\text{Cs}$  calibration energy spectrum on a liquid scintillator neutron detector using the numerical convolution algorithm described in the text. The best-fit curve is also reported (green line), together with the background spectrum for the same detector (violet line). The energy resolution is also indicated.

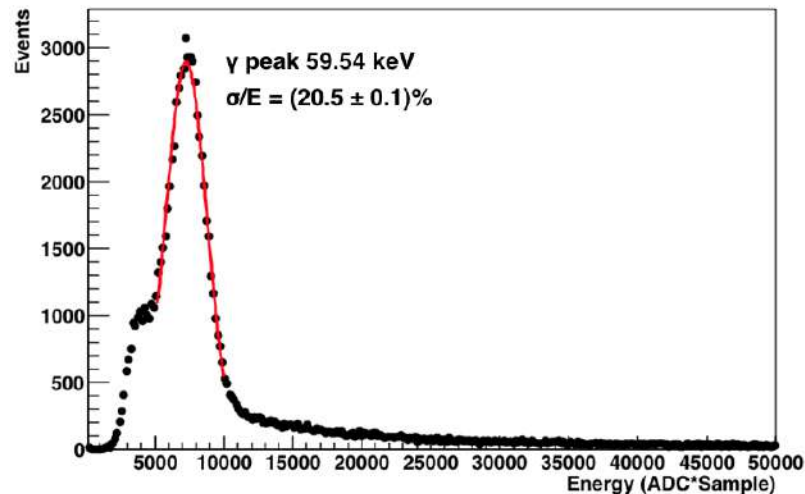


Figure 5.7:  $^{241}\text{Am}$  calibration energy spectrum of the same detector as in fig. 5.6. The energy resolution of the full-energy peak together with the best-fit curve (red line) is also reported.

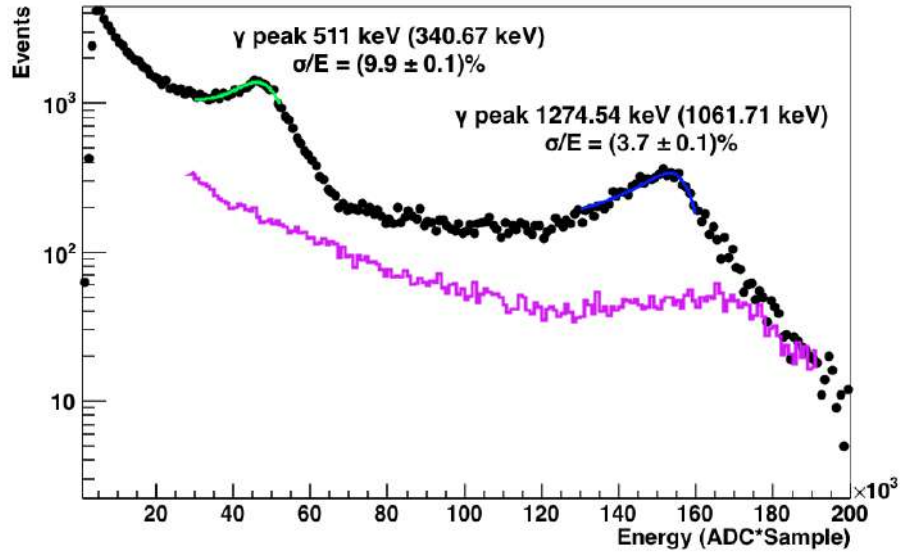


Figure 5.8: Best-fit (green and blue lines) of the two Compton edges of  $^{22}\text{Na}$  taken on the same detector used for the one reported in figure 5.6. The violet line is the background spectra measured from the same detector. The energy resolutions of both the Compton edges are also indicated.

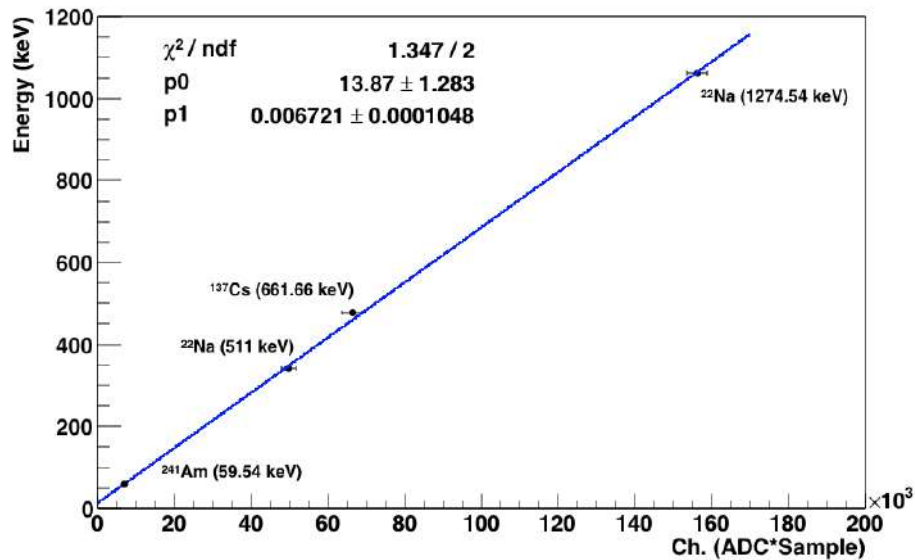


Figure 5.9: Linearity response of one liquid scintillator detector in the energy range from 59.54 keV ( $^{241}\text{Am}$  full-energy peak) to 1274.54 keV  $\gamma$ -ray by  $^{22}\text{Na}$ .

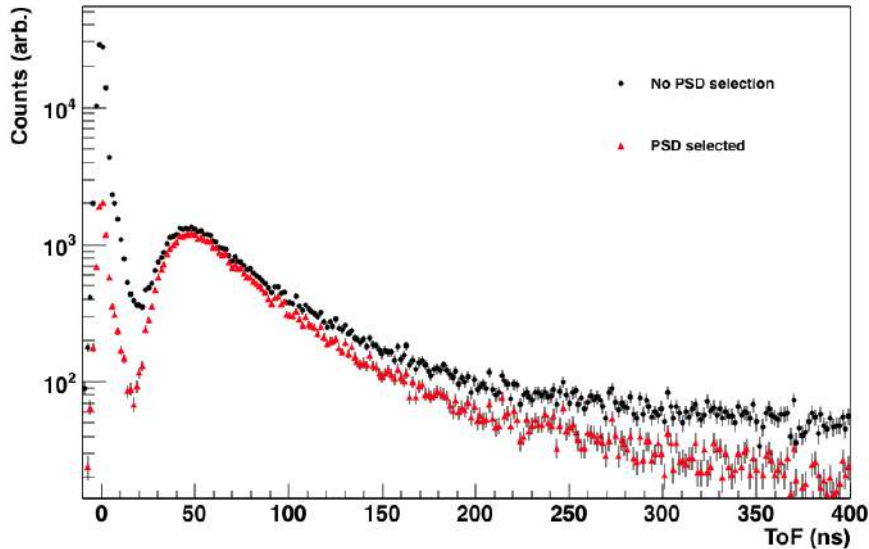


Figure 5.10: Time-of-flight spectrum with (red triangles) and without (black points) gamma-rays PSD rejection (see appendix C for details). Energy threshold on the near detector is  $100 \text{ keV}_{ee}$ .

### 5.3.2 Time-of-flight analysis and time shift correction

The tag-and-probe method was used to measure time-of-flight (ToF) distribution of neutron events. In this analysis, a so-called time coincidence run was used: tagging a prompt event in the near detector, and searching for a neutron event in coincidence with the far detectors. An example of ToF spectrum is displayed in fig. 5.10. It shows the prompt gamma-ray peak, with a ToF centered at about 3 ns, and the neutron hump, i.e. the distribution of fission neutrons [77]. The figure also shows the same ToF distribution with (red triangles) and without (black points) PSD selection criteria<sup>4</sup>. The pulse shape discrimination parameter was used, in particular, to cut gamma events: PSD parameter on the far detectors is requested to be above 0.13 such to select neutrons. The effect of the PSD selection is evident from the figure. It shows a significant reduction of the gamma-ray contribution to the overall spectrum at an energy threshold of  $100 \text{ keV}_{ee}$ , followed by a reduction of the uncorrelated environmental background, or gamma and residual neutrons coming from the source but not produced in the same fission event tagged by the near detector. The measured neutrons

<sup>4</sup>Refer to appendix C for further details.

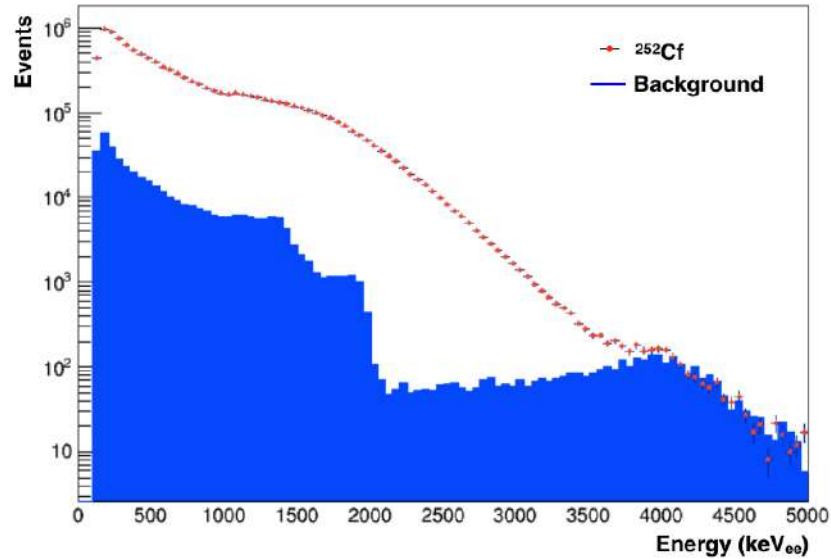


Figure 5.11: Measured spectrum of  $^{252}\text{Cf}$  in the near detector (red points) superimposed with a measured background spectrum due to environmental radiation (blue filled region).

spectrum coming from the  $^{252}\text{Cf}$  source in the near detector (red points) is shown in figure 5.11, superimposed with the measured environmental background (blue filled region). The background was estimated to be the 3.8% of the total.

Timing studies were also performed in order to refine the time-of-flight analysis and to cross check the baselines (i.e. the distance between the  $^{252}\text{Cf}$  source and the detectors) of the different LScis involved in the measure. An example is shown in figure 5.12 and in figure 5.13 for a background and a  $^{252}\text{Cf}$  source run, respectively. The former, in particular, shows background gammas. The left-hand peak in the spectrum is due to a gamma interaction in the far detector that leaves a track also in the near one, as pictorially drawn on fig. 5.14(a). The right-hand peak, on the other hand, comes from background events that after the interaction in the near detector, scatters in the far ones, too (fig. 5.14(b)). Their time delay can be used to calculate the baseline between the tagger and the prober detectors for the correlated background gamma events and the time offset correction. Also from the  $^{252}\text{Cf}$  events (figure 5.12), one can see two peaks structures in the time-of-flight spectrum. Those are due to the prompt gamma from the source. The left hand peak comes from a backscattered event correlated with the prompt emission (fig. 5.14(c)), while the main peak on the right is due to prompt

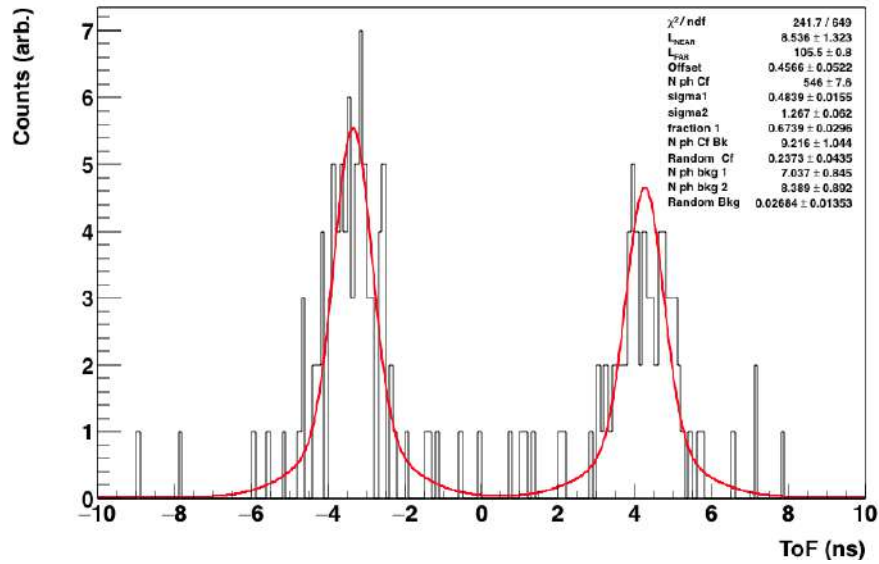


Figure 5.12: Measured background gamma spectrum used to derive baselines and background events fraction in the near detector in time coincidence with the far ones.

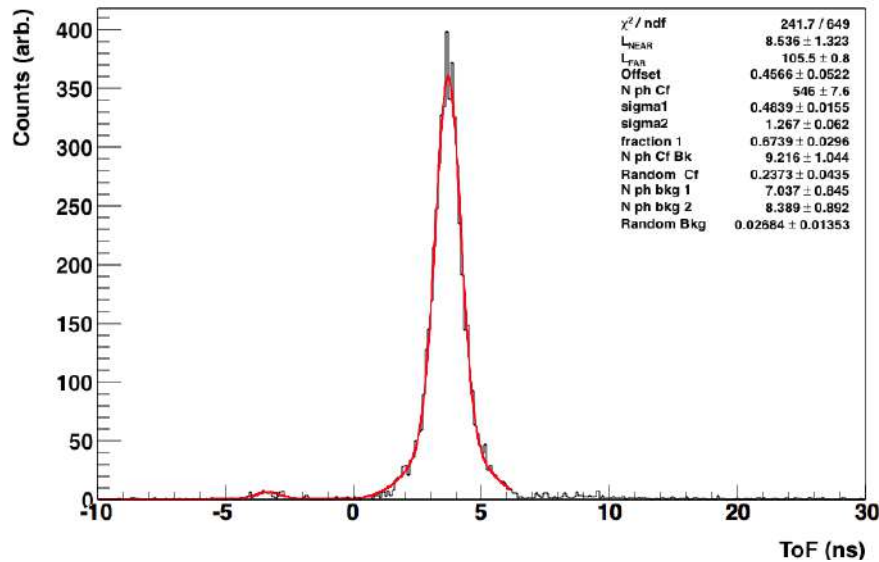


Figure 5.13: Measured gamma spectrum from  $^{252}\text{Cf}$  in the near detector in time coincidence with the far ones.

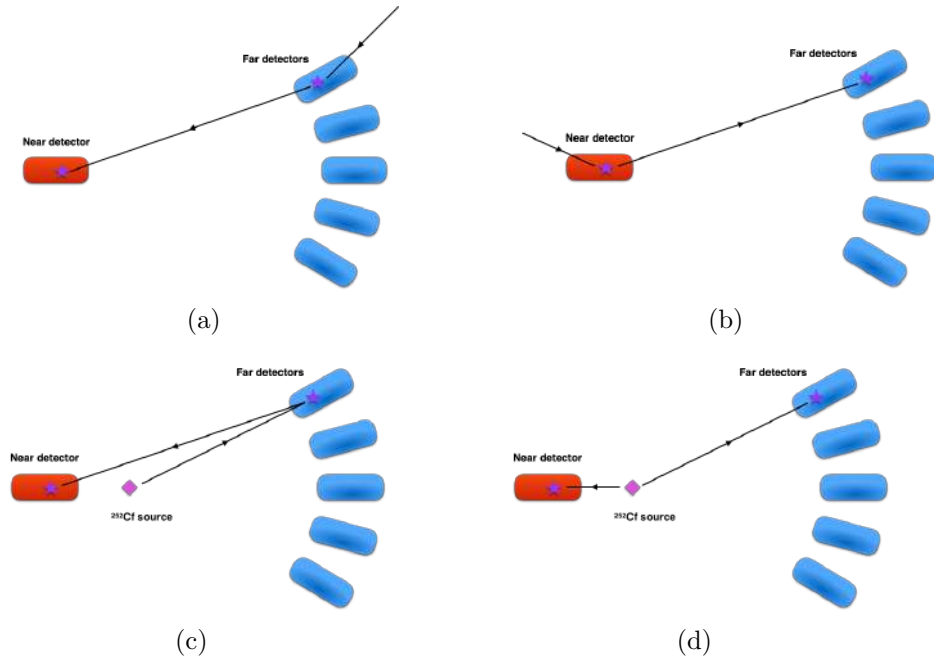


Figure 5.14: Drawings of a typical gamma interaction from background and  $^{252}\text{Cf}$  source in the LSis. On (a) is represented a background event that after the interaction in the far detector leaves a track also in the near one (negative values of ToF). (b) The same as the previous one, but in this case the gamma firstly interacts in the near and then in the far detectors (positive ToF). On (c) and (d) are reported, on the other hand, a gamma event from the  $^{252}\text{Cf}$  source that interacts in the far and then is backscattered in the near detector, and gamma from a single fission event scattered in the near and in the far detectors, respectively.

gammas emitted in the same fission event (fig. 5.14(d)). Finally, from a combined fit of the four gamma peaks, information about baselines, fraction of background events, offset and time resolution of the gamma peaks for each detector pairs can be inferred. The time offset was observed to be channel dependent, and it was in a range between about 2 and 8 ns. From this analysis a time resolution of about 0.5 ns rms, was also measured. Summarizing, time-of-flight spectra are produced using the following set of analysis cuts:

- time-of-flight is corrected according to the channel by channel baseline shifts determined by the above mentioned timing analysis;
- energy on the near detector is requested to be above  $100 \text{ keV}_{ee}$ ;

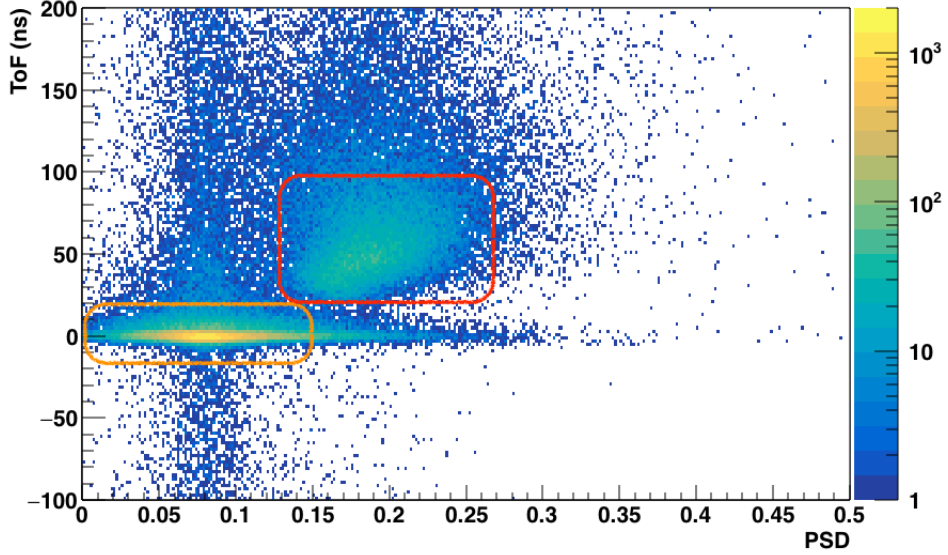


Figure 5.15: Time-of-flight scatter plot versus PSD parameter. Groups of events are highlighted by open colored rectangles (see text for details).

- multiplicity on the far detectors is requested to be one: only one far detector must have energy above  $20 \text{ keV}_{ee}$ ;
- energy on the far detectors is requested to be above a given threshold  $T$  (the default is  $100 \text{ keV}_{ee}$ ).

Time-of-flight spectrum versus PSD parameter is shown in fig. 5.15. In the figure two main groups of events can be distinguished:  $^{252}\text{Cf}$  neutrons (red box) and prompt gammas (orange box). This was also used to made a better selection on neutron events in order to derive the energy spectrum of the far scintillators.

Energy spectrum of the neutrons entering the scintillators was, then derived from the conversion of the time-of-flight spectrum above (fig. 5.15) into a variable bin size spectrum. The ToF spectrum was divided into 70 bins, each 2 ns wide, starting from 24 ns. Each of the edge of these bins was then converted in energy bins ( $E_i$ ) as follows:

- a numerical calculation of the velocity was performed:

$$\beta_i = \frac{d}{t_i c} \quad (5.6)$$

with  $d$  the average distance between the source holding structure and the far detectors and  $c$  the speed of light;

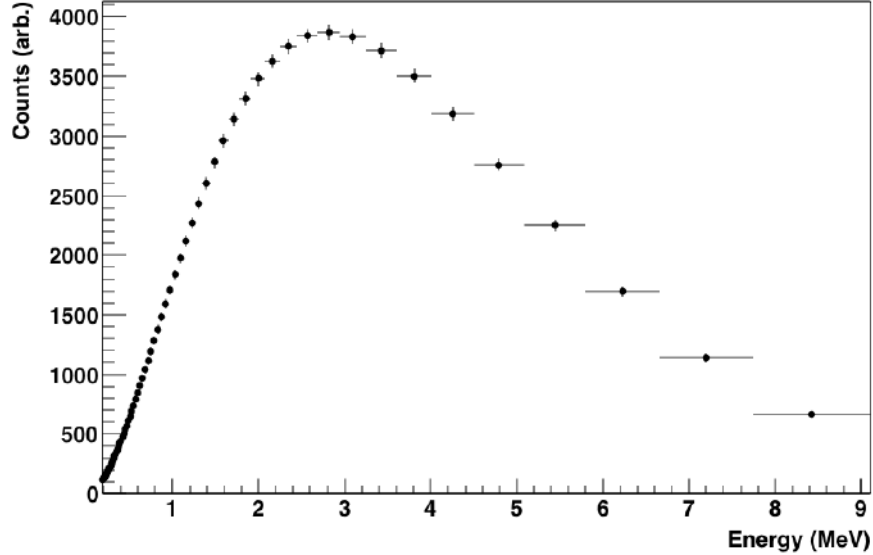


Figure 5.16: Incoming neutron energy in one far detector obtained from the ToF distribution following the procedure described in the text.

- calculation of the energy value was also performed:

$$E_i = m_N(\gamma_i - 1) \quad (5.7)$$

where  $m_N$  is the neutron mass (939.56 MeV) and  $\gamma_i$  is the relativistic correction  $\gamma_i = 1/\sqrt{1 - \beta_i^2}$ .

Kinetic energy was then calculated as listed above from the actual ToF events using the also listed cuts. The flat source-correlated background was then subtracted, calculated by taking the average of the ToF spectrum between 800 and 1200 ns, where only accidentals and pile-up events were expected. This made an average background of about 0.4575 counts/ns, while no correction was applied for the environmental background which is much smaller than the source-correlated one. Figure 5.16 reports the incoming neutron kinetic energy spectrum measured in one of the far detectors, obtained with the analysis procedure described above.

### 5.3.3 Neutron efficiency

The theoretical spectrum calculated in par. 5.2.1 was, then, used in order to calculate the neutron efficiency curve. The content of each bin of this

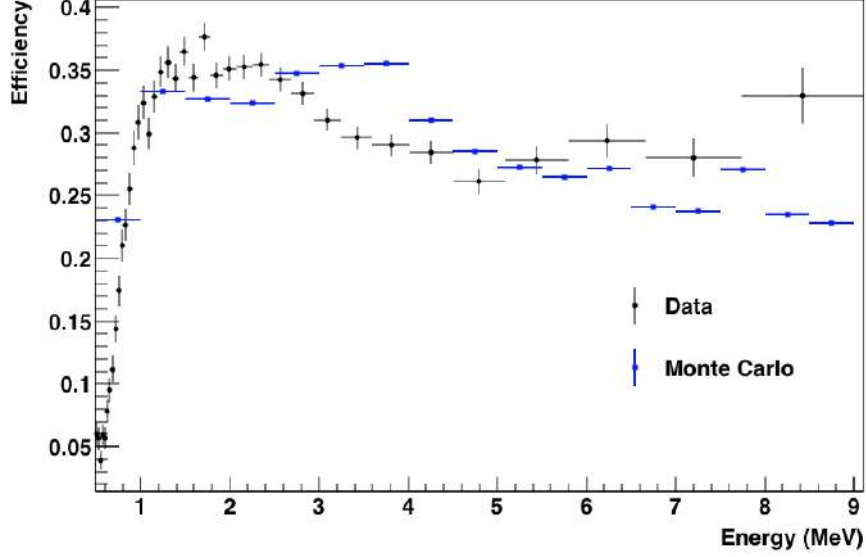


Figure 5.17: Absolute efficiency profile from the ReD neutron spectrometer (black points) compared with Monte Carlo expectations (blue line), details in the text.

spectrum was calculated as the integral of the function along one bin, as:

$$h2_i = \int_{E_i}^{E_{i+1}} f(E)d(E). \quad (5.8)$$

So, after the identification of neutron events from the  $^{252}\text{Cf}$  source, thanks to the PSD, the energy spectrum was divided by the theoretical one in order to obtain the absolute efficiency profile versus the neutron energy. It was chosen a set of data with the trigger in the near detector, an energy threshold in the far ones to be above  $100 \text{ keV}_{ee}$  and a neutron multiplicity of 3.76 as reported in ref. [77]. Several quality checks were also performed in order to be sure of the analysis procedure delineated above. In figure 5.17 the absolute efficiency profile spectrum taken from the ReD neutron spectrometer (black points) is displayed together with the Monte Carlo prediction, represented by blue points (see appendix D for channel-by-channel results). The spectrum averaged absolute efficiency is  $\epsilon = (26.8 \pm 5.4)\%$  for an energy threshold of  $100 \text{ keV}_{ee}$ , the uncertainty are statistical only. On the other hand, selecting only events with an energy deposit of 7 MeV in the liquid scintillator, the measured absolute efficiency is  $\epsilon = (28.3 \pm 6.1)\%$ , with the same energy threshold on the far detector as before. This value can be compared with

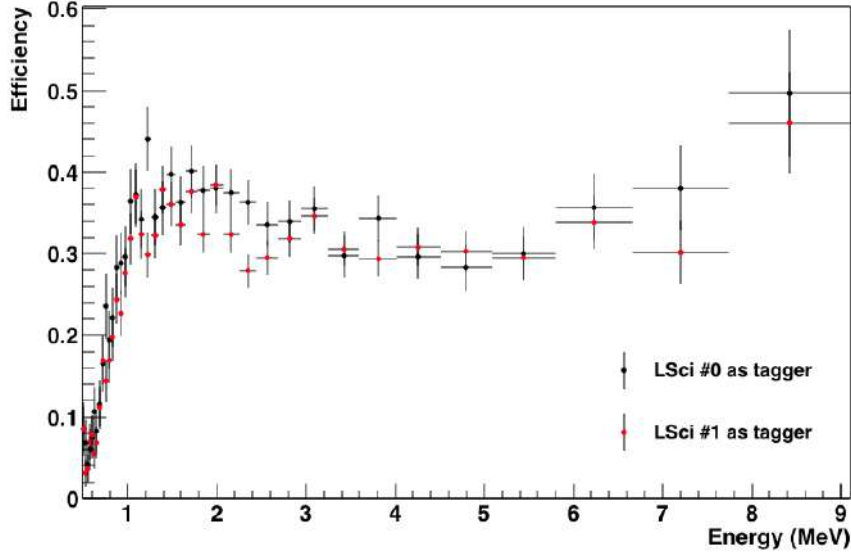


Figure 5.18: Comparison between two measured absolute efficiency profiles from the same liquid scintillator detector (LSci #2) used in different trigger conditions. Black points refer to LSci #0 as near detector and red ones are from LSci #1 as the near one (details in the text).

the efficiency  $\epsilon = (33.0 \pm 1.6)\%$  reported in ref. [74] for a 2-inch neutron detector instead of the 3-inch used in ReD.

Finally, figure 5.18 shows the absolute efficiency measured from the detector LSci #2. The efficiency of this detector was measured twice in different configurations. Black points, in particular, refers to the case in which LSci #0 was used as near detector (the so-called tagger) while coincidence events were searched in the LSci #2. The second set of data were taken, then, by swapping the tagger LSci #0 with the LSci #1. This allows to double check the measured efficiencies. So, at 7 MeV energy and for a  $100 \text{ keV}_{ee}$  threshold, from the black points an efficiency of  $37.6(4)\%$ , while a value of  $30.9(5)\%$  from the red ones were found, respectively. The spectrum-averaged measured efficiency ( $E = 2.4 \text{ MeV}$ ) for the same detector as above is  $35.7(3)\%$  and  $28.2(4)\%$  in the two trigger cases at an energy threshold of  $100 \text{ keV}_{ee}$ . So an estimation of the systematic error can be done, calculated as the quadratic sum of the differences between the above efficiency measurements. A value of about  $10\%$  was found.

## Chapter 6

# ReD at Laboratori Nazionali del Sud

The integration of the system in its final position at INFN - Laboratori Nazionali del Sud (LNS) in Catania is a non-trivial operation since it is composed by three different independent parts, as seen in par. 3.3. The picture 6.1 was taken after the deployment of the full system, before the starting of data taking with the beam. The primary  ${}^7\text{Li}$  beam enters the experimental hall from the bottom left corner of the picture, impinging the target inside the scattering chamber (the big silver cylinder on the left side along the beam pipe) that also contains the  ${}^7\text{Be}$  tag silicon detectors, while outgoing neutrons pointing towards the TPC (housed within the cryogenic system in the blue chart in the middle of the picture) are finally detected in the neutron spectrometer behind the system.

ReD was deployed in the beam line for the first time in June 2018, and two test beams with the full system followed during July 2018 and September 2018 for the complete integration and the characterization of the system. During the two tests beams, in fact, all the components were operated together for the first time, the silicon telescopes for the detection of  ${}^7\text{Be}$  tested and calibrated, and so the neutron spectrometer and the TPC, by using external sources and neutron beam. This was also a good opportunity for testing the electronics and the DAQ system with all operative channels (about 40) at the same time. At the end of operations, the ReD TPC was shipped back to Naples for the full commissioning (see cap. 4) while some collaborators continued the tests in Catania with the neutron spectrometer only. The physics run with the full system is expected to be performed early 2020. The author of this dissertation took part of both the testing phases in Naples and in Catania, contributing to the mounting phases but also with the data taking and analysis.

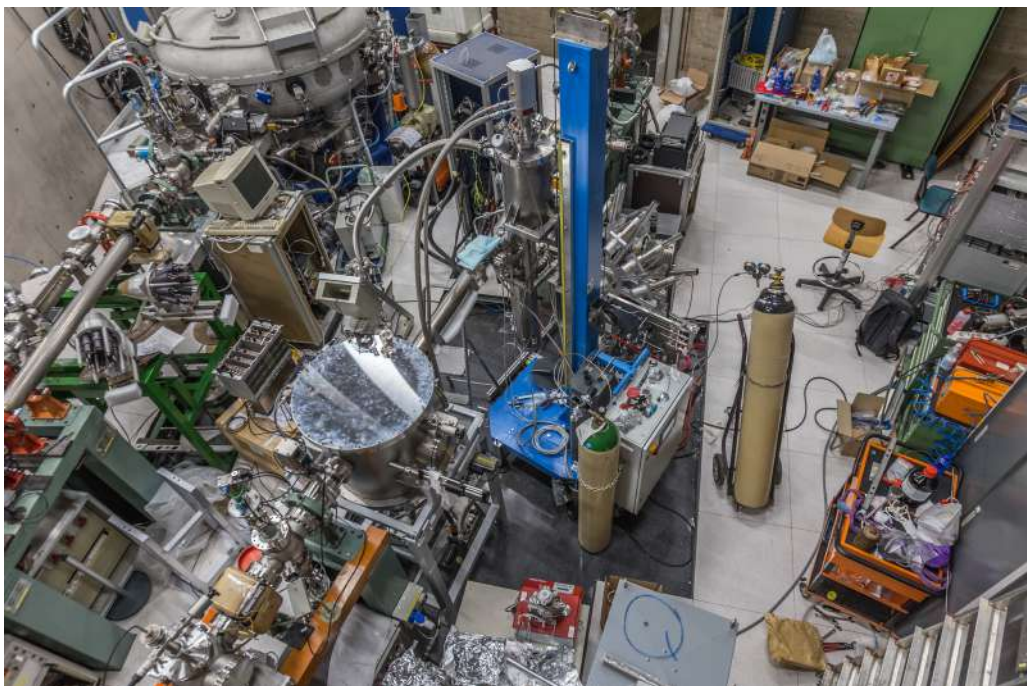


Figure 6.1: The integration of the ReD experiment at the “80 degrees” of the beam line at INFN - Laboratori Nazionali del Sud in Catania. The silver big cylinder on the left is the scattering chamber, while the blue chart in the middle is the cryogenic system that contains also the TPC with the neutron spectrometer behind it.

This chapter will be devoted to the commissioning phase of the neutron beam at LNS, with a focus on the testing phase of the high precision movement system for the silicon telescopes inside the scattering chamber (see par. 3.3). The latter was performed in July 2019.

## 6.1 Testing the neutron beam

### 6.1.1 Experimental setup

As already mentioned in par. 3.3.2, during the neutron beam testing phase performed in July 2019, the two silicon detectors of the telescope were mounted on a precision movement system in order to perform a fine tuning of their position without stopping the beam and opening the scattering chamber. The deployment of this new system was necessary because of the uncertainties in the telescope absolute position during the mounting phase. Because of the geometry of the experiment, and the kinematics of the reaction, an imprecise alignment can be the cause of the low statistics measured during the physics runs with the full system. The collimator on the silicon telescope inside the scattering chamber has, in fact, a  $\varnothing(3\text{ mm})$  diameter that, at a distance of about 46.5 cm from the target (see par. 3.3.2), corresponds to a  ${}^7\text{Be}$  aperture angle of about  $0.4^\circ$ . The ReD TPC and the neutron spectrometer are located at about 150 cm and 230 cm from the target, respectively. Outgoing neutrons intercept the TPC at an angle of about  $22.3^\circ$ , and they form an aperture cone of about  $2^\circ$  at the TPC distance. So, assuming the TPC efficiency to be unity, from the geometry of the experiment, a precision of about  $0.15^\circ$  in the placement of the silicon telescope is requested, while it is about 0.5 cm for both the TPC and the neutron spectrometer.

The experimental apparatus used during the test was made by five of the nine 3-inch liquid scintillator detectors (LSi) placed on a custom made supporting structure located at the same distance from the target of the expected TPC position, with the central one, in particular, located at exactly the same location (150 cm from the target and  $22.3^\circ$  with respect to the beam line, see par. 3.3). During the data taking, the other 3 detectors were left in their original position on their own supporting structure (the so-called wheel).

Data were taken in two different trigger modes: single mode, i.e. acquiring signals coming from both the silicon detectors with all LScis acquired in slave mode, and double-coincidence mode, where also a trigger on at least one neutron detector is requested. In figure 6.2 a picture of the experimental

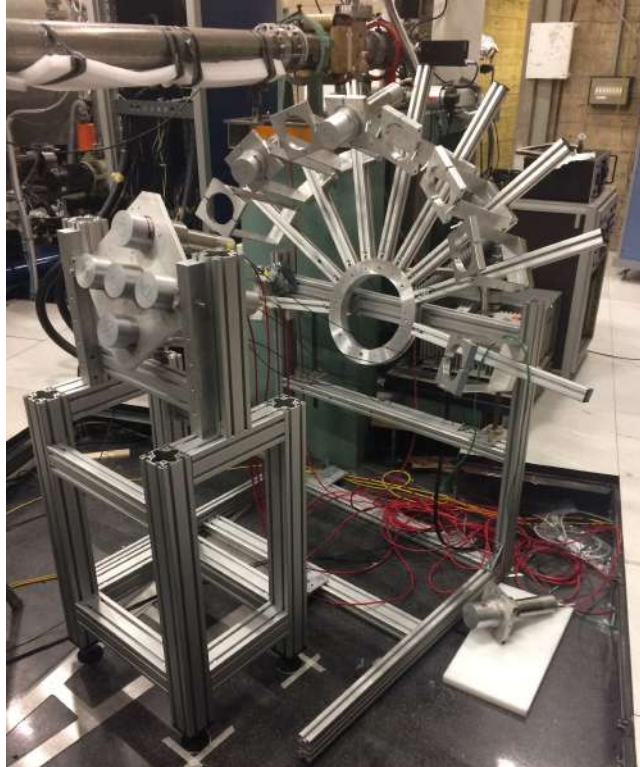


Figure 6.2: Photo of the experimental apparatus used for the neutron beam test. The five neutron detectors are arranged on a custom made structure and are placed at 150 cm from the target and at 22.3 degrees with respect to the beam line as the ReD TPC should be. Behind them the other detectors in their usual location, while on the floor one detector was placed in order to have a measurement at 45° and in the same reaction plane which contains the beam line and the silicon telescope.

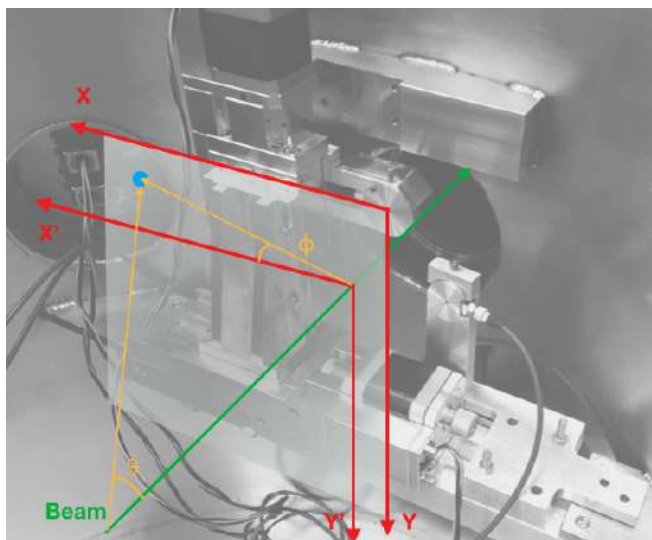


Figure 6.3: Reference frames used for the calibration of the precision movement system. The picture contains the  $(X,Y)$  reference frame in which the motor is centered at its own  $(0,0)$ , and the  $(X',Y')$  frame used in order to calibrate the system with respect to the main beam direction.

setup is shown.

### 6.1.2 Preliminary results

The main goal of the measurements presented here is the commissioning of the precision movement system by performing a scan in the motor position in order to check for the best working point that:

- maximize the fraction of  ${}^7\text{Be}$  events, coming from the proper kinematical locus, with an associated neutron-like event in the central LSci, i.e. the position of the TPC;
- maximize the fraction of events in the central LSci with respect to the side ones;
- favor the most symmetric configuration.

Figure 6.3 shows the method used for the position calibration of the motor system. Defining the reference frame  $(X,Y)$  in which the movement system has its own  $(0,0)$  in a fixed position, the  $(\theta_{7\text{Be}}, \phi_{7\text{Be}})$  angular coordinates of the impinging particle are defined with respect to a reference frame  $(X', Y')$  defined within the beam direction. It is then possible to derive the  $(X,Y)$

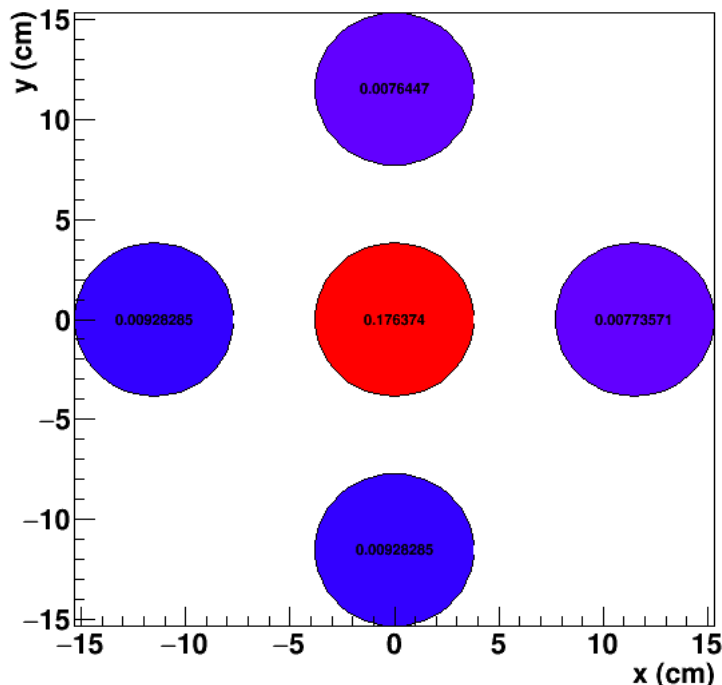


Figure 6.4: Fraction of events in the 5 LScis from the commissioning of the precision movement system. The reported numbers are the fraction of neutrons events seen by each LSci in coincidence with the silicon telescope detector (i.e. tagging the proper  ${}^7\text{Be}$  energy in the silicon telescope). The angular position of the telescope in this configuration is  $\theta_{7\text{Be}} = 5.05^\circ$  and  $\phi_{7\text{Be}} = 56.37^\circ$ .

position of the motor axes starting from the chosen angular coordinates in the primed system.

In July 2018 runs the nominal  $\theta_{7\text{Be}}$  was fixed to 5.15 degrees in order to have neutrons at  $22.3^\circ$  (see fig. 3.8), while the  $\phi_{7\text{Be}}$  angle was constrained by the telescope collimators (see par. 3.3.2). This limited the degrees-of-freedom of the hardware because there was no way to change the angular positions of the silicon telescopes without opening the scattering chamber and physically replace the collimators. Furthermore only a limited set of collimators were available. Preliminary analysis of the test beam performed in July 2019 with the precision movement system confirms the proper positioning of the TPC during the past runs. The best working point is  $\theta_{7\text{Be}} = 5.05^\circ$  and  $\phi_{7\text{Be}} = 56.37^\circ$  with the higher hit counting (about 84%) on the central detector, as

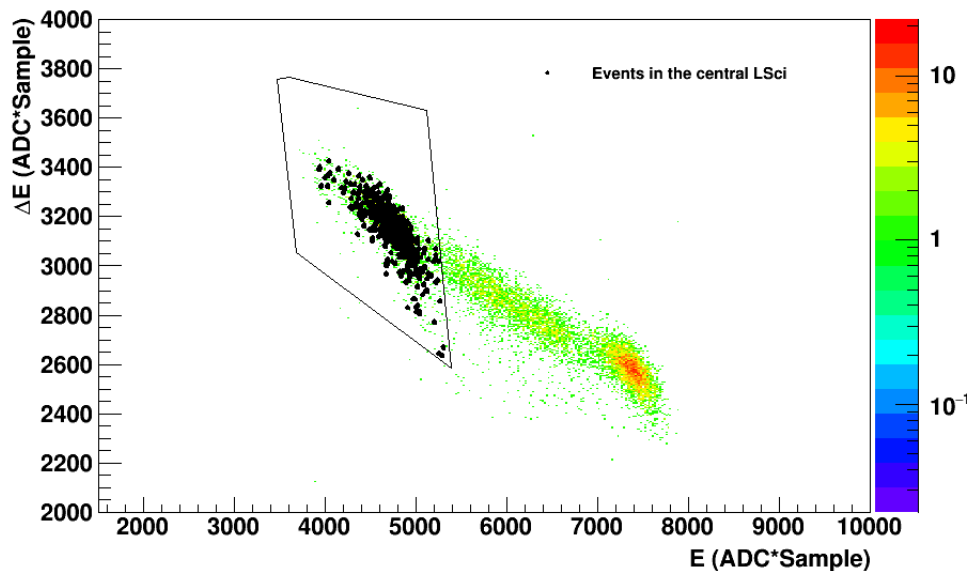


Figure 6.5: Events selection in the silicon detector from the commissioning of the precision movement system. It shows, in particular, the coincidence events with the central neutron detector (black points) and the graphical cut (black line region) used for the events selection in the analysis. The angular position of the telescope in this configuration is  $\theta_{7\text{Be}} = 5.05^\circ$  and  $\phi_{7\text{Be}} = 56.37^\circ$ .

shown in fig. 6.4. The same conclusion can be shown referring to the figure 6.5. It shows  $^7\text{Be}$  events in coincidence with the central neutron detector (black points) that mimic the TPC position. These events were then selected (underlined selection in the figure) for the calculation of events fraction in each neutron detector of the setup.

During the same test an inverse cross check was also performed: hitting a well-defined neutron detector starting from the calculated kinematics. The latter is in fact well known so, scanning the angle of  $^7\text{Be}$ , the emission angle of neutrons also changes (fig. 6.6). Figures 6.7 and 6.8 show the results for  $\theta_{7\text{Be}} = 4.6^\circ$  and  $\phi_{7\text{Be}} = 48.44^\circ$ , and  $\theta_{7\text{Be}} = 5.45^\circ$  and  $\phi_{7\text{Be}} = 47.93^\circ$ , respectively. The plot in figure 6.7, shows, in particular, neutron events in the case of the upper most LSci was targeted, while in figure 6.8 the right most one was selected as target detector. The above plots were obtained by requesting triggering  $^7\text{Be}$  events in the silicon telescope, an energy deposit in the neutron detectors of about  $30 \text{ keV}_{ee}$  and a PSD parameter greater than 0.12 for the neutron-like events (see par. 5.1.1).

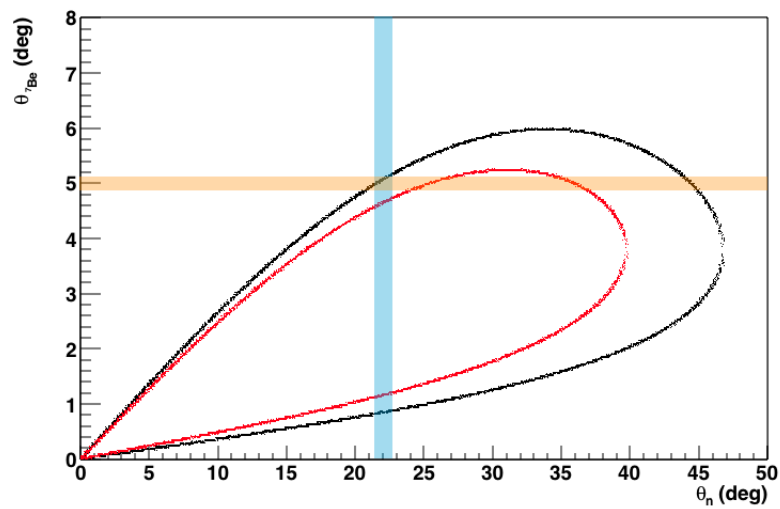


Figure 6.6: Angular correlation between  $\theta_n$  and  $\theta_{{}^7\text{Be}}$  from the  $p({}^7\text{Li}, {}^7\text{Be})n$  two body reaction at 28 MeV  ${}^7\text{Li}$  beam energy. The x axis shows the angle of outgoing neutrons  $\theta_n$ , while on the ordinate there is the  ${}^7\text{Be}$  emission angle,  $\theta_{{}^7\text{Be}}$ . Red curve refers to the first excited state of  ${}^7\text{Be}$  (about 429 keV), while the black one to the ground state. The two colored bands are pictorially representations of the working range values chosen during the measurements.

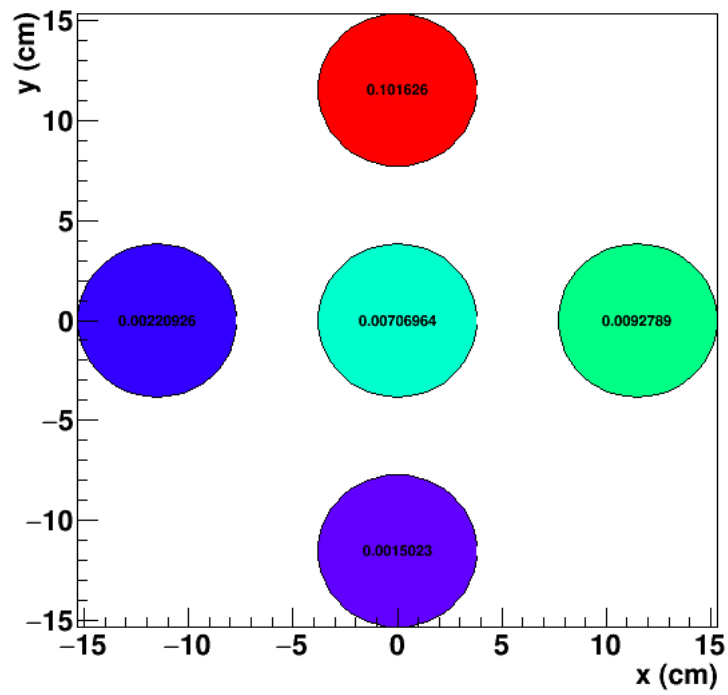


Figure 6.7: Fraction of events in the LScis in case of targeting on the upper most neutron detector. In this case  $\theta_{7\text{Be}} = 4.6^\circ$  and  $\phi_{7\text{Be}} = 48.44^\circ$ .

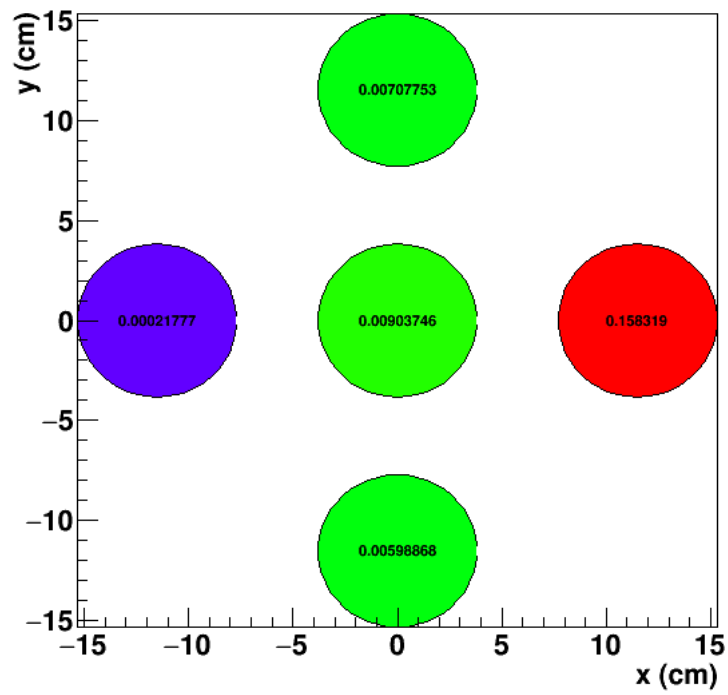


Figure 6.8: The same as fig. 6.7 but targeting on the right most LSci of the setup. Angular positions of the silicon detector are  $\theta_{\tau_{\text{Be}}} = 5.45^\circ$  and  $\phi_{\tau_{\text{Be}}} = 47.93^\circ$ .

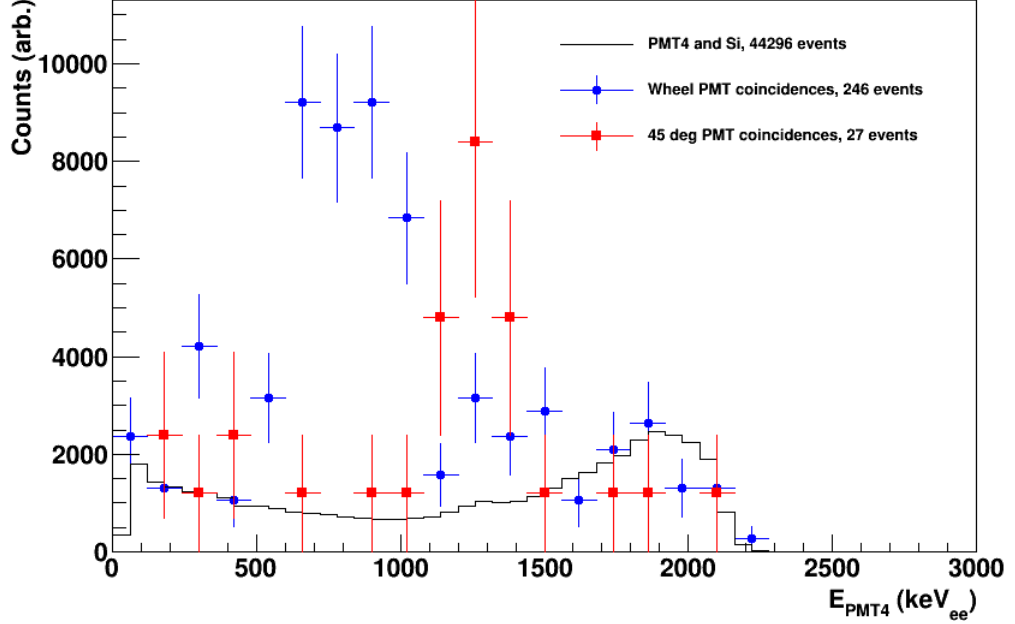


Figure 6.9: Triple coincidence events from the July 2019 test beam with a trigger condition on the silicon telescope in AND with at least one of the LSci detectors on the supporting structure (details in the text).

A triple-coincidence run was taken during the last night of measurements. In this case only one LSci detector was left in the central position just to mimic the TPC, while the others were placed on their proper supporting structure. The trigger configuration was set in a way to request for an AND between the silicon telescope with at least one of the neutron detectors mounted on the wheel (refers to fig. 6.2 for a visual scan of the setup). The figure 6.2, also shows the presence of an additional LSci detector on the floor close to the supporting structure at an angle of about  $45^\circ$  with respect to the beam line. This angular position should be very close to the low-energy kinematic solution of the  $p(^7\text{Li},^7\text{Be})n$  reaction (see fig. 3.8) that corresponds to neutrons energy of about 2.38 MeV. So, recoil events in this neutron detector should come from the higher energy kinematical locus of  $^7\text{Be}$ . Figure 6.9 shows on the abscissa the energy deposit in the central LSci in the position of the TPC (PMT 4), in case of triple coincidence. The spectrum, in particular, refers to the coincidence between silicon telescope detector, the central LSci and at least one detector on the wheel with the blue dots. The red markers are the same triple coincidence as before but with

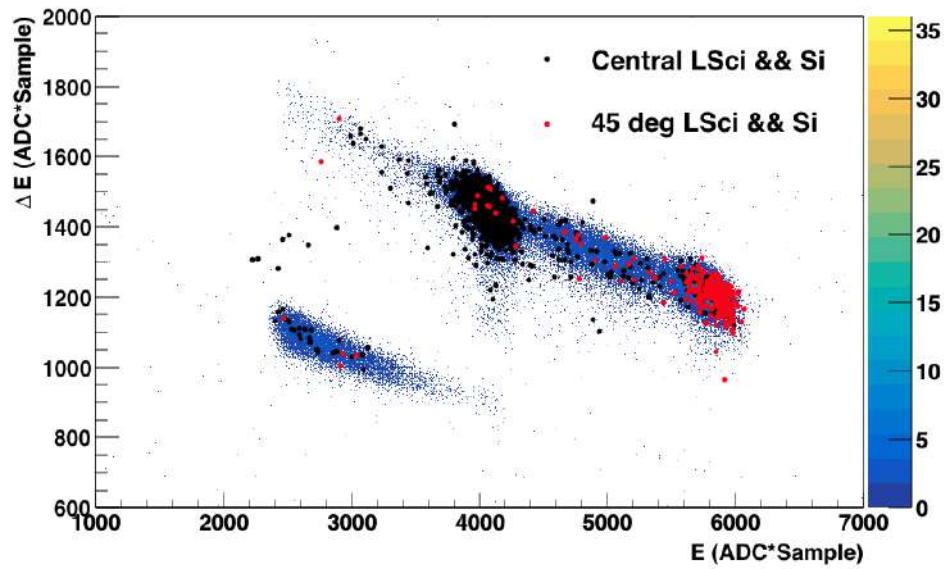


Figure 6.10: Scatter plot used for the triple-coincidence events selection. Blue points are the total of events seen in the silicon telescope, the superimposed black dots are the ones in coincidence with the central LSci detector and the red ones are events in coincidence with the LSci at  $45^\circ$ .

the LSci at  $45^\circ$  instead of one on the wheel, while the black continuum is a double coincidence between the telescope and the central neutron detector. Selecting events in coincidence with the central LSci, an estimation of the quenching of the liquid scintillator can also be done in order to have a cross-check with the value reported in ref. [74]. From kinematical calculations, in fact, neutrons scattered from the central detector, i.e. the TPC, have about 7.3 MeV kinetic energy as they impinge on a proton of the LSci at about  $36.8^\circ$  (see par. 3.3.5). At this angle, the proton will recoil with a kinetic energy of about 2.6 MeV. Since, from the spectrum in fig. 6.9, the energy released in the central LSci is about  $800 \text{ keV}_{ee}$ , the quenching in the liquid scintillator can be expressed as the ratio between the latter and the true value from the calculation:

$$Q = \frac{E_{ee}}{E_{true}}. \quad (6.1)$$

In the above equation,  $E_{ee}$  and  $E_{true}$  are the neutrons energy in electron-equivalent unit and the true kinetic energy expected from the kinematics expressed in keV, respectively. Furthermore, from the above eq. 6.1 the quenching value measured during this test beam is about 0.31(5) in good agreement with 0.33(2) reported in ref. [74].

Finally, in figure 6.10 a scatter plot used for the triple-coincidence events selection is reported: it shows a superposition between the total of  ${}^7\text{Be}$  events seen by the silicon telescope (blue colored points), selected events in coincidence with the central neutron detector (black points), i.e. the detector that mimics the TPC, while the red ones are events from the detector placed at about  $45^\circ$ . As mentioned above, the latter should see events that comes from the higher energy kinematical locus of the  ${}^7\text{Be}$  only, because of the kinematics. From the figure, it is possible to note also the presence of events due to accidentals or secondary scattering events in the detector.

# Conclusions

In the framework of the DarkSide program, the R&D project ReD (*Recoil Directionality*) aims to operate a Liquid Argon Time Projection Chamber (LAr TPC) to look for a possible directionality signature in the energy range of the expected WIMP-nucleus scattering recoils (up to 100 keV). The goal of the project is to irradiate a small LAr TPC with a neutron beam of known energy and direction by using the 15MV Tandem accelerator of the INFN - Laboratori Nazionali del Sud (LNS) in Catania, Italy. Neutrons are produced by means of the  $p(^7\text{Li}, ^7\text{Be})n$  two-body reaction in inverse kinematics, and then, thanks to the closed kinematics of the reaction, directed towards the TPC. Columnar recombination models suggest that the magnitude of the recombination effect between electrons and ions should vary with the applied electric field. Differences in the electrons-ions cloud are, in fact, expected for different ionization track orientations (parallel or perpendicular with respect to the electric field). Those effects can be explored by a deep characterization of both scintillation (S1) and ionization (S2) signals. Accurate measurements of S1+S2 and of the ratio S2/S1 may provide useful informations about the track directions (see par. 3.1). A Monte Carlo prediction on a possible directional effect in ReD, made with the ReD branch of the G4DS simulation toolkit (see par. 3.4), is shown in figure 6.11. The 2-D plot shows, in different colors, the ratio S2/S1, as measured by the first five liquid scintillator detectors of the neutron spectrometer of ReD, as a function of the energy of the scintillation signal S1, expressed in units of photoelectrons (PE). Since neutron detectors are fixed at different azimuthal angle with respect to the TPC but tagging the same neutron recoil angle, this allows to tag different Ar recoil angles with respect to the electric field applied to the TPC (see par. 3.3.5). So, in the above plot, different colors means different liquid scintillator detectors tagging different recoil track orientations.

Since ReD is composed mainly by three different, and independent, pieces, its complete commissioning and integration into the beam line at LNS was not trivial. Furthermore, since most of the technological solutions adopted

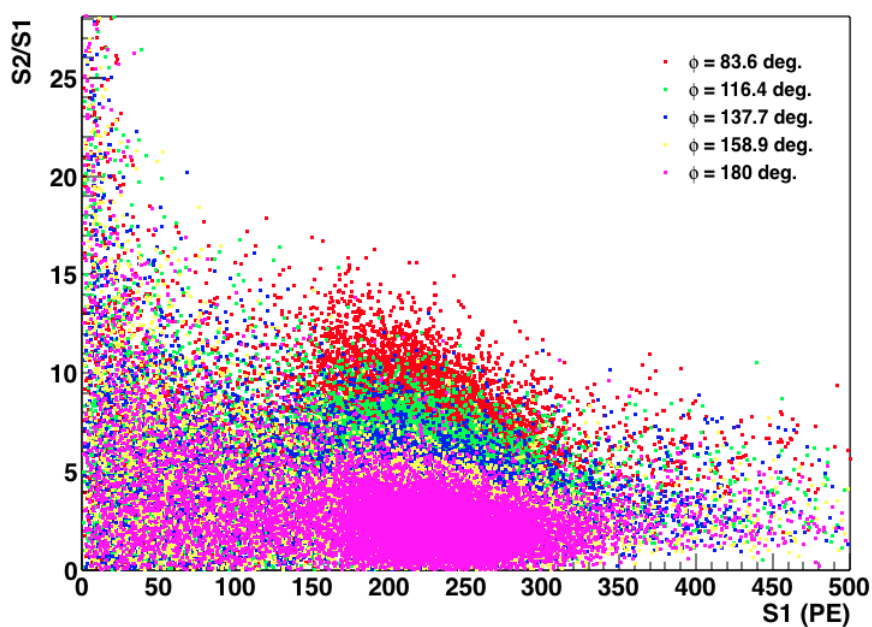


Figure 6.11: Simulated S2/S1 ratio versus S1 signal for directional effect prediction in ReD. Different colors refer to different liquid scintillator detectors used to tag recoiled neutrons from  $n+^{40}\text{Ar}$  elastic scattering.

in ReD will be part of the future DarkSide-20k detector it was crucial to have a complete characterization of the whole apparatus, in particular of the TPC. For all these reasons a complete review of the ReD experiment was done in this work, with a particular focus on the results that come from the latest calibration runs taken at Università degli Studi di Napoli Federico II, in collaboration with INFN - Sezione di Napoli.

Many of ReD experimental goals were achieved, as the first integration and the full characterization of two custom-made silicon photomultiplier detectors (SiPMs) with their cryogenic front-end electronics, achieving a good signal-to-noise ratio of about 30 and a good gain stability over the whole data taking period. ReD works properly both in single and in double phase, being capable to reproduce the data of the ARIS experiment in single phase [67]. The quenching effect due to the variation of the drifting electric field was also studied, confirming the dependence from field and energy of the scintillation response. A light output yield of about 8.4 PE/keV at 200 V/cm was measured from single phase  $^{241}\text{Am}$  runs, and confirmed also from  $^{83\text{m}}\text{Kr}$  and  $^{133}\text{Ba}$  measurements. The double phase runs analysis gave a value for the yield of extracted ionization electrons per unit of deposited energy at an extraction field of 5.79 kV/cm, that can be compared with ones reported from other experiments like SCENE [57], confirming also the capability of the system to extract electrons with high efficiency. Finally, ReD demonstrated the capability of running continuously in cold mode for long periods, even months, keeping a good stability of the whole system, reaching a good level of argon purity and a drift electron lifetime of the order of milliseconds.

The neutron beam at LNS in Catania was fully characterized by the fine tuning of the beam parameters and the complete characterization of the geometry of the setup. In this conditions the Tandem beam operators are confident to grant 20 nA of beam current for the next physical run scheduled at early 2020.

Should the directional effect be successfully observed, ReD will set a key milestone in the progress towards discovery of dark matter. Even if the directional sensitivity should not be confirmed, the experiment will have performed a complete and highly accurate investigation of all the aspects of the LAr response, providing a fully scalable technology to bring the future dark matter experiments based on LAr to the multi-ton scale, i.e. DarkSide-20k.

# Appendix A

## Matched filter to the Single Electron Response

Signal-to-Noise Ratio (SNR) of the detected pulses can be improved by filtering the raw waveforms. At cryogenic temperature, in particular, the large fraction of the signal charge is contained in the slow component of the waveform. In this conditions, the matched filtering technique results particularly effective since preserves the fast component of the signal, while maximizing the SNR yielding also a nanosecond timing resolution.

The matched filter was developed in the 50s to detect the bounced signal of pulsed radars from the random noise. The basic principle is that the pulse to be detected,  $s(t)$ , is the sum of a known signal,  $f(t)$ , and of stochastic noise  $\epsilon$ :

$$s(t | t_0, c) = c \times f(t - t_0) + \epsilon(t) \quad (\text{A.1})$$

where  $s(t)$  has two nuisance parameters,  $t_0$ , the time of the pulse, and a scaling factor  $c$  [78]. Several techniques were developed that demonstrate the power of this kind of filters in order to identify the signal  $f$  against the noise (i.e. SRN of amplitude). Among them, the one used in ReD is basically the convolution of a known, time reversed, signal, called kernel, with the signal itself:

$$\hat{s}(t | t_0, c) = s(t | t_0, c) \otimes f(-t) \quad (\text{A.2})$$

where  $\otimes$  is the convolution operator.

So, in order to apply the matched filter to the digitized waveforms of ReD (fig. A.1), the kernel  $f(-t)$  is obtained extracting the single photoelectron average waveform from data (fig. A.2), and then applied to the convolution algorithm (fig. A.3). Because of the high number of channels acquired, and the high number of events processed in a laser run, running the actual

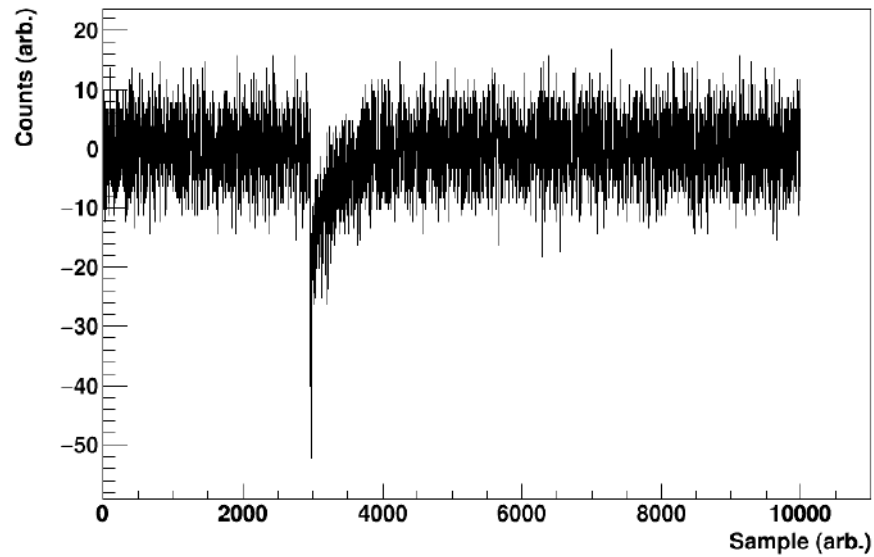


Figure A.1: Raw waveform from a single channel used for the convolution in the matching filtering algorithm (see text for details).

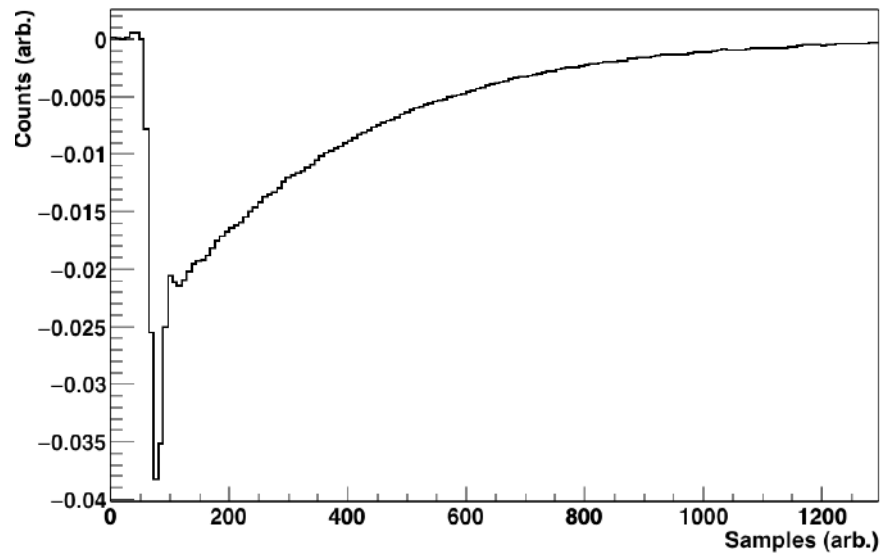


Figure A.2: Single photoelectron average waveform used as kernel in the matched filter for the waveform filtering.

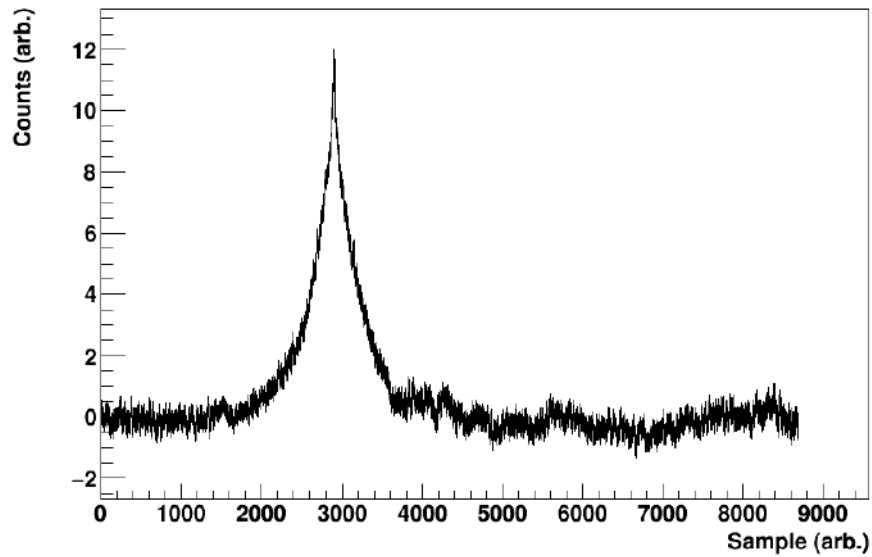


Figure A.3: Filtered waveform after the application of the matched filter.

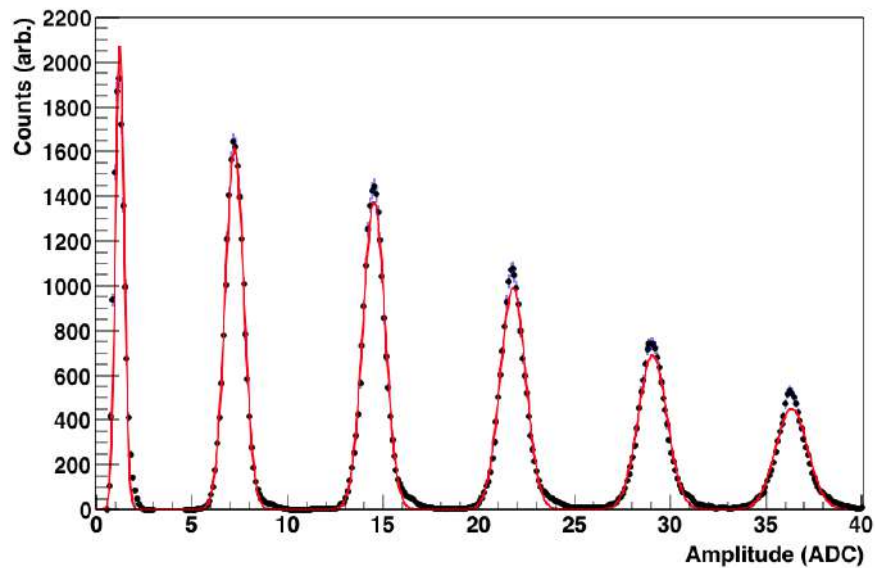


Figure A.4: Amplitude spectrum for bottom channel #0 filtered signal. The deviation of the right tails from their symmetric shape is due to the presence of correlated noises in the SiPMs.

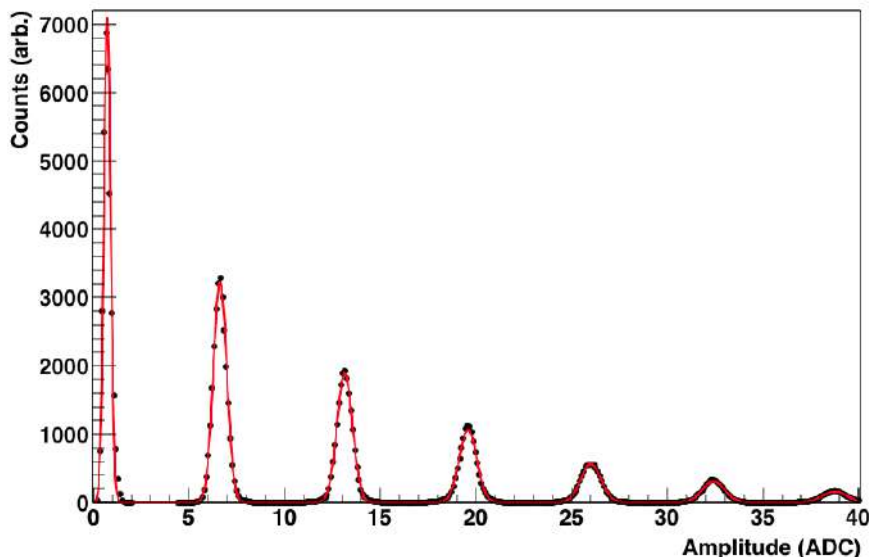


Figure A.5: Amplitude spectrum for top channel #9 filtered signal.

version of the matched filter is a CPU time consuming operation. Figures A.4 and A.5 report two examples of the single electron response (SER, see par. 4.1) after the application of the digital matched filter to the pulses of bottom and top tile channels #0 and #9, respectively. Note that, the right tails of each peak, particularly evident in the case of the bottom tile channel, show a deviation from a symmetric shape with respect to their mean value due to the presence of correlated noise in the SiPMs, like cross-talks and afterpulses. The matched filter technique can be also used to disentangle these kind of noises from the signals.

From the spectra shown above, the SNR can be defined as the ratio between the single-photoelectron peak (signal) and the standard deviation of the baseline measured in a gate window (noise). The single-photoelectron, in particular, is here defined as the difference between the maximum signal amplitude of the first and the second peak evaluated in a fixed gate window:

$$SNR = \frac{\mu_2 - \mu_1}{\sigma_0} \quad (\text{A.3})$$

with  $\mu_1$  and  $\mu_2$  the signal amplitude of the first and second peak, respectively and  $\sigma_0$  the standard deviation of the baseline.

Table A.1 summaries the results obtained for the two cases presented here and in par. 4.1. Third and fifth columns refer, in particular, to SNR and resolution ( $\sigma_1/\mu_1$  of the single-electron peak) after the application of the

Channel	SNR (no filter)	SNR (filter)	$\sigma_1/\mu_1$ (no filter) (%)	$\sigma_1/\mu_1$ (filter) (%)
0 bottom	12.7(14)	32(14)	14.6(1)	6.7(3)
9 top	23.7(8)	36.7(11)	7.9(2)	5.3(2)

Table A.1: Comparison between SNRs and resolutions for filtered and non filtered SER signals, for the two channels highlighted in the text. Third and fifth columns refer to SNR and resolution after the application of the matched filter, respectively (see text for details).

filter, respectively. An improvement of about 60% and 35% for the bottom and the top channel, respectively, in the estimation of the SNR was achieved with the matched filtering algorithm.

## Appendix B

# Quenching factor in liquid scintillators

Energy calibrations of the scintillator detectors used in ReD were already shown in par. 5.3.1. The energy scale was calibrated by using several gamma sources. Since the dependance by the pulse amplitude and energy is supposed to be linear, by using the following:

$$E = p_0 + p_1 \cdot E_{ch} \quad (\text{B.1})$$

electron-equivalent energy for each channel can be calculated. In the previous expression,  $p_0$  and  $p_1$  are the fitting parameters and  $E_{ch}$  is the amplitude expressed in ADC counts.

However, as reported in ref. [79], in the computation of the output light response for liquid scintillators, a correction due to the Birks saturation law [80] has to be considered. The number of excitons and electron-ion pairs produced during the scintillation process is, in fact, proportional to the energy loss  $dE/dx$  with a proportionality constant  $A$ . The concentration of the high ionization density zone of the path length (i.e. the core), on the other hand, is given by  $B \cdot dE/dx$  and it is proportional to the ionization density. So, if  $k$  is the total collision probability, the Birks saturation law [80] is given by:

$$\frac{dS}{dx} = \frac{A \frac{dE}{dx}}{1 + kB \frac{dE}{dx}} \quad (\text{B.2})$$

where  $kB$  is the so-called Birks constant and, together with  $A$ , can be experimentally determined. The above equation describes the response of a scintillator to an ionizing particle of any energy; the scintillation yield being reduced at high ionization density. The quenching factor  $f_i$  is then defined

as:

$$f_l = \frac{1}{1 + kB \frac{dE}{dx}}. \quad (\text{B.3})$$

Detector	p1	$\Delta p_1$
0	6.69e-03	9.49e-05
1	6.57e-03	9.16e-05
2	6.81e-03	9.83e-05
3	7.04e-03	1.05e-04
4	7.54e-03	1.20e-04
5	6.84e-03	9.91e-05
6	6.65e-03	9.36e-05
7	7.02e-03	1.04e-04
8	6.97e-03	1.03e-04

Table B.1: Fitting parameters from linear fit constraining to 0 the intercept. Values are reported for each detector.

Detector	p0	p1	$\Delta p_0$	$\Delta p_1$
0	11.20	6.60e-03	1.30	1.01e-04
1	12.43	6.46e-03	1.28	9.70e-05
2	14.20	6.68e-03	1.28	1.03e-04
3	15.25	6.89e-03	1.28	1.10e-04
4	13.86	7.39e-03	1.32	1.27e-04
5	14.61	6.70e-03	1.27	1.04e-04
6	12.44	6.53e-03	1.28	9.91e-05
7	11.98	6.90e-03	1.31	1.10e-04
8	15.62	6.81e-03	1.27	1.08e-04

Table B.2: Fitting parameters from linear fit with free parameters. Values are reported for each detector.

Tables B.1, B.2 and B.3 report the fit parameters and, in the last one, also  $kB$  parameters taken from linearity response curves per each scintillator detector, together with uncertainties on the last columns. Fit values from table B.1 were obtained by ignoring the photoelectric peak of  $^{241}\text{Am}$  and fixing to zero the  $p_0$  value of the linear function. In the other two sets of data, on the contrary, the americium peak was included in the fit and data were fitted with a linear function with free parameters and by using the Birks saturation law, respectively. The latter in particular was performed by using the procedure described in ref. [81]. Figure B.1 shows the linearity

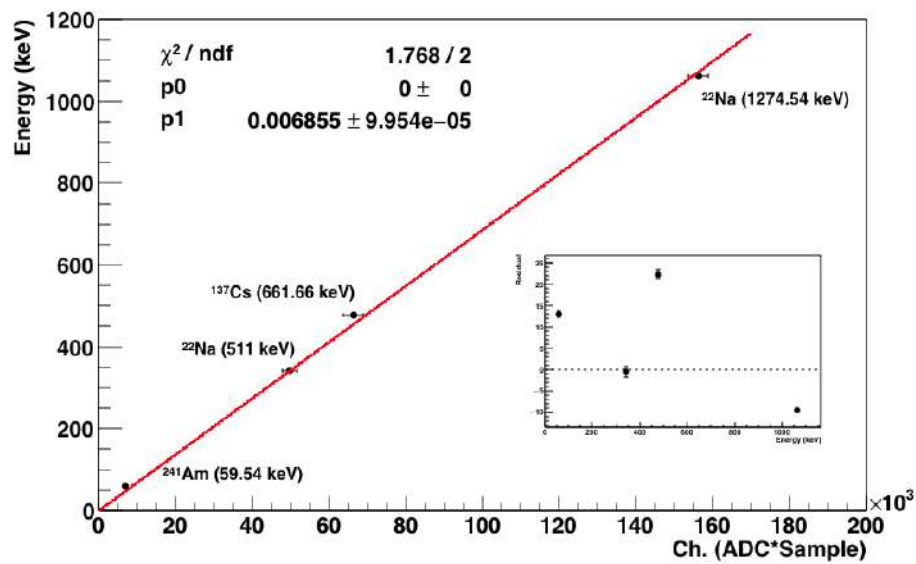


Figure B.1: Linear fit to the LSci #2 calibration curve in the energy range from 59.54 keV ( $^{241}\text{Am}$  full-energy peak) to 1274.54 keV  $\gamma$ -ray by  $^{22}\text{Na}$ . This fit was performed by fixing the  $p_0$  value of the fit to zero and by not taking into account the 59.54 keV point from  $^{241}\text{Am}$  (details in the text).

Detector	p1	kB	$\Delta p_1$	$\Delta kB$
0	6.60e-03	1.12e-02	7.45e-05	1.02e-04
1	6.48e-03	1.19e-02	7.39e-05	3.86e-04
2	6.65e-03	1.54e-02	3.75e-05	2.92e-04
3	6.90e-03	1.70e-02	8.28e-05	6.56e-04
4	7.30e-03	1.55e-02	9.03e-05	7.19e-05
5	6.66e-03	1.59e-02	7.83e-05	4.59e-04
6	6.56e-03	1.19e-02	7.53e-05	3.81e-04
7	6.83e-03	1.34e-02	8.12e-05	9.92e-05
8	6.69e-03	1.91e-02	1.25e-05	1.25e-05

Table B.3: Fitting parameters from Birks saturation law linear fit constraining to 0 the intercept. Values are reported for each detector.

response for the liquid scintillator detector LSci #2. The inset in the figure shows the residuals calculated as the difference between the true expected gamma energies from each source and the measured ones. From the former a loss of linearity is evident, so it is possible to conclude that, because of the quenching, an order one polynomial fit is not the best function in order to fitting data. Furthermore, the fit reported in the above plot does not include the 59.54 keV point from  $^{241}\text{Am}$ .

## Appendix C

# Pulse shape discrimination analysis in liquid scintillators

Pulse Shape Discrimination allows to distinguish, in a liquid scintillator, between different ionizing particles that interact in the active medium of the detector. Scintillation light from fast electrons is mostly generated within the prompt component, compared to recoil protons from neutron interactions (see par. 5.1.1). Those kind of measurements were done using a 65.6 kBq (about 2027 fissions/s)  $^{252}\text{Cf}$  neutron fission source. The optimal parameters for the evaluation of PSD in the used liquid scintillator cells were 60 ns and 300 ns for the short and long gates respectively, with 60 ns of pre-gate and 260 ns for the baseline threshold. Figure C.1 shows a scatter plot of PSD versus energy, obtained for the near detector, i.e. the one that faced the  $^{252}\text{Cf}$  source, while the inset shows the PSD parameter projected on a 1-D histogram in an energy window of 500 keV<sub>ee</sub> between 500 keV<sub>ee</sub> and 1000 keV<sub>ee</sub>. From the latter, the separation of the two populations of events is quite evident, despite the presence of an overlapping region with PSD between 0.1 and 0.15. Neutrons and gamma-rays can be distinguished by putting a cut at about 0.13 in the PSD scale. Figure shows also saturation effects, above 1400 keV<sub>ee</sub>, due to the settings of the DAQ system.

In figure C.2 scatter plots of the pulse shape discrimination parameter versus energy for the eight far detectors are shown. From these, by dividing the energy range in slices of 50 keV<sub>ee</sub> each, it is possible to compute the Figure of Merit (FoM) for each detector (see par. 5.1.1 for its definition) in each slice of energy. One example of FoMs for the LSci #2 far detector is reported in fig. C.3: any slice of energy was fitted with a sum of Gaussian functions in order to derive the FoM as it was defined in par. 5.1.1. From the latter, a distribution of the FoM values versus energy was then derived and results are shown in figure C.4. Comparing the two above figures it is

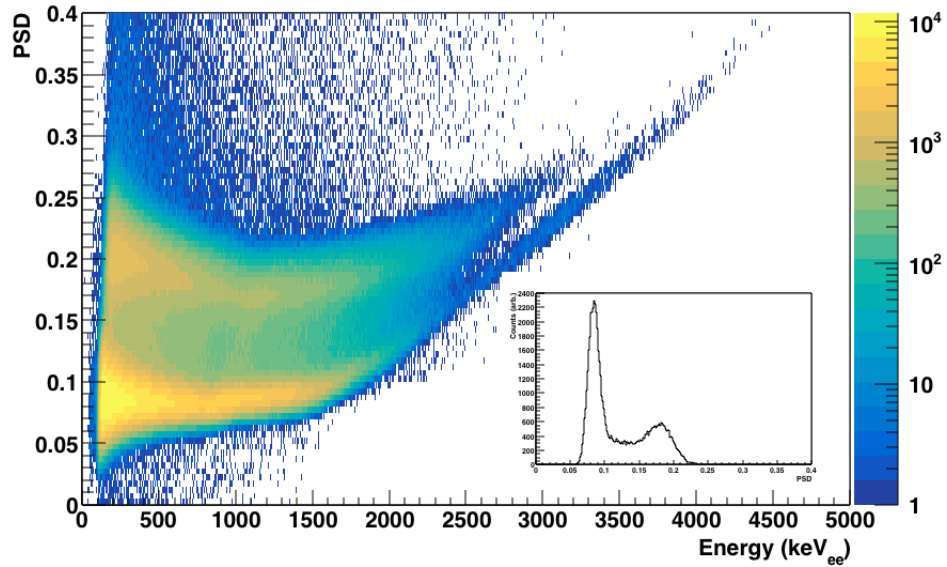


Figure C.1: Scatter plot of PSD versus energy for the near detector of a  $^{252}\text{Cf}$  run. The inset shows the PSD parameter projected on a 1-D histogram in an energy window of  $500 \text{ keV}_{ee}$ .

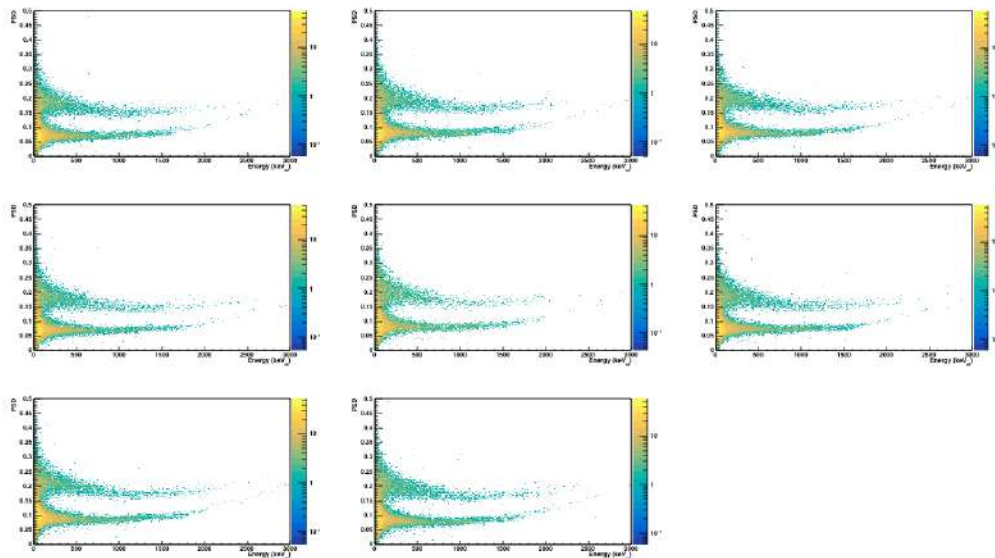


Figure C.2: Scatter plots of PSD versus energy for the far detectors of a  $^{252}\text{Cf}$  run.

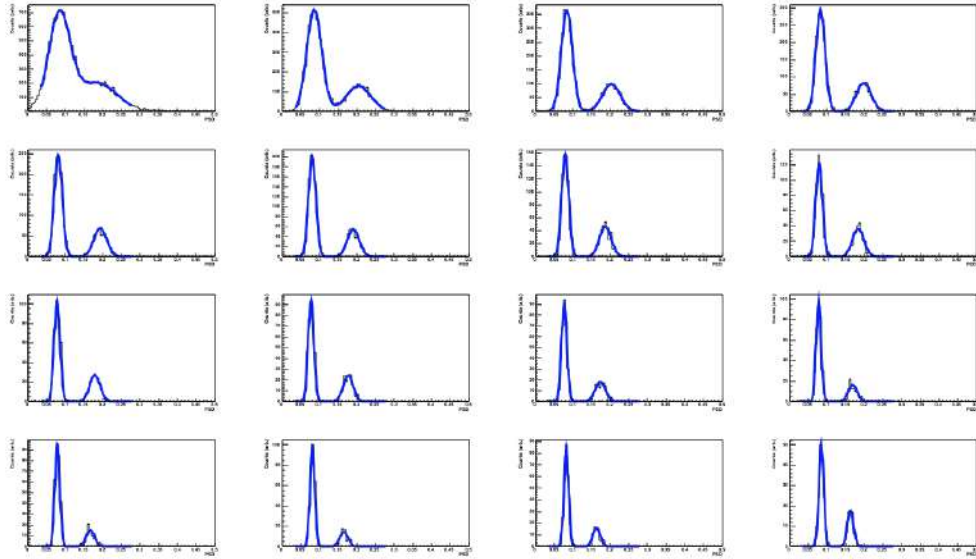


Figure C.3: Figures of Merit (FoMs) in energy slices of  $50 \text{ keV}_{ee}$  each for the LSci #2 far detector.

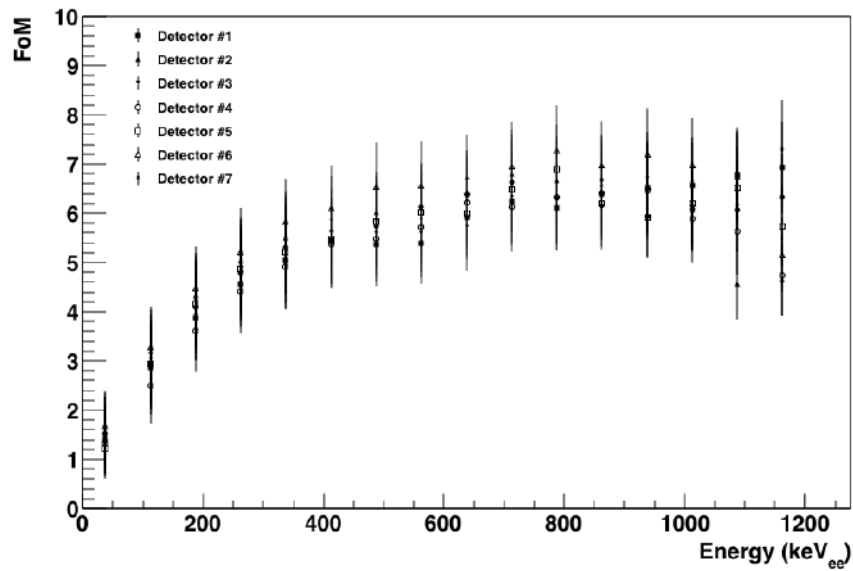


Figure C.4: Distribution of Figure of Merit (FoM) versus energy for each far detector of the neutron spectrometer. Error bars are derived from a toy Monte Carlo simulation.

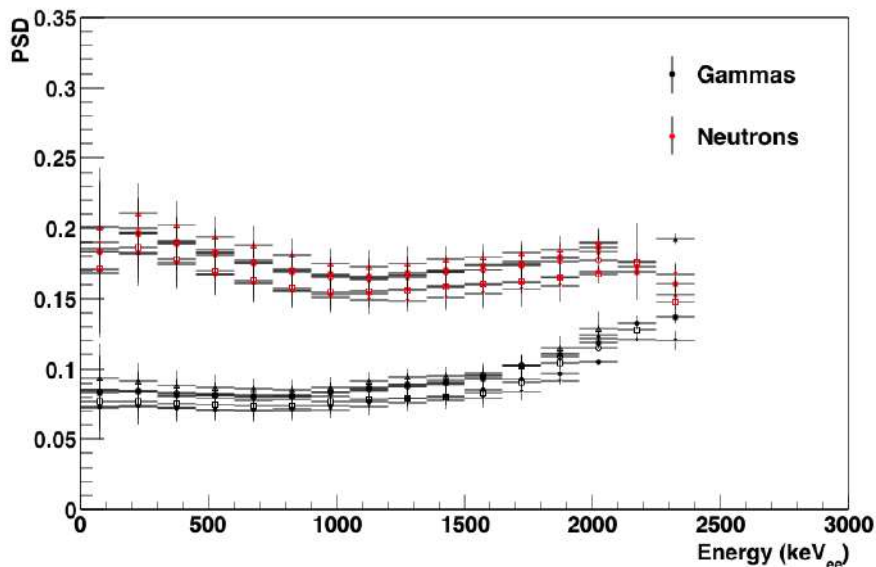


Figure C.5: PSD parameter distribution per each slice of energy ( $50 \text{ keV}_{ee}$ ) per each far neutron detector. Red points are neutron events while the black ones are from gammas. The high energy tail of the distribution is dominated by saturation effects in the detectors.

possible to argue that, starting from  $200 \text{ keV}_{ee}$ , a clear separation between the two classes of events (gammas and neutrons) occurs at a PSD value of about 0.12.

Finally, the figures C.5 and C.6 show distributions of PSD parameter versus energy per each energy slice and per each far detector. The two were obtained for different number of energy slices:  $50 \text{ keV}_{ee}$  each and  $25 \text{ keV}_{ee}$  each, respectively. From the former clear saturation effects occur in the detectors in the high energy tail of the distribution, so a selection of events based on the PSD method is no longer valid, i.e. the two curves tend to have a parallel trend.

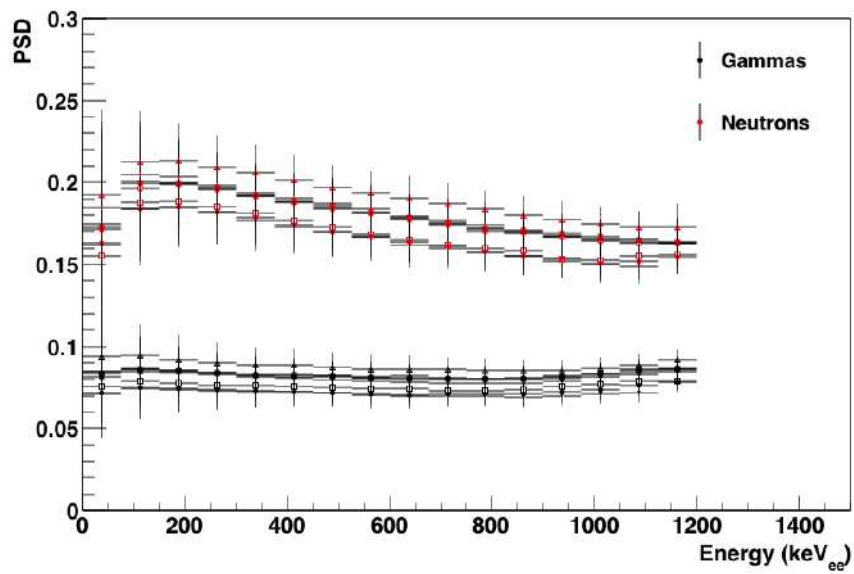


Figure C.6: The same as the previous one obtained by dividing the energy range in slices of 25 keV<sub>ee</sub> each avoiding saturation effects.

# Appendix D

## Neutron detectors efficiencies

Detector	$\epsilon$ @ 2.5 MeV (%)	$\Delta\epsilon$ (%)	$\epsilon$ @ 7 MeV (%)	$\Delta\epsilon$ (%)
1	28.2	2.6	19.3	2.4
2	32.9	2.8	41.7	3.6
3	36.6	2.9	28.1	2.9
4	29	2.6	25.3	2.9
5	22	2.3	22.6	2.7
6	36.1	2.9	35.2	3.4
7	31.9	2.8	35.1	3.2
8	31.4	2.7	30	3

Table D.1: Measured efficiencies compared for single neutron detector at 2.5 MeV and at 7 MeV, at a 100 keV<sub>ee</sub> threshold. Statistical uncertainties are also reported.

Table D.1 reports the measured efficiencies for each detector together with the statistical uncertainties for 2.5 MeV and 7 MeV incoming neutrons, while figure D.1 shows the efficiencies per each liquid scintillator detector of the ReD neutron spectrometer.

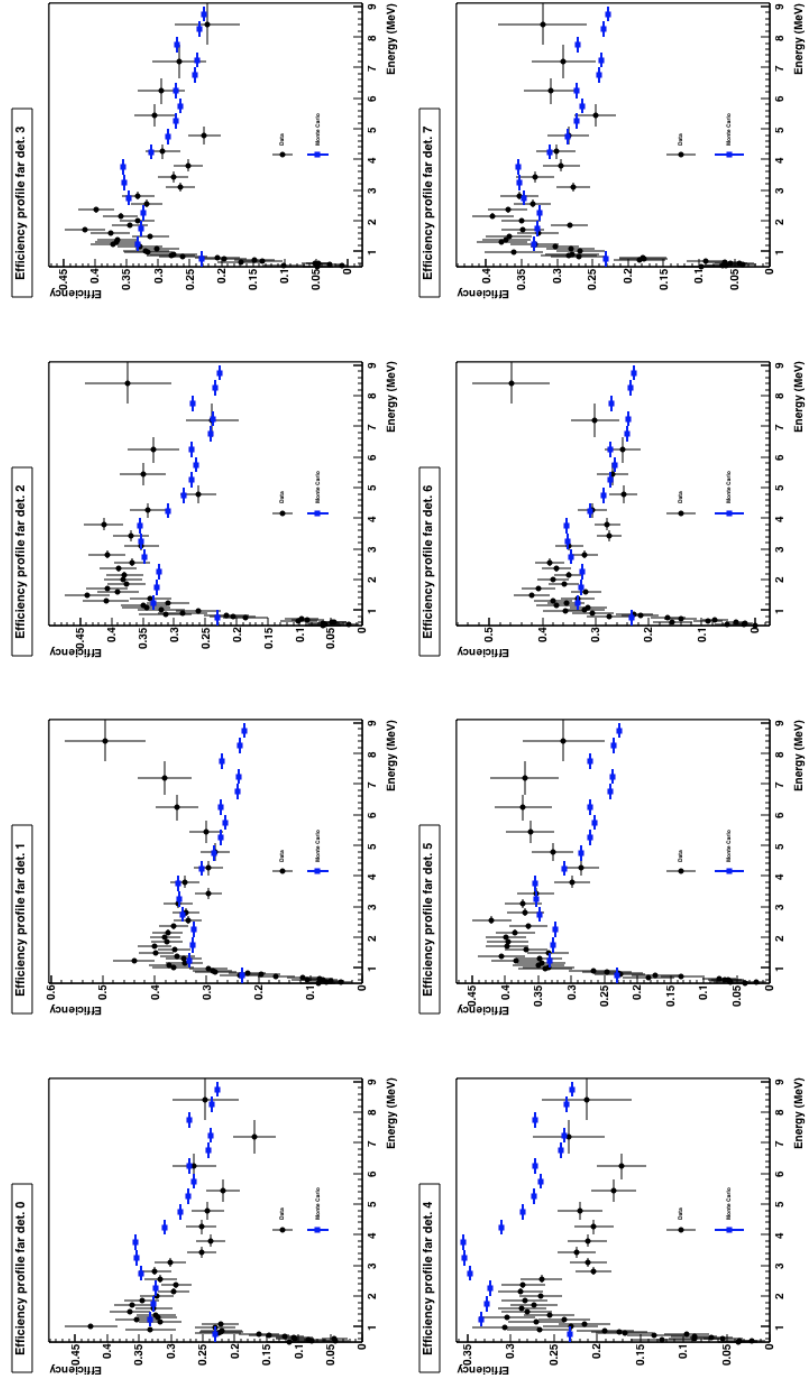


Figure D.1: Efficiency profiles from single neutron liquid scintillator detector (black points) compared with Monte Carlo expectations (blue dots).

# Bibliography

- [1] J. H. Oort, **The force exerted by the stellar system in the direction perpendicular to the galactic plane and some related problems**, Bull. Astron. Inst. Netherlands **6** (1932) 249;
- [2] F. Zwicky, **Die Rotverschiebung von extragalaktischen Nebeln**, Helv. Phys. Acta **6** (1933) 110;
- [3] F. Zwicky, **On the Masses of Nebulae and of Clusters of Nebulae**, ApJ **86** (1937) 217;
- [4] S. M. Faber, J. S. Gallagher **Masses and Mass-To-Light Ratios of Galaxies**, Ann. Rev. Astro. Astrophys. **17** (1979) 135;
- [5] D. N. Spergel et al., **First-Year Wilkinson Microwave Anisotropy Probe (WMAP) Observations: Determination of Cosmological Parameters**, ApJ. Supp. Ser. **148** (2003) 175;
- [6] D. Clowe et al., **A Direct Empirical Proof of the Existence of Dark Matter**, ApJ **648** (2006) L109;
- [7] P. A. R. Ade et al., **Planck 2015 results. XIII. Cosmological parameters**, Astron. Astrophys. **594** (2016) A13;
- [8] T. S. Van Albada et al., **Distribution of Dark Matter in the spiral galaxy NGC 3198**, APJ **295** (1985) 305-313;
- [9] G. Gamow, **The Evolution of the Universe**, Nature **162** (1948) 680-682;
- [10] A. A. Penzias and R. W. Wilson, **A Measurement of Excess Antenna Temperature at 4080 Mc/s**, ApJ **142** (1965) 419-421;
- [11] J. A. R. Cembranos, **Modified gravity and dark matter**, Journal of Physics: Conference Series **718** (2016) 032004;

- 
- [12] P. A. R. Ade et al., **Planck 2013 results. XVI. Cosmological parameters**, *Astron. Astrophys.* **571** (2014) A16;
- [13] P. J. E. Peebles, **Primeval adiabatic perturbations-Effect of massive neutrinos**, *ApJ* **258** (1982) 415;
- [14] D. N. Schramm and G. Steigman, **Relic Neutrinos and the Density of the Universe**, *ApJ* **243** (1981) 1;
- [15] S. Dodelson and L. M. Widrow, **Sterile neutrinos as dark matter**, *Phys. Rev. Lett.* **72** (1994) 17;
- [16] C. A. Baker et al., **An Improved experimental limit on the electric dipole moment of the neutron**, *Phys. Rev. Lett.* **97** (2006) 131801;
- [17] R. D. Peccei and H. R. Quinn, **CP conservation in the presence of pseudoparticles**, *Phys. Rev. Lett.* **38** (1977) 1440;
- [18] F. Wilczek, **Problem of Strong  $P$  and  $T$  Invariance in the Presence of Instantons**, *Phys. Rev. Lett.* **40** (1978) 279;
- [19] S. Weinberg, **A new light boson?**, *Phys. Rev. Lett.* **40** (1978) 223;
- [20] O. Chwolson, **Über eine mögliche form fiktiver Doppelsterne**, *Astronomische Nachrichten* **221** (1924) 329;
- [21] S. Burles et al., **Big Bang nucleosynthesis predictions for precision cosmology**, *ApJ* **552** (2001) L1;
- [22] B. J. Carr and S. W. Hawking, **Black holes in the early Universe**, *MNRAS* **168** (1974) 399;
- [23] B. P. Abbott et al., **GW170608: Observation of a 19 solar mass binary black hole coalescence**, *ApJ Lett.* **851** (2017) L35;
- [24] J. L. Feng, **Dark Matter candidates from particle physics and methods of detection**, *Ann. Rev. Astron. Astroph.* **48** (2010) 495;
- [25] M. C. Smith et al., **The RAVE Survey: Constraining the Local Galactic Escape Speed**, *Mon. Not. Roy. Astron. Soc.* **379** (2007) 379;
- [26] E. Kuflik, A. Pierce and K. M. Zurek, **Light neutralinos with large scattering cross sections in the minimal supersymmetric standard model**, *Phys. Rev. D* **81** (2010) 111701;

- 
- [27] P. Agnes et al., (DarkSide Collaboration), **DarkSide-50 532-day Dark Matter Search with Low-Radioactivity Argon**, Phys. Rev. D **98** (2018) 102006;
- [28] D. S. Akerib et al., (The LUX Collaboration), **Results from a Search for Dark Matter in the Complete LUX Exposure**, Phys. Rev. Lett. **118** (2017) 021303;
- [29] A. Marchionni et al., (ArDM Collaboration), **ArDM: a ton-scale LAr detector for direct Dark Matter searches**, J. Phys.: Conf. Ser. **308** (2011) 012006;
- [30] A. Badertscher et al., (ArDM Collaboration), **Status of the ArDM Experiment: First results from gaseous argon operation in deep underground environment**, arXiv:1307.0117v1 (2013);
- [31] J. Calvo et al., (ArDM Collaboration), **Status of ArDM-1t: First observations from operation with a full ton-scale liquid argon target**, arXiv:1505.02443v1 (2013);
- [32] R. Ajaj et al., (The DEAP-3600 Collaboration), **Search for dark matter with a 231-day exposure of liquid argon using DEAP-3600 at SNOLAB**, arXiv:1902.04048 (2019);
- [33] Aprile E. et al., (The XENON Collaboration), **Dark Matter search results from a one ton-year exposure of Xenon1T**, Phys. Rev. Lett. **121** (2018) 111302;
- [34] C. E. Aalseth et al., (The DarkSide Collaboration), **DS-20k: A 20 Tonne Two-Phase LAr TPC for Direct Dark Matter Detection at LNGS**, Eur. Phys. J. Plus **133** (2018) 131;
- [35] R. Bernabei et al., (DAMA/LIBRA Collaboration), **First model independent results from DAMA/LIBRA-phase2**, arXiv:1805.10486 (2018);
- [36] C. E. Aalseth et al., (CoGeNT Collaboration), **Search for An Annual Modulation in Three Years of CoGeNT Dark Matter Detector Data**, arXiv:1401.3295v1 (2014);
- [37] R. Agnese et al., (CDMS Collaboration), **Silicon Detector Dark Matter Results from the Final Exposure of CDMS II**, Phys. Rev. Lett. **111** (2013) 251301;

- 
- [38] M. Aaboud et al., (ATLAS Collaboration), **Search for chargino-neutralino production using recursive jigsaw reconstruction in final states with two or three charged leptons in proton-proton collisions at  $\sqrt{s} = 13$  TeV with the ATLAS detector**, arXiv:1806.02293 (2018);
- [39] T. Alexander et al., **Light yield in DarkSide-10: A prototype two-phase argon TPC for dark matter searches**, *Astropart. Phys.* **49** (2013) 44;
- [40] W. H. Lippincott et al., **Scintillation time dependence and pulse shape discrimination in liquid argon**, *Phys. Rev. C* **78** (2008) 035801;
- [41] A. Hitachi et al., **Effect of ionization density on the time dependence of luminescence from liquid argon and xenon**, *Phys. Rev. B* **27** (1983) 5279;
- [42] D. D'Angelo, **DarkSide-50 Results from first Argon run**, Oral Contribution to *20th Particle & Nuclei International Conference, Hamburg, Germany* (2014);
- [43] A. I. Bolozdynya, **Two-phase emission detectors and their applications**, *NIM A* **422** (1999) 314;
- [44] I. M. Obodovskii et al., **Emission of hot electrons from liquid and solid argon and xenon**, *J. Exp. Theo. Phys.* **55** (1982) 860;
- [45] P. Agnes et al., (DarkSide Collaboration), **The veto system of the DarkSide-50 Experiment**, *JINST* **11** (2016) P03016;
- [46] P. Agnes et al., (DarkSide Collaboration), **CALIS - A CALibration Insertion System for the DarkSide-50 dark matter search experiment**, *JINST* **12** (2017) T12004;
- [47] P. Agnes et al., (DarkSide Collaboration), **Simulation of argon response and light detection in the DarkSide-50 dual phase TPC**, *JINST* **12** (2017) P10015;
- [48] P. Agnes et al., (DarkSide Collaboration), **Constraints on Sub-GeV Dark Matter-Electron Scattering from the DarkSide-50 Experiment**, *Phys. Rev. Lett* **121** (2018) 111303;

- 
- [49] P. Agnes et al., (DarkSide Collaboration), **Low-mass Dark Matter Search with the DarkSide-50 Experiment**, Phys. Rev. Lett **121** (2018) 081307;
- [50] B. Abi et al., (DUNE Collaboration), **The Single-Phase Proto-DUNE Technical Design Report**, arXiv:1706.07081 (2017);
- [51] Global Argon Dark Matter Collaboration, **Future Dark Matter Searches with Low-Radioactivity Argon**, European Strategy on Particle Physics December 2018;
- [52] M. Cadeddu et al., **Directional dark matter detection sensitivity of a two-phase liquid argon detector**, J. Cosm. Astropart. Phys. **01** (2019) 014;
- [53] G. Jaffè, **Zur theorie der ionisation in kolonnen**, Ann. Phys. **42** (1913) 303; G. Jaffè, **On the Theory of Recombination**, Phys. Rev. **58** (1940) 968;
- [54] D. R. Nygren, **Columnar recombination: a tool for nuclear recoil directional sensitivity in a xenon-based direct detection WIMP search**, J. Phys.: Conf. Ser. **460** (2013) 012006;
- [55] V. Cataudella et al., **Directional modulation of electron-ion pairs recombination in liquid argon**, JINST **12** (2017) P12002;
- [56] The ReD Collaboration, **REcoil Directionality (RED) Project**, Recoil directionality proposal to CSN5 2015 (2015);
- [57] H. Cao et al., (The SCENE Collaboration), **Measurement of scintillation and ionization yield and scintillation pulse shape from nuclear recoils in liquid argon**, Phys. Rev. D **91** (2015) 092007;
- [58] M. Lebois et al., **Development of a kinematically focused neutron source with the  $p(^7\text{Li},n)^7\text{Be}$  inverse reaction**, NIM A **735** (2014) 145;
- [59] A. Mandarano, **New generation, SiPM-based, Liquid Argon TPCs from the kg to the multi-ton scale**, PhD thesis (2017) Gran Sasso Science Institute;
- [60] G. Chiodini, **The PADME experiment for dark mediator searches at the Frascati BTF**, JINST **12** (2017) C02037;

- 
- [61] H. Liskien and A. Paulsen, **Neutron production cross sections and energies for the reactions  ${}^7\text{Li}(p,n){}^7\text{Be}$  and  ${}^7\text{Li}(p,n){}^7\text{Be}^*$** , Atomic Data and Nuclear Data Tables **15** (1975) 57;
- [62] Evaluated nuclear data file (endf), <https://www.nndc.bnl.gov/exfor/endf00.jsp>, February 2018;
- [63] National Nuclear Data Center (nndc), <https://www.nndc.bnl.gov>, July 2019;
- [64] S. Vinogradov et al., **Probability Distribution and Noise Factor of Solid State Photomultiplier Signals with Cross-Talk and Afterpulsing**, IEEE Nucl. Science Symp. Conf. Rec. **25** (2009) 1496;
- [65] U. Fano, **Ionization Yield of Radiations. II. The Fluctuations of the Number of Ions**, Phys. Rev. **72** (1947) 26;
- [66] T. Doke et al., **LET dependence of scintillation yields in liquid argon**, NIM A **269** (1988) 291;
- [67] P. Agnes et al., (The ARIS Collaboration), **Measurement of the liquid argon energy response to nuclear and electronic recoils**, Phys. Rev. D **97** (2018) 112005;
- [68] S. Amoruso et al., (The ICARUS Collaboration), **Analysis of the liquid argon purity in the ICARUS T600 TPC**, NIM A **516** (2004) 68;
- [69] S. Kubota et al., **Recombination luminescence in liquid argon and in liquid xenon**, Phys. Rev. B **17** (1978) 2762;
- [70] E. Aprile et al., **Observation of anticorrelation between scintillation and ionization for MeV gamma rays in liquid xenon**, Phys. Rev. B **76** (2007) 014115;
- [71] M. Miyajima et al., **Average energy expended per ion in liquid argon**, Phys. Rev. A **9** (1974) 1438;
- [72] G. F. Knoll, **Radiation Detection and Measurement - Third edition** (2000) 219 - 263;
- [73] L. Stevanato et al., **Neutron detection in a high gamma-ray background with EJ-301 and EJ-309 liquid scintillators**, NIM A **690** (2012) 96;

- [74] F. Pino et al., **The light output and the detection efficiency of the liquid scintillator EJ-309**, Appl. Radiat. Isot. **89** (2014) 79;
- [75] O. Klein and Y. Nishina, **Über die Streuung von Strahlung durch freie Elektronen nach der neuen relativistischen Quantendynamik von Dirac**, Z. Phys. **52** (1929) 853;
- [76] J. F. Dicello et al., **Radiation Quality of Californium-252**, Phys. Medicine and Biology **3** **17** (1972) 345;
- [77] A. B. Smith et al., **Spontaneous Fission Neutron Spectrum of Cf<sup>252</sup>**, Phys. Rev. **108** (1957) 411;
- [78] S. W. Smith, **The Scientist and Engineer's Guide to Digital Signal Processing** (1998) 107 - 122;
- [79] N. V. Kornilov et al., **Total characterization of neutron detectors with a <sup>252</sup>Cf source and a new light output determination**, NIM A **599** (2009) 226;
- [80] J. B. Birks, **Scintillations from Organic Crystals: Specific Fluorescence and Relative Response to Different Radiations**, Proc. Phys. Soc. A **64** (1951) 511;
- [81] A. Grau Malonda and A. Grau Carles, **The ionization quench factor in liquid-scintillation counting standardizations**, Appl. Radiat. Isot. **51** (1999) 183.